Mind's eye: Saccade-related evoked potentials support visual memory encoding in humans

Gansheng Tan[1,2,3,4], Phillip Demarest[1,2,3,4], Yilin Li[1,2,3.4], Hohyun Cho[5], Haeorum Park[2,3,4], James R. Swift[2,3,4], Cory S. Inman[6], Joseph R. Manns[7], Stephan B. Hamann[7], Xiaoxuan Liu[1,2,3,4], Krista L. Wahlstrom[6], Ziwei Li[1,2,3,4], Martina K. Hollearn[6], Justin M. Campbell[8], Patrick E. Cettina[1,2,3], Siddharth S. Sivakumar[1,2,3], Eric C. Leuthardt[1,2,3,4], Jon T. Willie[1,2,3,4,9], Peter Brunner[1,2,3,4]

[1] Department of Biomedical Engineering, Washington University in St. Louis, St. Louis, MO, USA
[2] Department of Neurosurgery, Washington University School of Medicine in St. Louis, St. Louis, MO, USA
[3] Division of Neurotechnology, Washington University School of Medicine in St. Louis, St. Louis, MO, USA
[4] National Center for Adaptive Neurotechnologies, St. Louis, MO, USA
[5] Department of Neurosurgery, University of Alabama, Birmingham, AL, USA
[6] Department of Psychology, University of Utah, Salt Lake City, UT, USA
[7] Department of Psychology, Emory University, Atlanta, GA, USA
[8] Spencer Fox Eccles School of Medicine, University of Utah, Salt Lake City, UT, USA
[9] Department of Neurosurgery, University of Texas at Austin, Austin, TX, USA

*communicating authors: Jon T. Willie and Peter Brunner

Highlights

- Widespread, consistent evoked potentials follow saccades (Saccade-Related Evoked Potentials, SREPs) in human subjects with intracranial electrodes
- SREPs are not oculomuscular artifacts and carry no discernible information about saccade direction
- SREPs occur earlier and at higher peak amplitudes in the temporal lobes than in other anatomical regions
- Earlier and high-amplitude SREPs predict successful visual encoding

Graphical abstract

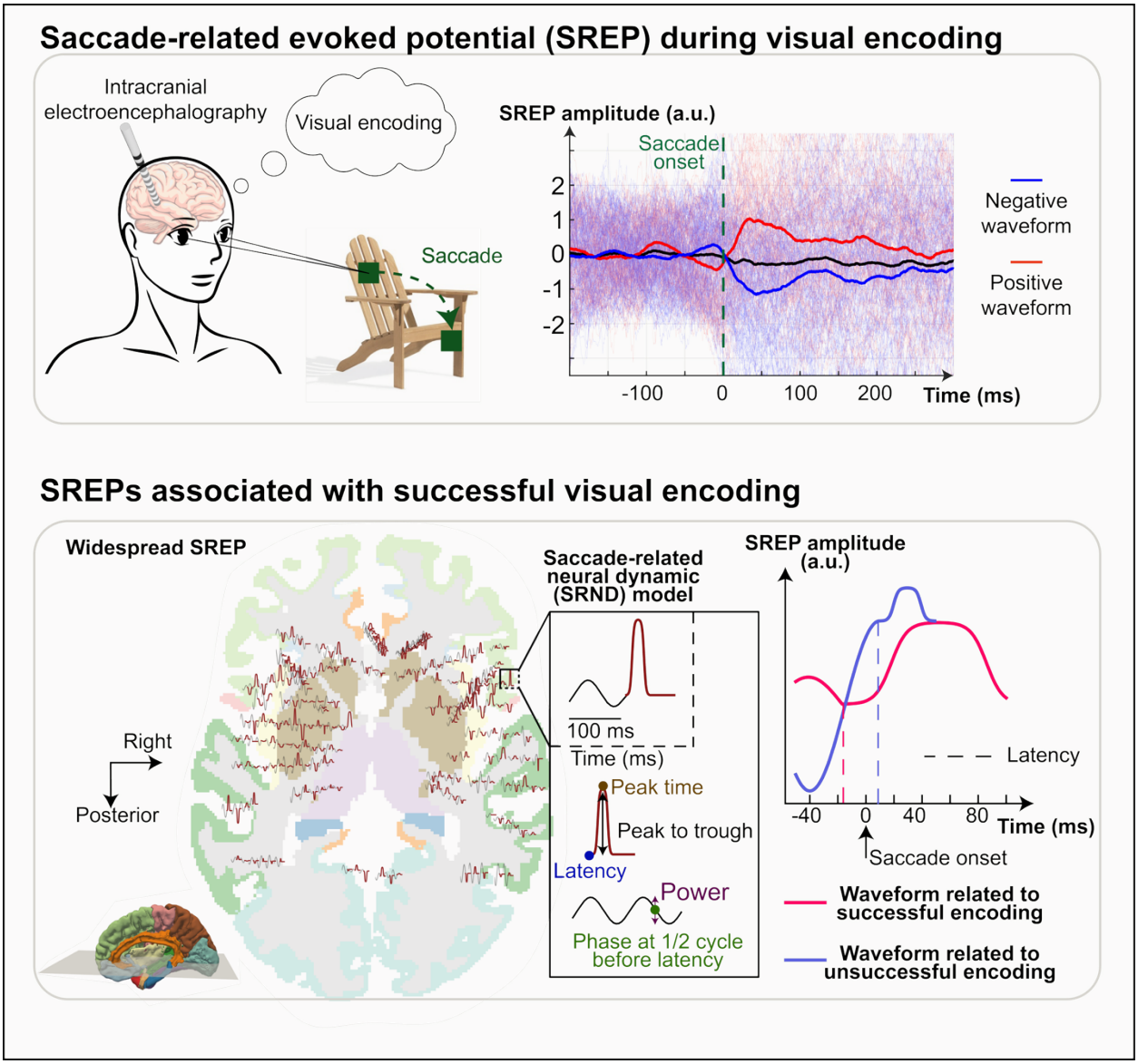

SUMMARY

In active vision, the brain receives and encodes discontinuous streams of visual information gated by saccadic eye movements. Saccadic modulation of neural activity has been observed in nonhuman primates and is hypothesized to support perception and memory; however, its functional role in humans remains unclear. In our study, we tested the hypothesis that saccadic modulation of neural activity in humans predicts successful visual encoding. For this purpose, we measured eye gaze and local field potentials in intracranially-monitored patients while they performed visual encoding tasks. We observed consistent brain-wide evoked potentials following saccades (saccade-related evoked potentials, SREPs). These SREPs were not attributable to ocular muscle activity or retinal input. Their magnitudes were not explained by spatial proximity to eye muscles or saccade eccentricity, and their polarity bore no relationship to saccade direction. Instead, the phase of pre-saccadic oscillations aligned with saccade timing and dissociated SREPs with positive polarity from those with negative polarity. Spatiotemporal profiling revealed that SREPs emerged earliest and with the greatest magnitude in the temporal lobes. We developed a saccade-related neural dynamic (SRND) model that characterized pre-saccadic oscillatory activity and SREP at each intracranial recording site using a finite set of features. Random forest models trained with these features achieved 62.6% balanced accuracy for predicting next-day recognition (long-term memory). Using the Shapley value, a framework for explaining machine learning models, we identified an SREP profile, characterized by earlier latency and larger magnitude, that was associated with successful visual encoding. In contrast, predicting saccade direction using the same SRND model performed at chance level, indicating that the observed SREP is less likely a corollary discharge signaling saccadic motor copy. These findings demonstrate that SREPs are a direct result of saccadic modulation of neural activity and that they contribute to human visual encoding.

Introduction

Every shift in eye gaze has the potential to shape visual memory[1]. Humans actively explore the environment through rapid eye movements that alternate between saccades and fixations. Saccades rapidly move the fovea to a new location in the visual field, and in the subsequent fixation, visual information from this location is sent to the visual system[2]. The brain processes the dynamic inflow of visual information structured by eye movements, constructs meaningful representations, and forms memories. Despite the important role of saccades in gating visual

input, many efforts to understand neurophysiological processes in visual memory overlook the saccade-related neural dynamics.

Saccades in primates were accompanied by changes in electrical potentials in the medial temporal cortex[3–5]. These changes in local field potentials (LFPs) have been shown to synchronize single-unit activity and reset neural oscillation phase, which suggests saccadic modulation of neural circuits[3,6–8]. In this paper, we refer to such signals as saccade-related evoked potentials, operationally defined as consistent LFP waveforms time-locked to saccade onset, without presuming a specific underlying cause. While one interpretation is that SREPs are responses to a changing visual image on the retina, findings of SREP in darkness and during rapid eye movement sleep challenge this hypothesis and suggest additional functions beyond visual response[9,10]. Because saccades discretize visual input and gate the timing at which information enters the visual system, SREPs are well positioned to coordinates when and how visual information is processed for effective encoding into memory[11]. Understanding whether and how SREPs contribute to visual encoding is critical, as it may elucidate neural mechanisms underlying active vision and inform neuromodulation strategies for improving memory. However, the existence and functional role of SREPs in humans remain largely unknown due to technological constraints in simultaneous intracranial electrophysiology and eye tracking during naturalistic, free-viewing behavior.

Early research on visual processing largely focused on stimulus-driven responses, in which visual stimuli were presented at fixed retinal locations to minimize eye movements and isolate passive sensory processing[12]. Although this approach allows precise control of when and where visual stimuli are presented, it sacrifices ecological validity. Recent advances in optical eye-tracking technology enable real-time tracking of gaze. Simultaneous recording of eye movement and neural activity allows researchers to align neural dynamics with eye movements and visual input, opening new avenues to study visual processing in a more natural setting[13]. Identifying SREP requires neuronal recordings with millisecond temporal precision. Neuroimaging, such as functional magnetic resonance imaging (fMRI), generally lacks the necessary temporal resolution. Noninvasive methods, such as scalp electroencephalography, provide millisecond temporal resolution but are limited in the identification of the underlying neural sources[14]. Source localization remains a challenging inverse problem that depends heavily on assumptions and parameter choices. Oculomotor signals generated by eye muscles can confound the analysis of saccadic modulation, as reported in human electrophysiology[15,16].

One hypothesis of the functional role of saccadic modulation posits it as a form of *corollary discharge*, a copy of the motor signal that prepares the brain for the sensory consequences of an impending movement[17]. In vision, the corollary discharge mechanism maintains visual continuity despite the disrupted visual input resulting from saccades[18]. Specific neural pathways underlying the corollary discharge mechanism have been previously identified in nonhuman primates. The projections, from the superior colliculus (SC) to the frontal eye field via the medial dorsal thalamic nucleus and from the SC to the middle temporal cortex through the inferior pulvinar, carry the vectors of impending saccades and contribute to visual continuity[19]. A recent study observed saccadic modulation of neuronal activity exhibiting some properties of corollary discharge in the human mesial temporal lobe, a region involved in high-level visual processing and memory formation[8]. This finding also comports with the broader active sensing framework, which posits that motor sampling, such as sniffing in rodents and saccades in primates, is not random but part of a coordinated strategy that optimizes sensory information processing[20–23] (**Figure 1A**). Although these findings point towards a role of saccadic modulation in visual encoding, direct evidence in humans has yet to be established.

We aim to determine whether saccadic modulation serves higher-order cognitive functions such as visual encoding, in addition to basic perception. Two principal methods for quantifying neural dynamics in electrophysiological signals are evoked potentials (EPs) and spectral dynamics. EPs measured with intracranial electrodes capture the rapid extracellular voltage deflections associated with synchronous neuronal activity following saccades[8,24]. Spectral dynamics analysis typically requires longer time series that span multiple cycles of the assumed oscillation to accurately estimate its periodic properties[25]. Recent work has emphasized the importance of separating strictly defined rhythmic components from the aperiodic $1/f$ activity when interpreting power spectra, and the methodology and interpretations of these components are under active investigation[26]. Given this context, we sought to investigate the most rudimentary and well-established form of saccadic modulation, SREP, and test our hypothesis that SREPs predict visual encoding outcome.

This study investigates the existence, spatiotemporal dynamics, and cognitive relevance of SREPs by leveraging a unique research window: patients with intractable epilepsy who undergo stereoelectroencephalography (SEEG) monitoring for seizure onset zone localization. To record and analyze neural activity during active vision, we used the BCI2000 platform, which enables synchronous stimulus presentation, intracranial local field potential (LFP) recordings, and eye gaze tracking[27]. We first confirmed the presence of SREPs and verified that they represent

saccadic modulation rather than ocular muscle signals. We observed two waveform patterns of SREPs and examined potential determinants of these patterns, such as saccade direction and oscillatory activity. We found that the instantaneous phase of the preceding oscillations modulates the polarity of SREPs. To identify the neural pathway underlying saccadic modulation, we characterized the spatiotemporal dynamics of SREPs. We found that earlier and higher-amplitude SREPs were spatially clustered in the temporal lobe. Next, we tested our central hypothesis that SREPs play a functional role in visual encoding using random forest models. Our results confirmed that SREP characteristics predicted successful visual encoding. Building on this, we used Shapley value analysis to interpret the mapping between SREP characteristics and the visual encoding learned by the models[28]. In general, earlier SREPs with greater magnitude and later peak times predicted successful visual encoding. Finally, to assess whether these SREPs reflect a narrowly defined corollary discharge signal, we evaluated whether they encoded saccade direction[17]. We confirmed that most, if not all, SREPs did not encode either the current or subsequent saccade direction. These results suggest that SREPs support visual encoding in the human brain, as a mechanism of saccadic modulation, separate from classical corollary discharge.

Results

Visual memory encoding performance and eye movement characteristics

Eight human subjects participated in this study (see **Supplementary Table 2** for patient characteristics). Across the eight subjects, a total of 1629 electrode contacts spanning 129 trajectories were implanted, with an average of 204 ± 30 (mean ± SD; SD, standard deviation) contacts on 16 ± 2 trajectories per subject (**Figure 1C**). We identified and excluded electrode contacts exhibiting epileptiform activity or artifactual signals (e.g., due to poor contact) (**Supplementary Table 3**), resulting in an average of 201 ± 29 valid contacts per subject. Additionally, for 6 subjects, two Behnke Fried Depth electrodes (AD-TECH), each with 8-contact micro-wires, were implanted. **Figure 1D** and **Figure 1 – Figure supplement 2A** show the regional distribution of electrode contacts and sampling density, respectively.

Subjects participated in a series of visual memory encoding tasks, each comprising an encoding phase followed by a test phase the next day. (see **Appendix A** for study protocol, see **Figure 1 – Figure supplement 1G** for exemplar stimuli). During each encoding trial, an image of an object or scene was presented on a screen, and subjects were instructed to remember it for a later memory test. (**Figure 1B**). Subjects freely scanned the presented images while eye gaze

and intracranial electroencephalogram (iEEG) data were recorded (**Figure 1E**). Subjects completed one or more visual memory encoding tasks with distinct image sets on non-overlapping days, when feasible. The number of completed tasks depended on the duration of each patient's stay in the epilepsy monitoring unit (**Supplementary Table 1,** see **STAR Methods** - study design section for details).

This study is part of a clinical trial that investigated the effect of amygdala stimulation on declarative memory (NCT05065450). In this clinical trial, brief electrical stimulation of the amygdala was delivered immediately following image presentation in half of the visual memory encoding trials, followed by a 5-s intertrial interval. To study the saccadic modulation in the normative visual encoding process, we restricted analyses to trials that met the following criteria: (1) no amygdala stimulation was delivered during the trial; (2) the subject maintained their gaze on the monitor for more than half of the trial duration as determined from eye-tracking data; and (3) the subject pressed one of the response buttons. Applying these criteria yielded 1130 valid visual encoding trials, comprising 7292 saccades (**Supplementary Table 1**).

We verified that subjects performed the task as instructed and assessed whether the brief preceding amygdala stimulation had any latent effect on memory performance and saccadic behaviors. All subjects exhibited memory performance better than chance (i.e., 50%, see **STAR Methods** - Assessing memory outcome). The overall correct recognition rate, which incorporates both correct identification of previously presented images and correct rejection of novel images, was 72% $\pm$ 8% (mean $\pm$ standard deviation, SD) (**Figure 1F, Figure 1 – Figure supplement 1F, Supplementary Table 3**). Subjects exhibited saccadic kinematics consistent with human active visual sampling from the environment[29]. The mean fixation duration was 183 ms (SD = 266 ms); and the mean saccade duration was 48 ms (SD = 15 ms, **Figure 1G**). The saccade directions were dispersed, with a relatively higher probability of horizontal and vertical eye movements (35.54% and 26.45%, respectively, **Figure 1G,** see **STAR Methods** – Saccade detection and characterization section for details). These results indicate that subjects were attentive and visually scanned the presented images.

Next, to assess whether the brief preceding amygdala stimulation exerted a latent effect on the subsequent trial, we compared saccade behavior and recognition memory performance between trials with and without a preceding amygdala stimulation trial. The effect size (i.e., Cohen's d) for duration differences between trials with and without a preceding amygdala stimulation trial was trivial (-0.015 for saccades and -0.024 for fixation, **Figure 1 – Figure**

supplement 1C–D). The circular distribution of saccade direction did not differ significantly between trials following an amygdala stimulation trial (N_1 = 3657) and those not following amygdala stimulation (N_2 = 3635, Watson–Williams test, p=0.879, F = 0.023, **Figure 1 – Figure supplement 1A–B**). The correct recall rate for trials that followed an amygdala stimulation trial, and those that did not, were both 75% (**Figure 1 – Figure supplement 1E)**. These results reject the possibility that the brief preceding amygdala stimulation confounded visual encoding and saccades.

SREPs are consistent, brain-wide, and exhibit two polarities

SREPs represent a canonical form of saccade-locked neural modulation that has been documented in nonhuman primates[3–5], whereas evidence in humans remains sparse. We therefore first asked whether intracranial LFPs in intracranially monitored humans exhibit the defining property of SREPs, that is, temporally consistent waveform time-locked to saccade onsets[30]. In the presence of SREPs, we expected that the inter-trial Pearson correlation coefficients computed on LFP signals within the peri-saccadic window (i.e., -10 to +40 ms relative to saccade onset) would be greater than those within the pre-saccadic baseline (i.e., -200 to -10 ms relative to the saccade onset)[30]. We also systematically varied the pre-saccadic and baseline window sizes to assess the temporal extent of this consistency (see **Discussion**). To ensure that the inter-trial correlation was calculated from local, saccade-related neural activity rather than artifacts or stimulus-driven responses, we excluded electrode contacts containing artifactual signals, applied small Laplacian re-referencing, and excluded saccades occurring 200 ms before or after the image onset (see **STAR Methods**).

To our surprise, the peri-saccadic inter-trial correlations exhibited a more bimodal distribution, compared to the approximately normally-distributed inter-trial correlations during baseline (**Figure 2A, Figure 2 – Figure supplement 2A**). In 98% of electrode contacts, the peri-saccadic inter-trial correlation distribution significantly deviated from baseline inter-trial correlation distribution (**Figure 2 – Figure supplement 2B**, median p-value $< 1 \times 10^{-20}$, significance threshold after correcting for multiple comparisons = 1.9×10^{-5}, Kolmogorov-Smirnov tests). To quantify the effect size of this deviation, we computed the absolute difference in the area under the curve (AUC) between the peri-saccadic and baseline empirical cumulative distribution functions of inter-trial correlations (**Figure 2 – Figure supplement 2A)**. The deviation effect size corresponding to the adjusted significance threshold was 0.017, whereas the 2.5–97.5 percentiles of the deviation effect size distribution were 0.011 to 0.228 (**Figure 2 – Figure supplement 2B**). These results imply two clusters of internally consistent LFP waveforms following saccades.

To identify these two clusters, we applied agglomerative hierarchical clustering to the inter-trial correlation matrix and partitioned the resulting dendrogram at the first bifurcation (**Figure 2B,** see **STAR Methods** - Identification of SREPs). **Figure 2D** shows the averaged SREPs for the two identified clusters at an electrode contact in the middle temporal lobe, which exhibit opposing polarity and phase of pre-saccadic oscillatory activity. Pooling inter-trial correlations across the two clusters of waveforms would obscure waveform consistency; therefore, we separately quantified SREP waveform consistency for each cluster, using the area under the receiver operating characteristic (ROC) curve[30] (see **STAR Methods** - Identification of SREP, **Figure 2C**). As a control, we repeated this process for baseline LFP to adjust for hierarchical clustering-induced AUC inflation (**Figure 2E**). The peri-saccadic area under the ROC curve was significantly higher than the baseline-derived control area under the ROC curve (Cohen's d = 2.651, two-tailed paired t-test, n = 2604, t statistic = 81.13, $p < 0.001$, **Figure 2F**).

Thus far, we have found that SREPs in humans are consistent across saccades and exhibit two opposing waveform polarities. We next asked whether these consistent SREPs were localized to specific anatomical circuits or broadly distributed throughout the cortex. To answer this question, we defined SREP prevalence at anatomical regions as the proportion of electrode contacts with area under the ROC curve in the peri-saccade condition above the mean + 2 SD of the control area under the ROC curve (**Figure 2G**). The SREP prevalence across all cortical regions, except the right motor cortex (37%), exceeded 50%. The fusiform gyrus (left: 92.0%, right: 97.0%), temporal (left: 91.0%, right: 96.7%), and parietal lobes (left: 0.86%, right: 100.0%) were the three regions with the highest SREP prevalence. To obtain a threshold-independent estimate of SREP prevalence across regions, we varied the thresholds from the mean to the mean + 4 SD of the control area under the ROC curve, and integrated the resulting SREP prevalence across this range, yielding a prevalence summary metric. This analysis revealed a similar spatial pattern in SREP prevalence (**Figure 2–Figure Supplement 1**). We ranked brain regions based on the area under the ROC curve for peri-saccadic intertrial correlations, and based on their difference from the control area under the ROC curve (**Figure 2 – Figure supplement 2C–E**). The differences in area under the ROC curve were generally higher in the temporal lobe (except the medial temporal lobe) and parietal lobe, followed by the frontal lobe, and subcortical regions. The electrode contact-level spatial pattern of differences in area under the ROC curve was consistent with previous findings (**Figure 2 – Figure Supplement 3A–E**). The peri-saccadic area under the ROC curve averaged across polarities was also higher than baseline for LFPs recorded from micro-wires, but this difference was less pronounced compared to LFPs recorded from macro electrode contacts(**Figure 2 – Figure Supplement 3F–G**, Cohen's d = 0.227, two-tailed paired t-

test, n = 115, t statistic = 2.088, p = 0.039). These results demonstrate that SREPs in humans are consistent and brain-wide.

SREPs in iEEG reflect neural activity rather than ocular-muscle electromyogram artifacts

Intracranial recordings have an exceedingly high signal-to-noise ratio compared to noninvasive modalities and are therefore widely regarded as being free of ocular-muscle electromyogram (EMG)[31]. Nevertheless, one study showed that signals recorded from subdural electrocorticography grids may be contaminated by ocular-muscle EMG signals[16]. In this study, Kovach et al. correlated peak-to-trough amplitude of EPs at saccade times with saccade eccentricity and electrode-to-eyeballs distance[16]. Given this precedent, we tested two predictions that would hold if the observed SREPs reflect ocular-muscle EMG signals: (1) Cluster-level averaged SREP peak amplitude would decrease with increasing distance between the electrode contacts and the nearest eye globe center, which approximates the distance between electrode contacts and the myogenic dipole source generated by extraocular muscle activation; and (2) Single-trial SREP peak amplitude would increase with greater saccade eccentricity, reflecting stronger extraocular muscle activation. This ocular-muscle EMG could explain the two opposing SREP polarities observed in our study, as saccades in opposite directions could engage different pairs of extraocular muscles and generate myogenic fields of opposing polarity across the head. We later show this to be false (see **Results** – Phase of preceding oscillatory activity associated with SREP polarity).

To test the first prediction, we identified onset latency, peak amplitude, and peak-to-trough amplitude for cluster-level averaged SREPs and single-trial SREPs (**Figure 3A**, see **STAR Methods** – Characterization of SREP waveforms). The distance from the eyeballs accounted for only a minor fraction of variance in peak amplitude of averaged SREPs (**Figure 3D**, explained variance = 3.8%, n = 2573 for positive polarity; explained variance = 3.5%, n = 2575 for negative polarity, linear regression). To ensure that our findings were not dependent on a specific choice of SREP amplitude metric, we adopted the measure used in Kovach et al.[16], peak-to-trough amplitude. In our study, distance from the eyeballs only explained 0.9% and 0.7% variance in peak-to-trough amplitude of cluster-level averaged SREPs for positive and negative clusters, respectively, across all electrode contacts (**Figure 3 – Figure Supplement 1A**, n = 2571 for positive polarity; n = 2570 for negative polarity; linear regression). These results do not support the first prediction.

To test the second prediction, we assessed whether single-trial SREP peak amplitude scaled with saccade eccentricity using linear regression. As waveform characterization is less reliable for single-trial SREPs that deviate substantially from the cluster-level averaged SREP due to background neural activity, we quantified the alignment between each single-trial SREP and the corresponding cluster-averaged SREP waveform using Spearman's correlation; and used single-trial SREPs with similarity above the median (i.e., 0.413) for analysis based on single-trial SREPs. The distribution of waveform alignment was skewed towards positive values, with an area under the kernel density curve of 0.812 for correlations greater than zero (**Figure 3B–C**). This indicates a general alignment between single-trial and averaged SREP waveforms. Linear regression revealed that saccade eccentricity explained 0.0% of the variance in peak amplitude for both polarities (**Figure 3E,** |estimated coefficient| < 0.001, p < 0.001, n = 250531 for positive polarity; |estimated coefficient| < 0.001, p = 0.156, n = 250614 for negative polarity; linear regression with t-test). For both polarities, saccade eccentricity explained 0.0% variance in single-trial SREP peak-to-trough amplitude (**Figure 3 – Figure Supplement 1B,** |estimated slope| < 0.001, p = 0.020, n = 250531 for positive polarity; |estimated coefficient| < 0.001, p = 0.079, n = 250614 for negative polarity; linear regression with t-test**)**. The results show no relationship between SREP peak amplitude and saccade eccentricity.

To establish that SERPs are not ocular-muscle EMG, we next confirmed that ocular muscle EMG amplitude correlated with saccade eccentricity, as a positive control. We extracted electrooculogram (EOG) signals from fronto-polar EEG scalp electrodes (Fp1 and Fp2) using bipolar re-referencing, and extracted the peak and peak-to-trough amplitude of single-trial EPs at saccade times using the clustering and waveform characterization methods as for SREPs. Compared to SREPs recorded with intracranial electrodes, single-trial EP peak amplitude from EOG signals showed a strong dependence on saccade eccentricity, with larger estimated slopes and greater explained variance (**Figure 3F,** explained variance = 7.0%, estimated slope = 0.133, p < 0.001, n = 1100 for positive polarity; explained variance = 6.7%, estimated slope = -0.130, p < 0.001, n = 1126 for negative polarity; linear regression with t-test). This dependence holds when we quantified single-trial EP magnitude from EOG signals using peak-to-trough amplitudes (**Figure 3 – Figure Supplement 1C**, explained variance = 2.7%, estimated slope = 0.108, p < 0.001, n = 1100 for positive polarity; explained variance = 8.2%, estimated slope = -0.171, p < 0.001, n = 1126 for negative polarity; linear regression with t-test). Direct comparison revealed that the variance explained by saccade eccentricity was significantly greater in the ocular-muscular signals captured in fronto-polar scalp EEG electrodes compared to intracranial recordings (**Figure 3G**, t = 3.154, p = 0.012, Cohen's d = 3.193, $n_{EOG} = 10$, $n_{EOG} = 2367$, Welch's

t-test, rank-biserial correlation = 0.833). The above results convincingly demonstrated that the observed SREPs cannot be explained by ocular muscle EMG.

We next examined whether the SREPs represented a change in visual input resulting from saccades. If this were the case, we would not expect consistent LFP waveforms following saccades that occurred in the absence of meaningful visual changes, that is, during the intervals between images when a blank screen containing a fixation cross on a uniform black background is presented. We computed the SREP consistency during fixation-cross presentation periods using the same method described above. Despite the absence of changes in visual inputs, SREP consistency during fixation-cross presentation was significantly higher than baseline (**Figure 3H**, paired t-test, $p<0.001$, Cohen's $d = 2.631$, $n = 2604$). Across electrode contacts, SREP consistency during image presentation was positively correlated with that during fixation-cross presentation (**Figure 3I**, Pearson correlation coefficient = 0.752, $p < 0.001$, based on t-distribution). This correlation indicated regional specificity in how saccades modulate LFPs independently of concurrent visual input. We calculated the ratio of electrode contacts showing consistent SREPs across anatomical regions during fixation cross presentation and found the spatial pattern was similar to that during image presentation (**Figure 3 – Figure Supplement 1E**, **Figure 2G**).

These results demonstrate that SREPs are not attributable to changes in visual input nor ocular-muscle EMG signals.

Phase of preceding oscillatory activity is associated with SREP polarity

We found that SREPs exhibited two opposing polarities and sought to understand the physiological basis of this observation. We first considered two parsimonious mechanisms that could result in SREPs of two polarities: (1) volume-conducted ocular-muscle EMG, which we have shown to be unlikely; and (2) neural activity associated with saccade planning or execution. Both mechanisms predict polarity-specific directional clustering, i.e., that saccades associated with SREPs of the same polarity exhibit greater directional clustering compared to all saccades; and that saccade directions differ between SREPs of opposing polarities.

To test these predictions, we quantified directional clustering of saccades using Rayleigh statistics. For each electrode contact, we computed Rayleigh statistics based on the saccade directions associated with positive-polarity and negative-polarity SREPs separately (Monopolar condition), and compared them against Rayleigh statistics computed from the same number of saccades pooled across both polarities (Combined condition), thereby controlling for sample size. We found no evidence of polarity-specific directional clustering. For both polarities, differences in

Rayleigh statistics between monopolar and combined conditions were centered at zero (**Figure 4 – Figure Supplement 1C,** t = -0.953 p = 0.341, Cohen's d = -0.022, n = 2068 for positive polarity; t = -1.028, p = 0.304, Cohen's d = -0.023, n = 2058 for negative polarity; two-tailed t-test). Across electrode contacts, there was no significant difference in saccade direction between SREPs of opposing polarities (95% CI for W statistics = [1.926, 2.107], the corresponding 95% CI for p-value is [0.486, 0.512], Mardia-Watson-Wheeler test). In contrast to SREPs, EPs at saccade times derived from EOG signals, capturing volume-conducted ocular-muscle EMGs, exhibited strong polarity-specific directional clustering (**Figure 4 – Figure Supplement 1A**). for EOG signals, polarity-specific Rayleigh statistics were significantly higher than those computed from the same number of saccades pooled across polarities (**Figure 4 – Figure Supplement 1B,** t = 5.950, p < 0.001, Cohen's d = 1.881, n = 15 for positive polarity; t = 4.553, p = 0.001, Cohen's d = 1.440, n = 18 for negative polarity; paired t-test). The circular distribution of saccade direction differed significantly between positive and negative EPs from EOGs at saccade times (p < 0.001 for all subjects, 95% CI for W statistics = [33.223, 46.050], Mardia-Watson-Wheeler test). These findings rule out both oculomotor artifacts and neural activity coding saccade directions as possible explanations for the observed opposing SREP polarities.

The ubiquitous presence of oscillatory activities in LFPs and the phase-locking relationship between saccade timing and alpha oscillations reported in a previous study prompted us to consider whether the phase of preceding oscillatory activity modulates SREP polarity[32]. Therefore, we first identified the dominant neural oscillation at each electrode contact by detecting peaks in the one-over-frequency ($1/f$)-normalized power spectral density (**Figure 4A**, see **STAR Methods** - Oscillation detection and quantification). Across electrode contacts, the distribution of oscillation frequency centered at 11 Hz (**Figure 4 – Figure Supplement 1D**). We quantified the power of these oscillatory activities as the deviation between the power spectral density and the $1/f$ fit at the dominant frequency. **Figure 4 – Figure Supplement 1E** shows the distribution of the power of oscillatory activities. The mean oscillation power was 5.9 $\mu V^2/Hz$, suggesting the presence of neural oscillation.

Next, to determine whether the phase of neural oscillations preceding SREPs modulates their polarity, we quantified the difference in oscillation phase for positive and negative SREPs at five time points: 0.5, 1, 1.5, 2, and 3 oscillatory cycles (OCs) before the onset of each SREP. To minimize the influence of SREP in instantaneous phase estimation, we applied the Hilbert transform to narrowband-filtered LFPs before each SREP onset at $\pm$2 Hz around the dominant oscillation frequency (**Figure 4A,** see **STAR Methods**). For each time point, we quantified phase

separation as the area under the absolute difference between the two probability density functions of the instantaneous phase associated with each polarity (**Figure 4B**). To evaluate the statistical significance of the observed phase separation between polarities, we performed permutation testing in which we generated surrogate (i.e., null) distributions for each electrode contact by randomly permuting the polarity labels. Across electrode contacts, phase separation before SREP onset was significantly higher compared to the null distributions (**Figure 4C,** $p < 0.001$ for all time points, paired Wilcoxon signed-rank, n = 1970 pairs). The degree of separation, quantified by the rank-biserial correlation, continuously increased steadily as time approached SREP latency, from 0.204 (3 OCs before SREP onset latency) to 0.581, 0.790, 0.901, and 1.000 (0.5 OCs before SREP onset latency). These results show that for each electrode contact, SREP polarity is associated with the phase of pre-SREP neural oscillations.

We next asked whether the relationship between pre-SREP oscillation phase and SREP polarity was consistent across electrode contacts. To answer this question, we computed the circular mean of phase for each polarity and electrode contact by averaging across saccades. We found that mean phase values across electrode contacts formed distinct polarity-specific clusters (**Figure 4D,** all Bonferroni-corrected $p < 0.001$, number of comparisons = 10, $n_{positive}$ = 1975, $n_{positive}$ = 1976, Rayleigh test). Furthermore, phase concentration increased progressively as time approached SREP onset latency, resulting in greater separation of the mean phases between polarities (**Figure 4D,** Rayleigh statistic/mean resultant length R = 0.186, 0.386, 0.478, 0.597, and 0.677 at 3, 2, 1.5, 1, and 0.5 OCs before SREP onset for negative polarity, R = 0.174, 0.352, 0.458, 0.583, and 0.662 for positive polarity). At 1 OC before SREP latency, the mean phase values associated with positive SREPs were near $\pm\pi$, corresponding to the trough of the oscillation, whereas the mean phase values associated with negative SREPs were near 0, corresponding to the oscillation peak. These results support that the relationship between SREP polarity and the phase of pre-saccadic oscillation is consistent across recording sites.

Active sensing theory proposes that neuronal oscillations create cyclic windows of efficient sensory processing that are temporally coordinated with sampling behaviors[33]. We tentatively interpreted the observed phase separation between positive and negative SREPs as evidence that an oscillatory cycle contains two such windows for visual memory encoding. This interpretation predicts that the oscillation phase associated with the same SREP polarities align across saccades. To test this prediction, we quantified phase alignment using the inter-trial phase coherence (ITPC), separately for positive and negative SREPs. For both polarities, ITPC increased monotonically from 2 OCs before SREP onset latency, and then decreased after SREP

peak time (**Figure 4E**). The effect sizes (i.e., Cohen's d) between ITPC at 2 OCs before SREP onset latency and subsequent 4 time points (from 1 OC before SREP onset latency to 1 OC after SREP peak time) were 1.214, 1.625, 1.739, 1.704, and 1.427. These findings show that SREPs may be embedded in a broader window of saccade-timed neural coordination.

While phase alignment indexes the temporal coordination between neural oscillation and SREPs, oscillation power reflects the degree of synchronous local population activity accompanying SREPs[34]. We therefore examined the temporal dynamics of oscillatory power during SREPs. To enable comparison across electrode contacts and subjects, we normalized the oscillatory power to its magnitude at two OCs before SREP onset latency. Oscillatory power increased from 2 OCs before the SREP onset latency and remained elevated at that level throughout the SREP period (**Figure 4 – Figure Supplement 1F**). To determine whether phase alignment and oscillatory power during SREPs reflect dissociable neural processes, we compared their temporal dynamics by quantifying their correlation across time points. We found the strongest positive correlation at SREP onset latency (**Figure 4F**, $R^2 = 0.274$). The correlation was weaker at time points preceding and following SREP onset, with R^2 = 0.022 at 1 OC before SREP latency, R^2 = 0.118 at 0.5 OCs before SREP latency, R^2= 0.198 at the SREP peak, followed by a decline to R^2 = 0.046 at 0.5 OCs after the SREP peak. These results show partially divergent temporal profiles of phase alignment and oscillatory power.

Together, our results demonstrate a systematic relationship between pre-SREP oscillation phase and SREP polarity, along with an interplay between ongoing oscillation and SREP.

SREPs occur earlier and at higher peak amplitude in the temporal lobe

To understand the large-scale organization of SREPs, we sought to characterize the spatial structure in SREP onset latency and peak amplitude throughout the brain. One precondition for the presence of such a structure is inter-contact (i.e., across-locations) variability in these two SREP parameters. Because we hypothesized that SREPs contribute to visual memory encoding, we also expected trial-by-trial (intra-contact) variability that explained variance in recognition of the presented images. Therefore, we quantified intra-contact and inter-contact variability in SREP onset latency and amplitude. To ensure comparability, we estimated intra-contact and inter-contact variability based on matched sample sizes (see **STAR Methods** - Quantifying intra- vs inter-contact variability of SREP characteristics). The average intra-contact standard deviation of SREP latencies was 5.3 ms for both polarities (**Figure 5A**), whereas the average time interval between peak time and latency was 38.6 ms (SD = 12.3 ms). Inter-contact standard deviation of SREP onset latencies, was 7.1 ms for negative SREPs and 6.6 ms for positive SREPs, both

significantly greater than intra-contact variability (**Figure 5A**, N = 786, W statistics = 24141, $p < 0.001$, rank-biserial correlation = -0.766 for negative polarity; N = 797, W statistics = 34836, $p < 0.001$, rank-biserial correlation = -0.669 for positive polarity; Wilcoxon signed-rank test). This finding shows that, despite variability in SREP onset latency within regions, greater variability arises across regions, suggesting a systematic spatial structure in SREP onset latency.

We next used cluster-level averaged SREP onset latency to characterize this spatial structure. For this approach to be used, two preconditions should be satisfied: across electrode contacts, (1) positive and negative SREP onset latency positively correlated, such that pooling positive and negative SREPs does not obscure location-specific latency patterns; and (2) inter-contact differences in cluster-level averaged SREP latency positively correlated with differences at the single-trial level, ensuring that the cluster-level averages reflect location-specific onset latency. Our evaluation of the preconditions revealed that, across electrode contacts, onset latencies for positive and negative SREPs were positively correlated (Pearson $r = 0.436$, $p < 0.001$; **Figure 5 – Supplement 1A–B**). We found a significant positive correlation between inter-contact differences in clustered-level averaged SREP onset latency and the corresponding effect sizes computed from single-trial SREPs (**Figure 5 – Supplement 1C**, Pearson $r = 0.436$, $p < 0.001$, t-test). These results satisfy the preconditions for characterizing the spatial structure in cluster-level SREP onset latency.

Using cluster-level SREP onset latency, we found that electrode contacts with earlier SREPs were clustered in the temporal lobe (**Figure 5B**). To quantitatively characterize this spatial pattern, we identified electrode contacts with SREP onset latency in the 0–15th percentile range and applied 3-dimensional (3D) Gaussian Mixture Models (GMMs) to their spatial locations. This analysis revealed two predominant clusters located in each temporal lobe. We computed the SREP onset latency averaged across electrode contacts within each anatomical region (see **Figure 5C** for the list of regions), and confirmed that the SREPs in the bilateral temporal lobes had earlier latencies than those in other regions (**Figure 5C**). SREPs of both polarities exhibited similar latency patterns across regions (**Figure 5 – Figure supplement 1E–F**). These results quantitatively confirm that SREPs first occur in the temporal lobes.

If the observed SREPs represent a sequence of the saccadic modulation originating in the temporal lobes, we expect earlier SREPs to be more spatially localized and later SREPs to be spatially dispersed. To verify this expectation, we stratified electrode contacts by SREP latency percentiles and quantified spatial spread as the Euclidean norm of the standard deviations of contact coordinates along three orthogonal axes (Left-right, posterior-anterior, and inferior-

superior). We found that spatial spread increased progressively from early to late SREPs (**Figure 5D, Figure 5 – Figure supplement 1D**), confirming our expectation.

To determine how brain regions are temporally involved in saccadic modulation, we stratified SREPs into categorical percentile bins: early (0–15th), mid (30–45th), and late (60–75th), and calculated the proportion of electrodes within each region falling into these ranges. Consistent with our prior finding, early SREPs were overwhelmingly observed in the bilateral temporal lobes and insula. Mid-latency SREPs were observed in parietal, subcortical regions (basal ganglia and thalamus), and medial temporal (amygdala and hippocampus) region; and late SREPs were more broadly distributed (**Figure 5D**). While this categorical analysis identified brain regions involved in early or late saccadic modulation, it remains unclear how a single region's involvement in saccadic modulation evolves. Therefore, we identified regions showing a graded involvement that diminishes progressively as SREP onset latency increases by computing, for each region, the Spearman correlation between the latency percentile bin (ordered from earliest to latest) and the proportion of electrodes whose SREP onset latency fell into that bin. A negative correlation indicates greater engagement in early SREPs with progressively reduced engagement at later times, whereas a positive correlation indicates the opposite. We found strong negative correlation in the middle temporal (Spearman's $\rho = -0.97$, corrected $p < 0.001$, number of comparisons = 20), inferior temporal ($\rho = -0.74$, corrected $p = 0.455$), and superior temporal ($\rho = -0.98$, corrected $p < 0.001$) regions; and a positive correlation in the orbital frontal ($\rho = 0.82$, Bonferroni corrected asymptotic $p = 0.136$) and inferior frontal regions ($\rho = 0.89$, corrected $p = 0.025$). These results show a graded shift in regional involvement from early temporal to later frontal saccadic modulation.

Reasoning that both SREP timing and magnitude may be structured by the same saccadic modulation circuitry, we examined whether SREP peak amplitude exhibits a spatial organization similar to that of the SREP onset latency. We confirmed the two aforementioned preconditions for cluster-level SREP peak amplitude. Specifically, across electrode contacts, peak amplitude of cluster-level averaged SREPs for positive and negative polarities was significantly and negatively correlated, reflecting the opposing polarities (**Figure 5 – Figure supplement 2B–C**, Pearson's correlation coefficient = -0.365, $p < 0.001$). For a pair of electrode contacts, the effect size between their single-trial SREP peak amplitude was positively correlated with the difference in peak amplitude in their averaged SREP (**Figure 5 – Figure supplement 2D**, Pearson's correlation coefficient = 0.510 for negative SREPs, Pearson's correlation coefficient = 0.479 for positive SREPs, $p < 0.001$ for both polarities, based on t-distribution). Following the same reasoning as in

the SREP onset latency analysis above, we quantified intra- and inter-contact variability in SREP peak amplitude and found that the mean intra-contact variability was higher than the inter-contact variability (**Figure 5 – Figure supplement 2A**). While greater intra-contact variability suggests that single-trial SREP peak amplitude mostly reflects dynamic neural processes associated with each saccade, it does not preclude the presence of systematic anatomical differences in cluster-level average SREP peak amplitude. In fact, cluster-level average SREPs with higher peak amplitude averaged across polarities were also clustered in the bilateral temporal lobes (**Figure 5F**, **Figure 5 – Figure supplement 2G**). These results show similar spatial patterns for SREP peak amplitude and onset latency.

To determine whether the strongest saccadic modulation is also localized to the temporal lobes, we stratified electrodes by percentile bins of absolute peak amplitude and computed spatial spread. We found that spatial spread decreased monotonically with increasing saccadic modulation strength, measured by absolute SREP peak amplitude (**Figure 5G**). Stronger SREPs formed localized spatial clusters in the temporal lobe, whereas SREPs with lower absolute peak amplitudes were more spatially dispersed **(Figure 5 – Figure supplement 2E**). We performed a region-wise correlation analysis between the peak amplitude percentile bin and the proportion of electrodes whose SREP peak amplitude fell in that bin. This analysis revealed significant positive correlation for anterior temporal (**Figure 5 – Figure supplement 2F,** $\rho = 0.95$, Bonferroni corrected asymptotic $p = 0.002$, number of comparison = 20), inferior temporal ($\rho = 0.95$, corrected $p = 0.001$), and middle temporal ($\rho = 0.93$, corrected $p = 0.005$) regions.

In summary, SREPs exhibit a spatially structured progression, characterized by earlier and stronger SREPs in the temporal cortex and later involvement of broader cortical and subcortical regions.

SREPs predict visual memory encoding outcome

The central hypothesis of our study is that SREP morphology predicts visual memory encoding (remembered versus forgotten). To test this hypothesis, we employed random forest models to determine potential non-linear relationships between SREP morphology and visual memory encoding[35]. Because each SREP waveform is a high-dimensional time series, mapping the full waveform to memory outcomes would be computationally inefficient and difficult to interpret biologically. We therefore sought a low-dimensional yet physiologically meaningful representation of SREP morphology. Building on our earlier findings of an association between pre-saccadic neural oscillation and the subsequent SREP waveform, we defined a saccade-related neural dynamic (SRND) model for each saccade at a location. The SRND model decomposes the neural

dynamics at saccade times into two components: pre-saccadic oscillatory activity and the following SREP (**Figure 6A**). We described these two components using five parameters: SREP onset latency, SREP peak-to-trough amplitude, SREP peak time, and the power and phase of the ongoing oscillation at half OCs before the saccade onset (see **STAR Methods**). The SRND models preserve key morphological features of SREP and ongoing neural oscillations and enable interpretable learning of the relationship between SRNDs and memory outcome.

A potential confound arises if systematic differences in saccadic behavior existed between remembered and forgotten trials and if those behaviors were correlated with SRND parameters. In that case, the random forest classifier could achieve above-chance prediction by exploiting saccadic behavior-memory associations, in addition to SRNDs. Although our earlier analyses found no association between saccadic behaviors and SRND parameters, we took an additional precaution before training the classifier. Specifically, we verified that saccadic behaviors themselves did not predict visual encoding (**Figure 6B**). We found comparable saccade eccentricity and duration between saccades during remembered and forgotten trials ($n_{remembered}$ = 3913, $n_{forgotten}$ = 1227, t = -0.325, p = 0.745, Cohen's d = -0.011, t-test for saccade eccentricity; t = -1.237, p = 0.216, Cohen's d = -0.0039, t-test for saccade duration). To assess differences in saccade direction between remembered and forgotten trials, we estimated circular densities of saccade angles and quantified between-condition differences as the absolute area between the two densities over [–π, π]. In contrast, a permutation test, in which condition labels were shuffled, showed no significant difference in saccade direction between saccades in remembered and forgotten trials (p = 0.862).

We next trained a random forest classifier to predict memory encoding outcomes from SRND parameters derived from LFPs at individual electrode contacts, with each saccade labeled according to the memory outcome of the trial in which it occurred. This electrode-contact-level model learned location-dependent SRND-memory mappings, which formed the basis for a hierarchical prediction framework. Because we simultaneously recorded SRNDs from multiple electrode locations, and multiple saccades could occur during each image presentation, we can aggregate predictions across electrodes to yield saccade-level predictions, and then across saccades to yield trial-level predictions. This hierarchical approach enabled us to address three distinct questions about how SRNDs support memory encoding: (1) Are SRNDs at a single electrode location sufficient to predict memory outcome? (2) Is memory encoding jointly shaped by SRNDs across the brain? If so, aggregating prediction probabilities across electrode locations should improve prediction; and (3) Does aggregating predictions across saccades further improve

the prediction of the memory outcome of the viewed image. We address each of these questions in turn below.

To prevent the model from overfitting to subject-specific electrode coverage, we added normally distributed spatial jitter to electrode coordinates. To prevent the classifier from leveraging idiosyncratic properties of specific images for predicting memory outcome, we split our data at the trial level. Thus, all saccades and their associated SREPs during a given image presentation were confined to either the training or the test set, so the model was never exposed to SRND from the same presented image. Because the number of remembered and forgotten trials was imbalanced, we used balanced accuracy as our primary metric for evaluating model performance (**Supplementary Table 3**). In 5-fold cross-validation (CV), the trained model achieved 55.7% balanced accuracy and 70.3% accuracy at the electrode-location level, exceeding all values in the null distribution generated by permutating memory encoding outcome labels (**Figure 6d, Figure 6 - Figure Supplement 1a**). These results show that SRNDs at individual electrode locations carry information predictive of visual encoding.

To answer the second question of whether memory encoding depends on coordinated SRNDs across locations, we evaluated the predicted probability of successful memory encoding at the saccade level, defined as the predicted probability obtained from the trained random forest classifier and averaged across electrode contacts. Because this saccade-level predicted probability was continuous, classifying the memory outcome (remembered vs. forgotten) associated with each saccade requires a decision threshold. To evaluate classifier performance in a threshold-independent manner, we calculated the area under the ROC curve, which summarized sensitivity–specificity tradeoffs across all possible decision thresholds. The observed area under the ROC curve on test data (0.662) exceeded all values from its null distribution generated by training and evaluating models on data with permuted labels (**Figure 6E**). The observed saccade-level balanced accuracy corresponding to the optimal decision threshold was 62.6%, exceeding all values in its permutation-based null distribution (**Figure 6E**). Moreover, for each CV fold, both electrode-contact- and saccade-level balanced accuracy exceeded all values in their respective permutation-based null distribution (**Figure 6 – Figure Supplement 1F**). These results show that SRNDs across the brain jointly shape memory encoding.

To answer the third question of whether aggregating predictions across saccades further improves the prediction of the memory outcome, we computed the trial-level average predicted probability from SRND parameters across all electrode contacts and all saccades. We found that the trial-level predicted probability for testing data was higher in remembered trials, than in

forgotten trials (**Figure 6 – Figure Supplement 1c**, U statistic = 84652, $p < 0.001$, rank-biserial correlation = 0.333, $n_{remembered}$ = 635, $n_{forgotten}$ = 200, Mann–Whitney U test). At the trial-level, the observed testing area under the ROC curve was 0.678, and balanced accuracy was 63.1%, both exceeding all values in their respective null distributions (**Figure 6 - Figure Supplement 1b**, permutation test). Compared to the saccade-level model performance, aggregating SRND parameters across multiple saccades in a trial did not substantially improve memory outcome prediction

This finding suggested that successful memory encoding may not require that every saccade during image viewing be associated with encoding-conducive SRNDs. Because behavioral outcomes are shaped by the neural activities across sequential sensory events, it is possible that SRNDs cumulatively influence the memory encoding outcome[36]. We next asked whether the likelihood of remembering an image scales with the proportion of encoding-conducive SRNDs across saccades. Building on our validation that the classifier has learned SRND parameters associated with successful memory encoding, we computed the proportion of saccades that the model classified as occurring in remembered trials. We found that 75% of saccades in actual remembered trials were associated with encoding-conducive SRNDs, compared to 49% of saccades in forgotten trials, which were associated with encoding-conducive SRNDs (**Figure 6 – Figure Supplement 1D**). A chi-squared test of independence revealed a significant association between trial condition and predicted saccade labels ($\chi^2(1)$ = 217.89, $p < 0.001$). These results show that remembered trials had a greater proportion of SRNDs associated with successful memory encoding.

The conclusion that SRNDs contribute to visual memory encoding rests on the premise that the trained random forest was neither underfitting nor overfitting. To validate this premise, we systematically evaluated the influence of three key hyperparameters on model performance, including the number of trees, the maximum tree depth, and the minimum required leaf size. Leaf nodes are the terminal decision points of each tree, and their size controls how finely the model partitions the data. We reasoned that increasing tree depth and decreasing the minimum leaf size allowed the model to learn more complex relationships. Consistent with this reasoning, classifiers trained on SRND parameters with greater tree depth and smaller leaf size achieved higher training accuracy until saturation (**Figure 6F**), and critically, test accuracy rose in parallel with training accuracy and did not decline. For primary analyses, we used the default hyperparameters of the *imbalanced-learn* Python package (200 trees, maximum depth = 20, minimum leaf size = 1). Under this configuration, the model achieved relatively higher training and testing accuracy

compared to other configurations, and we observed no divergence between training and testing accuracy across the surrounding hyperparameter space, confirming that the classifier was neither underfitting nor overfitting (**Figure 6F**).

These results establish SRNDs as physiological correlates that support visual memory encoding.

Stronger and earlier SREPs predict recognition memory

We next sought to characterize the SRND profile associated with successful memory encoding. To understand how SRND parameters map onto memory outcomes, we applied Shapley additive explanation to the trained random forest classifier[37]. As we trained random forest classifiers using CV, we first ensured that the mapping learned by the classifier was consistent across CV folds by quantifying (1) the concordance of feature importance, (2) the similarity of decision boundaries, and (3) the agreement of model outputs across CVs. To establish statistical significance, we compared these metrics against their respective null distributions generated by permuting the memory encoding labels once to create a surrogate dataset, from which we trained random forest classifiers using 5-fold CVs.

To quantify the concordance of feature importance across CVs, we applied Kendall's coefficient on feature importance measured as Gini impurity reduction. The concordance coefficient across CV folds (Kendall's W = 0.966) for the actual data was higher than all values in the null distribution (mean Kendall's W = 0.439, SD = 0.110), suggesting that the models across CVs consistently identified the same features as important and weighted them similarly (**Figure 6G**).

To examine whether our random forest classifiers' decision thresholds were consistent across CVs, we compared split histograms between pairs of CV folds and quantified their similarity using the area under the absolute difference curve. A split histogram, which represents the distribution of decision thresholds across features, captures the decision boundaries. The split histogram for models trained on actual data across CVs were more similar than the null distribution generated based on permuted data (U = 0.000, $p < 0.001$, Mann-Whitney U test, Cohen's d = -3.398, $n_{actual} = 10, n_{null} = 100$), suggesting that random forests trained on actual data exhibit consistent decision boundaries across CV folds (**Figure 6H**).

To assess whether random forest models trained on actual data yield consistent predictions across CVs, for each pair of models trained in different CV folds, we randomly sampled observations from the test set in one model and used it as input to both models. We used

Pearson's correlation coefficient between the predicted probabilities of successful memory encoding from a pair of models to quantify the output agreement between the two models. We repeated this procedure for models trained on actual data and on models trained on a dataset generated by permuting labels. Models trained on actual data had higher output agreement across CV folds than those trained from permuted data (**Figure 6I**, U = 40000, p < 0.001, Mann-Whitney U test, Cohen's d = 5.208, $n_{actual} = 200, n_{null} = 200$). For a pair of models trained on actual data in different CV folds, we also quantified the proportion of testing samples with different predictions. This proportion was significantly lower than the null distribution derived from models trained with permuted data (**Figure 6 – Figure Supplement 1H**, U = 0, p < 0.001, Mann-Whitney U test, Cohen's d = -7.656, $n_{actual} = 200, n_{null} = 200$). Together, these results demonstrate that the mapping learned by the random forest classifiers between SRND parameters and memory outcome generalizes across CV folds.

Given this generalizability, we calculated Shapley values from a randomly selected fold to determine how each SRND parameter contributed to the predicted probability of successful memory encoding. Shapley values quantify how much a given feature value increases or decreases the probability of successful memory encoding for individual observations, while accounting for correlations between features (see **STAR Methods** - Shapley additive explanation). **Figure 7A** shows, for a representative electrode contact in the superior temporal gyrus, how Shapley values varied as a function of each SRND parameter's observed value. To illustrate that the obtained Shapley values captured how the trained classifier predicted memory outcome from SRND parameters, we compared the relationship between each SRND parameter's observed values and their corresponding Shapley values to two characterizations of the model's decision structure. First, we compared this relationship for each SRND parameter to its partial dependence plot, which quantifies the average predicted probability across observed values, independently of the other parameters (**Figure 7B**). Second, we compared the SRND parameter value — Shapley value relationships to model-predicted probabilities across the parameter space. To obtain the model-predicted probabilities, we systematically varied the SRND parameters and passed their combinations together with the electrode contact coordinates as inputs to the trained random forest classifier (**Figure 7C**). These two comparisons show generally consistent SRND parameter value — Shapley value relationships and predicted probability of successful memory encoding, for example, at this representative contact, higher preceding oscillatory power was associated with lower Shapley values and lower predicted probability of successful memory encoding (**Figure 7B-C**).

To summarize the learned mapping between SRND parameters and visual memory encoding in interpretable terms, we constructed a lower-dimensional representation of the SRND parameter value - Shapley value relationship for each parameter and each electrode contact. This representation consisted of a threshold and a direction derived from Shapley values, partitioning each SRND parameter into encoding-conducive and non-encoding-conducive ranges (see **STAR Methods** - Shapley value-informed thresholds and directions). This representation reduces the decision trees in the trained random forest classifier to a single decision boundary per parameter and location (**Figure 7D**).

To confirm that Shapley value-informed thresholds and directions captured a meaningful relationship between SRND parameters and memory outcome, we compared recall likelihood between remembered and forgotten trials, a probabilistic measure of successful memory encoding derived from Shapley value-informed thresholds and directions (see **STAR Methods** - Shapley value-informed thresholds and directions). We found that recall likelihood averaged across electrode contacts was significantly higher in remembered trials compared to forgotten trials (**Figure 7D,** $N_{remember} = 3052$, $N_{forgotten} = 906$, U = 1.872×10^6, p < 0.001, Mann-Whitney U test, rank-biserial correlation coefficient = 0.354). We next assessed whether Shapley value-informed thresholds and directions predicted successful memory encoding. To assess whether this prediction exceeded what would be expected from arbitrary thresholds, we performed surrogate testing by randomly sampling thresholds from the observed feature values. For each saccade, we compared the recall likelihood of every SRND parameter at every electrode contact against a baseline probability of 0.5. The balanced accuracy for individual SRND parameters based on actual Shapley value-informed threshold and direction was significantly higher than the surrogate control ($N_{observation} = 2707$, $N_{control} = 5414$, p < 0.001, t-test, Cohen's d ranged from 0.296 to 0.390). When we leveraged recall likelihoods across all SRND parameters for each saccade (i.e., classifying an instance of SRND as encoding-conducive if the majority of parameters exceeded 0.5), the actual balanced accuracy was significantly higher than the control ($N_{observation} = 2707$, $N_{control} = 5414$, U = 9.767×10^6, p < 0.001, Mann-Whitney U test, Cohen's d = 0.571). **Figure 7 – Figure Supplement 1A** shows the area under the ROC curve for classifying whether SRNDs recorded at an electrode contact during a saccade occurred in a remembered or forgotten trial, based on recall likelihoods. The area under the ROC curve was significantly higher using recall likelihood based on actual Shapley value-informed threshold and direction ($N_{observation}$ = 2707, $N_{control}$ = 5414, p < 0.001, Mann-Whitney U test, U = 1.067×10^7, Cohen's d = 0.817), compared to the surrogate control. These results demonstrate that Shapley

value-informed thresholds and directions provide an interpretable summary of the SRNDs associated with successful visual memory encoding

Our findings that SRNDs across the brain better predict memory outcome than SRNDs in a single location suggest that successful memory encoding is supported by brain-wide SRNDs. If the Shapley value-informed thresholds and directions accurately identify the range of encoding-conducive SRND parameters at each location, then the extent to which encoding-conducive SRNDs are present across locations should better predict, for each saccade, whether the viewed image was recognized. To test this hypothesis, we calculated for each saccade the proportion of SRND parameters that fell within the location-specific, Shapley value–informed encoding-conducive ranges across all electrode locations. To evaluate the prediction performance, we constructed an ROC curve by varying the proportion threshold. The averaged area under the ROC curve across subjects was 84.9%, exceeding all values in the control distribution generated by randomly sampling thresholds from the feature values (**Figure 7F**, rank-biserial correlation = 1.000, Cohen's d = 6.789). The average balanced accuracy at the optimal proportion threshold across subjects was 77.9%, which also exceeded all values in the control distribution (rank-biserial correlation = 1.000, Cohen's d = 8.761). Notably, Shapley values–informed thresholds and directions better predicted successful visual encoding at the saccade level than the random forest classifier trained on SRND parameters (**Figure 6E**). This result shows that the threshold–direction representation, by distilling the complex decision rules of the random forest into a single decision boundary, may better capture the generalized mapping between memory encoding and SRNDs.

Using SRND parameters across saccades as inputs to the trained random forest classifier did not substantially improve the prediction of memory outcome. If Shapley value–informed thresholds and directions faithfully represent the SRND parameter-memory outcome relationship learned by the random forest classifier, trial-level prediction using these thresholds and directions should similarly not improve beyond saccade-level prediction. We applied the same procedure described above, that is, calculated the proportion of SRND parameters falling within location-specific encoding-conducive ranges, now extended across all saccades within a trial. At the trial level, the area under the ROC curve and optimal balanced accuracy of separating remembered from forgotten trials using Shapley value–informed thresholds and directions were 0.801 and 0.732, respectively (**Figure 7 – Figure Supplement 1B**). While these two model performance metrics exceeded all values in the surrogate control distribution, they did not surpass saccade-

level prediction, which supports that Shapley values–informed thresholds and directions capture the relationship between SRNDs and successful memory encoding

We next used Shapley values–informed thresholds and directions to identify brain regions where SRNDs most strongly influenced visual memory encoding. For each electrode contact, we computed the mean absolute Shapley value across saccades to quantify how strongly that contact's SRND parameters contributed to the memory outcome. The mean absolute Shapley values for SRND parameters across CV folds were consistent with feature importance based on Gini impurity reduction (**Figure 6G**), and consistent across CV folds (**Figure 6 – Figure Supplement 1G**, Kendall's coefficient of concordance = 0.966, p = 0.0, permutation test). We ranked the average values across electrode contacts within a functional-anatomical region to assess the spatial distribution of influence (**Figure 7G**). We found that SRNDs in the frontal and parietal regions had the strongest influence on visual encoding (**Figure 7H**). Regional averages may obscure within-region heterogeneity. Therefore, we additionally visualized mean absolute Shapley values at the electrode contact level (**Figure 7 – Figure supplement 1C**, see **STAR Methods** - Visualization of the SRND-visual encoding relationship), which confirmed that SRNDs in frontal and parietal cortices and nearby white matter had the strongest influence on visual encoding.

Finally, we delineated the SRND profiles associated with successful visual encoding by quantifying Shapley value–informed thresholds and directions for each SRND parameter across the brain (**Figure 7I–M**). SREPs with higher magnitude, especially in frontal and parietal regions, were associated with successful encoding (**Figure 7I**). This was consistent with the electrode contact-level SREP magnitude profile associated with successful visual encoding shown in **Figure 7 – Figure Supplement 1D**. Earlier SREP latencies across the cerebrum were associated with successful encoding (**Figure 7J, Figure 7 – Figure Supplement 1E**). Later SREP peak times in the left hemisphere were associated with successful visual encoding (**Figure 7K**, **Figure 7 – Figure Supplement 2A**). Oscillation power at 0.5 OCs before SREP onset latency showed hemispheric asymmetry: lower power in the left hemisphere and higher power in the right hemisphere were associated with successful encoding (**Figure 7L, Figure 7 – Figure Supplement 2B**). At the same pre-SREP timepoint, oscillation in the trough-to-peak rising phase (i.e., $[-\pi, 0]$ radians) was associated with successful memory encoding across most brain regions, regardless of SREP polarity (**Figure 7M, Figure 7 – Figure Supplement 2C, Figure 7 – Figure Supplement 3A–B**). We refer to this range of oscillation phase as the encoding-conducive phase interval. Because the pre-SREP oscillation phase was coupled with SREP polarity, it is possible

that the encoding-conducive phase interval was disproportionately populated by SREPs of one polarity, which would predict a memory encoding outcome difference between polarities. Contrary to this prediction, across electrode contacts, memory encoding outcome associated with positive and negative SREP did not differ (mean [95% CI from bootstrapping]: Positive, 74% [73%, 75%]; Negative, [73%, 75%]). To identify the source of this contradiction, we examined the joint distribution of oscillation phase and the corresponding Shapley values. Across electrode contacts, although pre-SREP phase distributions differed between positive and negative SREPs (centering near 0 for negative SREPs and near π for positive SREPs), the encoding-conducive phase interval was similar across polarities (**Figure 7 –Figure supplement 3C–D**). Shapley value for the pre-SREP oscillation phase showed subtle distributional differences between polarities: moderate positive Shapley values ($\approx$0.01) were more probable for negative-polarity SREPs, whereas higher Shapley values ($\approx$0.03) were more probable for positive-polarity SREPs (**Figure 7 –Figure supplement 3E**). These differences balanced out, yielding equivalent memory encoding outcomes across SREP polarities.

Shapley value analyses reveal that SREP profiles marked by early latency and strong amplitude are associated with successful visual memory encoding.

SREPs did not encode saccade direction

We have demonstrated that SREPs reflect neural states supporting visual encoding and characterized their profiles associated with successful visual encoding. The remaining question is whether these SREPs represent saccadic corollary discharge or a novel memory-related mechanism. If SREPs were a narrowly defined corollary discharge signal, they should convey information about saccade direction. We tested this hypothesis using random forest regressors to examine whether SRND parameters could predict saccade direction (see STAR Methods - **RF regression for predicting saccade direction**). Because saccade direction is a circular variable, we transformed saccade direction θ into a continuous vector $[sin(\theta), cos(\theta)]$, which allows the use of Euclidean distance as a loss function while preserving the circular nature of the variable. **Figure 8A** illustrates the model architecture and training and evaluation pipeline.

To assess whether SRNDs contained information about saccade direction, we compared the model's prediction error on held-out testing data to null distributions generated by permuting saccade directions. Across 5-fold CVs, the observed testing mean squared error (MSE) for $sin(\theta)$ fell at the 65th percentile of the null distribution, and that for cos(θ) fell at the 93rd percentile (**Figure 8B**). We obtained the predicted saccade direction using the two-argument arctangent function, $atan2$, and found that the mean absolute angular error between predicted and true saccade

direction was higher than the surrogate control distribution, which indicated that SRND parameters were not predictive of saccade direction (**Figure 8C**). We next assessed if leveraging SRND parameters across electrode contacts could reveal directional encoding. For each saccade, we obtained the prediction of saccade direction based on the predicted $[sin(\theta), cos(\theta)]$ vectors averaged across electrodes (**Figure 8D**). The testing mean absolute error (MAE) corresponded to the 52nd percentile of the null distribution, indicating chance-level performance. To verify that this result was not due to suboptimal hyperparameter choices, we systematically evaluated the effect of key hyperparameters, including the number of trees, the maximum tree depth, and the minimum leaf size, on model performance. Although increasing the maximum depth and decreasing the leaf size allowed the model to be more complex and better fit the training data, the electrode contact-level and saccade-level model performance on the testing data remained consistently poor, suggesting that the failure to predict saccade direction was not due to model limitations (**Figure 8 – Figure Supplement 1A**). These results provide initial evidence that SRND parameters do not encode saccade direction information.

Subsequently, we examined whether SRNDs in any contacts contained directional information by determining for each contact, the percentile rank of its saccade-level testing MSE within its respective null distribution. Only 5% of electrode contacts achieved a testing MSE below the 5th percentile of their null distribution (**Figure 8E**). We used permutation testing to identify direction-informative electrode contacts by comparing the percentile rank of each contact's saccade-level test MSE within its null distribution against a Bonferroni-corrected significance threshold (α = 0.05). **Figure 8F** shows the ratio of saccade direction-informative electrode contacts across anatomical regions. No region exceeded a 3% ratio of direction-informative electrode contacts, except for the brainstem (13%, one of the eight microwires near the left hippocampus and brainstem showed directional information)**.** To determine which SRND parameter showed directional modulation, we estimated the circular kernel density of the SRND parameters' values as a function of saccade direction (**Figure 8F**). For each SRND parameter, we quantified directional modulation as the non-uniformity of feature values across angular space, measured as the integral of the absolute deviation from the mean. **Figure 8G** shows the distribution of non-uniformity for the five SRND parameters. We compared them against the null distribution generated by shuffling SRND-direction pairings. For all five SRND parameters, the non-uniformity value in more than 95% of electrode contacts was below the 95th percentile of their respective null distributions (**Figure 8G**). These results suggest that most, if not all, SRNDs across the brain do not convey information about saccade direction.

To confirm that the absence of directional information in SRND parameters was not an artifact of the model architecture, learning target, or prediction granularity, we implemented a series of control models: (1) a fully connected neural network predicting the trigonometric representation of saccade direction, (2) a neural network trained to minimize angular loss, (3) a von Mises kernel regression, and (4) a random forest classifier for binary saccade direction (left vs. right). We obtained null distributions of performance metrics from these models trained on permuted data.

The first control model, a neural network, predicted the sine and cosine of the saccade direction using SRND parameters and electrode coordinates (**Figure 8 – Figure Supplement 1B**, see **STAR Methods**). The observed electrode contact-level mean squared errors (MSEs) for $sin(\theta)$ and $cos(\theta)$ were 0.924 and 1.035, corresponding to the 71st and 28th percentiles of their respective null distributions (**Figure 8 – Figure Supplement 1C**). The MSEs for saccade directions were 10404 and 10263 deg^2 at the electrode contact and saccade levels, corresponding to the 28th and 30th percentiles of their null distributions, respectively (**Figure 8 – Figure Supplement 1D**).

The second control model, a neural network, used the same architecture as the first control model but with an angular loss function to ensure that the model training was not constrained by the trigonometric target representation (**Figure 8 – Figure Supplement 1E**). This model yielded MSEs of 1066 and 10581 deg^2 at the electrode-contact and saccade levels, corresponding to the 17th and 37th percentiles of their null distributions, respectively (**Figure 8 – Figure Supplement 1F**).

The third control model used von Mises kernel regression, which natively handled the circular dependent variable (i.e., saccade direction) (see **STAR Methods** - Kernel regression by minimizing the von Mises negative log-likelihood). This model also failed to predict saccade direction above chance, with MSEs of 10783 and 10520 deg^2 at the electrode contact and saccade levels, corresponding to 22nd and 22nd percentiles of their null distributions (**Figure 8 – Figure Supplement 1G**).

The fourth control model, a random forest classifier, predicted binarized saccade direction (i.e., left vs. right). This approach reduced the complexity of the prediction problem and paralleled our earlier prediction of successful visual encoding (**Figure 6C**). This random forest classifier performed at the chance level. The electrode contact-level balanced accuracy was 0.501, corresponding to the 83rd percentile of its null distribution. The saccade-level area under the ROC

curve and balanced accuracy were 0.517 and 0.502, corresponding to the 52nd and 73rd percentiles of their null distribution, respectively. (**Figure 8 – Figure Supplement 1I**). The absence of directional information in SRND parameters was robust across all four models and learning schemes.

To further distinguish SREPs from corollary discharge, we assessed whether SREPs reflected the motor planning for the subsequent saccade, that is, whether they encoded the direction of the upcoming saccade. We trained and evaluated random forest regressors for predicting the direction of the next saccade using SRND parameters and electrode locations. The electrode contact-level and saccade-level mean absolute errors were 90° and 90°, respectively. These errors corresponded to the 42nd and 39th percentiles of the null distribution, respectively, suggesting that SREPs were unlikely to reflect prospective oculomotor planning.

These converging analyses demonstrate that SRNDs do not encode saccade direction, ruling out an interpretation of SRNDs as a corollary discharge signal.

Discussion

Here, we provide direct evidence that SREPs represent saccadic modulation of large-scale neural activity, rather than muscular activities in humans. Corroborating this interpretation, we demonstrate an interplay between SREP waveforms and ongoing oscillatory neural activities throughout the brain. Our explanatory analysis based on machine learning models validates the hypothesis that SREPs contribute to visual memory encoding and confirms the absence of directional tuning in SREPs. We identify SREP profiles associated with successful visual encodings. Coordination between active sensing mechanisms (e.g., saccades, sniffing, echolocation) and underlying neural activity is commonly found across species (e.g., non-human primates, rodents, and bats), presumably to optimize information processing[20,38,39]. Our findings demonstrate that an analogous mechanism exists to support human visual encoding: larger SREPs likely reflect a transient increase in synchronized synaptic activity, creating a network state favorable for visual memory encoding. These findings position SREPs as potential targets for memory-enhancing neuromodulation, for example, through interventions that amplify SREPs at saccade times.

Presence, spatiotemporal structure, and behavioral relevance of SREPs

The novelty of our study lies in the shift from stimulus-locked responses to saccade-timed neural dynamics, demonstrating that SREPs are present, spatiotemporally organized, and behaviorally

relevant. Studies of neural mechanisms in human visual encoding have focused on brain responses to various visual stimuli[40,41]. Although SREPs were previously reported and have been shown to modulate neural activity in non-human primates, direct evidence that these findings translate to humans has remained scarce[7,42,43]. This knowledge gap persists due to methodological constraints, such as the limited availability of human intracranial LFPs and the potential contamination of ocular-muscular artifacts in non-invasive electrophysiology. We leveraged a unique research opportunity in neurosurgical patients undergoing intracranial monitoring, and our findings provide direct evidence for the presence of SREPs in humans. These results corroborate and extend a recent study conducted by Staudigl et al., which showed that saccades coordinated amygdala-hippocampus interactions in humans[44]. When considered alongside findings from non-human primates, the available data suggest that saccadic modulation operates at multiple physiological scales, including neuronal spiking, evoked potentials, oscillations, and functional connectivity[8,39,45]. Likewise, we observed consistent SREPs, along with increased phase synchronization and increased oscillation power following saccades. Our findings that SREP waveforms are systematically associated with the phase of ongoing oscillations (**Figure 4**) suggest that neural dynamics across scales at the time of saccades may reflect a latent state indexing attention or readiness for visual processing. Validating this hypothesis is important because, if correct, it would unify saccade-related neural phenomena into a coherent mechanistic framework. This hypothesis makes two falsifiable predictions: (1) experimentally inducing saccades at different phases of ongoing oscillations affects other saccade-related neural dynamics, and (2) the encoding of other sensory information, such as auditory encoding, is enhanced when SREP profiles mirror those associated with successful visual encoding.

Previous studies of saccade-related neural dynamics have primarily focused on the visual system, where they were studied as mechanisms of visual perception, more specifically, perceptual stability[46,47]. More recent work has extended this scope, showing that saccades modulate neural activity beyond the visual system, including the medial temporal lobe[32], the thalamus[48], and the auditory cortex[22]. These findings suggest saccade-related neural dynamics may serve broader cognitive functions beyond visual perception. These studies primarily focused on individual brain regions, potentially missing coordinated saccadic modulation across the brain. Our study demonstrates widespread SREPs across the human brain and reveals their systematic spatiotemporal organization through whole-brain spatiotemporal profiling. Earlier SREPs with greater amplitude emerged in the temporal lobe, a region implicated in high-order visual processing[49], followed by later SREPs across parietal and frontal regions (**Figure 5 –**

supplementary video). This pattern suggests a cascading dynamic across regions that coordinate visual perceptual and encoding processes over time, which aligns with emerging evidence that cognitive representations are neither strictly localized nor ubiquitously distributed, but rather reflected broadly across the brain[50,51].

We interpret these results as follows. Early SREPs likely reflect the reconfiguration of the temporal lobe network, which may facilitate high-level visual processing[44]. After visual inputs are integrated into meaningful percepts, fronto-parietal networks mediate downstream encoding processes through information integration, working memory, and attention regulation[52,53]. Supporting this interpretation, SREPs in frontal and parietal regions exhibit the strongest influence on visual encoding performance (**Figure 7G and H**). Notably, our dataset has limited coverage within the early visual cortex, which constrains our ability to determine whether a latency gradient exists along the visual processing hierarchy. Even within this limitation, our findings provided convincing evidence that SREPs serve visual memory encoding, consistent with the view that human vision is an active sensing process[54]. Conceptually, our results invite a novel model of visual cognition. Instead of being a feedforward transformation of retinal input through the visual hierarchy, visual cognition involves neural events at saccade times that constitute a coordinated, whole-brain mechanism. We refer to these neural events as SREPs because, although our results show temporal consistency of LFP waveforms around saccades, they are correlational in nature. Without causal manipulation of saccades, it remains an open question whether saccades drive these neural dynamics or whether an underlying internal state coordinates both.

Implications for studying active visual memory encoding in humans

Our study has three primary implications for neuroscientific studies of active visual encoding in humans. First, we encourage research to adopt active-viewing paradigms and incorporate eye-tracking, as these approaches capture the dynamics of human visual processing in naturalistic settings. Second, intracranial recordings in neurosurgical patients, such as those undergoing epilepsy monitoring, can reliably capture saccade-related neural dynamics that are free of oculomuscular contamination. Third, as saccades coincide with multiple processes, such as motor commands, shifts in retinal input, and cognitive processes, careful analytical dissociation is needed to attribute neural signals to behavioral and cognitive relevance. Our study showcases two key analytical strategies to address this challenge. We examined neural activity during saccades while subjects attended to a blank screen to control retinal input. This analysis reveals that these SREPs are largely non-visually mediated, consistent with previous studies in non-human primates and cats[9,55]. Additionally, we separately correlated SREP characteristics,

extracted from LFPs and EOG, with saccadic behavior measures, such as saccade direction, thereby ruling out any potential confound introduced by EMG activity. Below, we present additional control analyses and discuss their implications.

To quantify the duration for which SREP waveforms remained consistent across trials, we systematically varied the window size and compared the distributions of intertrial correlation. We defined the pre-saccadic epoch as starting 1 second prior to saccade onset and with the same length as the peri-saccadic epoch (**Figure 2 – Figure Supplement 4A**). To quantify SREP consistency differences between pre- and peri-saccadic epochs, we computed the difference in the area under the cumulative distributions of the intertrial correlation curve (AUC) as follows: for correlations smaller than the crossing point, we calculated the difference by subtracting pre-saccade AUC from peri-saccade AUC; for correlations greater than the crossing point, we calculated the difference by subtracting peri-saccade AUC from pre-saccade AUC. Aligning with the main findings, we found that SREPs were more consistent than pre-saccadic LFPs (**Figure 2 – Figure Supplement 4B**, $t = 5.349$, $p < 0.001$, Cohen's $d = 0.274$, $n = 382$, two-sided t-test). This result is consistent across window length (**Figure 2 – Figure Supplement 4B)**. Interestingly, distributions of intertrial correlations were less normally distributed when the analysis windows were shorter, for both pre- and peri-saccadic EP (**Figure 2 – Figure Supplement 4B**).

These results imply that SREPs are transient. As we increased the window length, we incorporated ongoing activity unrelated to the saccade, thereby reducing waveform consistency. The same pattern observed in the pre-saccadic neural field potentials may result from coordinated visual memory encoding processes before saccades. Our observed clustering of oscillation phases preceding saccades supports this view (**Figure 4D**). A separate methodological concern is that shorter windows, by including fewer data samples, may yield extreme intertrial correlation values[56]. To rule out this possibility, we performed an additional surrogate analysis by shuffling data for each saccade to extract pre- and peri-saccadic LFP waveforms. We found that the separation effect size, which measures how peri-saccadic LFP differs from baseline LFP, was significantly reduced in surrogate data compared to real data ($t = -65.086$, $p < 0.001$, Cohen's $d = -1.804$, two-sided t-test, $n = 2604$, **Figure 2 – Figure Supplement 4C**). The above analyses suggest that the LFP waveform following saccades is not spontaneous but represents consistent saccadic modulation. This conclusion is further supported by our finding that SREPs predicted successful visual encoding.

We evaluated the random forest classifier's generalizability to individual subjects by computing electrode-contact- and saccade-level balanced accuracies, averaged across cross-

validation iterations, separately for each subject's test data. For each subject, we generated a null distribution of balanced accuracy using models trained on permuted labels. **Figure 6 – Figure Supplement 1E** shows the percentile rank of balanced accuracy relative to the null distribution for each subject. The observed saccade-level balanced accuracy exceeded the null distribution in 6 out of 8 subjects, indicating relatively good generalizability. For the remaining two subjects, saccade-level balanced accuracy corresponded to the 83rd and 72nd percentiles of the null distribution, indicating performance above chance but with limited generalizability. This is not unexpected. Although the full cohort provided broad coverage across the cerebrum, electrode coverage for individual subjects was often more limited, for example, restricted to a single hemisphere depending on the suspected seizure onset zone. We also note that these two subjects had the fewest valid remembered and tested visual encoding trials (12 and 14), which might limit the model's ability to fully learn the mapping between SRND parameters and successful encoding in the brain regions sampled in these individuals.

Because the anatomical organization of brain regions and their associated functions is highly complex and not expected to follow a linear mapping, we used non-linear models (i.e., random forest models) to learn the mapping from SRND parameters recorded at specific brain regions to visual encoding. We were interested in whether there is a linear relationship between the SRND parameters and visual encoding. For this purpose, we trained logistic regression models using the same inputs and labels as in training random forest models, except that we substituted peak-to-trough amplitude with its absolute value. This was done to avoid multicollinearity, as polarity information is already captured by the preceding oscillation phase. The logistic regression performed well above chance, but not as well as the random forest model (**Figure 6 – Figure Supplement 1I**). For testing data, the electrode-contact-level balanced accuracy was 53.1%, the saccade-level ROC AUC was 63.2%, and the saccade-level balanced accuracy was 59.5%. Assuming a linear relationship, the weight coefficient for each SRND parameter indicates that a higher absolute SREP peak-to-trough value was associated with remembered trials, aligning with the mapping identified in the random forest models (**Figure 7I**).

Proposed mechanisms underlying SREPs and their relationship with successful visual encoding

Our investigation was motivated by Katz et al., who reported saccade-related inhibition of single units in mnemonic structures and interpreted it as a corollary discharge-like signal[8]. While our study built upon their findings, our results reveal a distinct form of saccadic modulation. Specifically, our study provides direct evidence for the role of SREPs in visual encoding. Moreover,

the observed SREPs did not systematically encode saccade direction, which is a hallmark of corollary discharge. Our findings thus suggest that neural dynamics following saccades are another form of saccadic modulation that is more consistent with the active sensing framework and the study by Leszczynski et al. in non-human primates[22]. The existing literature and our results suggest two mechanistically distinct forms of saccadic modulation: (1) an early corollary discharge, and (2) a later modulation of neural activity to support visual encoding[39,57,58].

Within the active sensing framework, a theory proposed that saccades modulate sensory processing by resetting ongoing oscillations to a high-excitability phase[3]. Our results suggest an alternative, but not mutually exclusive, mechanism of SREPs. We observed SREPs with positive and negative polarities at the same recording sites, and their waveform depends on the ongoing oscillation phase. As these SREPs were derived from locally re-referenced field potentials, they reflected the mesoscale current flows driven by synchronized synaptic currents[59]. Based on this, we propose a model in which each brain region follows its intrinsic rhythm, with saccades acting as events that synchronize neural activity in a manner contingent on the local rhythm. The consistent LFP waveforms time-locked to saccades may result from the temporal coordination between saccade and intrinsic brain rhythms. This interpretation is supported by observations of phase clustering before saccades shown in this study (**Figure 4**) and in other studies[32,60]. This model predicts higher intertrial coherence and elevated oscillatory power at saccade times, which are also validated in our study and previous work[3,22]. Given that SREP is a brain-wide phenomenon, a global, uniform phase reset would likely interfere with ongoing neural computations, for example, information coding[61]. Thus, a phase-contingent synchronization mechanism for processing incoming input may be functionally more beneficial.

All visual inputs are not remembered equally[62]. Our study shows that SREP characteristics and ongoing oscillations explain this variability. Notably, the proportion of SRNDs associated with successful encoding was below 100% in remembered trials, suggesting that not every saccade in a remembered trial occurred in a neural state conducive to encoding. In forgotten trials, not all saccades were predicted to be associated with unsuccessful encoding, implying that even when recognition ultimately failed, transient neural states supportive of encoding can still arise but may be insufficient or poorly timed to drive successful visual memory encoding. We distilled the SRND parameter–encoding relationship learned by the random forest model into a lower-dimensional space defined by thresholds and direction rules derived from Shapley values. The extrapolated mapping predicted successful memory encoding slightly better than the random forest classifier, suggesting that this representation preserves and identifies a more generalizable mapping

between visual encoding and SREPs. The lower-dimensional representation provides a foundation for interpreting the relationship between SRND parameters and visual encoding. Specifically, successful encoding was associated with greater SREPs amplitude, particularly in frontal and parietal regions (**Figure 7I**). It is our interpretation that stronger SREPs represent greater attention and may signal priority for encoding in memory circuits[63]. In addition, successful encoding is associated with earlier SREPs in general, which mirrors Staudigl et al.'s finding that neuronal responses in the medial temporal lobe associated with remembered images occurred earlier than those associated with later forgotten images[44]. These findings suggest that earlier saccadic modulation is beneficial for visual encoding, although the exact mechanism remains to be elucidated.

Previous studies have demonstrated that greater oscillation power in the hippocampus was associated with better recognition memory in non-human primates[3]. Our results provide a whole-brain mapping between oscillatory activities and successful visual encoding. The normalized oscillation power at 0.5 OCs before SREP onset latency showed hemispheric asymmetry. In general, lower preceding power in the left hemisphere and higher power in the right hemisphere were associated with successful encoding. If SREPs represent synchronization, contingent on local rhythm, then regions in which higher preceding oscillation power predicts successful encoding likely belong to the encoding-relevant network. In other words, their ongoing rhythmic activity is functionally aligned with visual encoding. We caution that the functional meaning of oscillation is frequency- and region-dependent. For example, increased posterior alpha oscillations in the visual cortex have been linked to an enhanced signal-to-noise ratio via selective inhibition of background activity[54], whereas increased hippocampal theta oscillations are associated with active information encoding[65,66]. Given that the dominant frequency across cerebrum resides in the theta–alpha range (5–12 Hz; **Figure 4 –Figure Supplement 1D**), it is plausible that both inhibitory gating and encoding mechanisms are at play.

Conclusion

Our study establishes SREPs as saccadic modulation of large-scale neural activities that predict human visual memory encoding. What determines whether a visual input is encoded into long-term memory has been attributed to stimulus salience, top-down attention, amygdala-mediated emotional regulation, and hippocampal-dependent consolidation[67–70]. Our findings add saccadic modulation of neural activity to this set of mechanisms. We speculate that SREPs reflect a saccade-coupled form of top-down modulation, by which the brain supports visual memory encoding; though its precise relationship to canonical attentional processes remains to be

determined. Causal manipulations, such as brain stimulation timed to saccades to disrupt SREP, will be critical to confirm this speculation. Regardless of how SREPs map onto existing cognitive frameworks, such as attention, the encoding-conducive SREP profile identified in our study, characterized by earlier onset latency and greater peak amplitude, provides a measurable target for memory-enhancing neuromodulation. Together, these findings extend the active sensing framework to human visual memory encoding: each shift in gaze is accompanied by a structured neural event that influences whether the encountered visual world is remembered.

Resource availability

Lead contact

Requests for further information and resources should be directed to, and will be fulfilled by, the lead contact, Peter Brunner (pbrunner@wustl.edu).

Materials availability

This study did not generate new unique reagents.

Data and code availability

All analysis scripts and data for statistical analysis and figure plotting are available on a GitHub repository (https://github.com/GanshengT/Saccade-related-evoked-potential-predicts-visual-memory). Raw imaging and electrophysiological data can be de-identified and provided to qualified researchers upon request, given the large file size (~95 TB) and in accordance with our IRB-approved protocol. Anonymized data for one subject, and a script illustrating the data-processing pipeline are available on a GitHub repository (https://github.com/GanshengT/Saccade-related-evoked-potential-predicts-visual-memory).

Acknowledgements

This work was supported by NIH/NIMH (R01-MH120194), NIH/NIBIB (P41-EB018783, R01-EB026439), McDonnell Center for Systems Neuroscience, Fondazione Neurone, NIH/NINDS (U24-NS109103, U01-NS108916, U01-NS128612, R21-NS128307), and NIH/NEI (R01-EY037195). The manuscript was edited by the Scientific Editing Service of the Institute of Clinical and Translational Sciences at Washington University, which is supported by an NIH Clinical and Translational Science Award (UL1 TR002345).

Author contributions

Conceptualization: G.T.; Data curation: G.T., P.B., and J.T.W.; Formal analysis: G.T.; Funding acquisition: E.C.L., P.B., J.T.W., C.S.I., J.R.M., and S.B.H.; Investigation: G.T., P.B., J.T.W., and E.C.L.; Methodology: G.T., P.D., H.C., Y.L., and Z.L.; Software: G.T., P.B., and J.R.S.; Supervision: P.B., J.T.W., and E.C.L.; Validation: G.T., P.B., H.C., P.E.C., S.S.S., H.P., X.L., Z.L., and E.C.L.; Visualization: G.T., P.D., and P.B.; Writing – original draft: G.T.; Writing – review & editing: G.T., J.T.W., P.B., and E.C., Task design: J.R.S., K.L.W., M.K.H., and J.M.C.

Declaration of interest

Eric Leuthardt holds equity in Aurenar Inc. Gansheng Tan, Peter Brunner, and Eric Leuthardt filed a provisional patent related to this work in November 2025 (Application number: 63/910,588). The other authors declare no competing interests.

Declaration of generative AI and AI-assisted technologies in the writing process.

During the preparation of this work, the author(s) used ChatGPT and Grammarly AI in order to improve the readability of the manuscript. After using these tools, the authors reviewed and edited the content as needed and take full responsibility for the content of the published article.

STAR Methods

Experimental model and study participant details

Eight epilepsy patients (two males and six females) undergoing intracranial monitoring with stereoelectroencephalography (SEEG) at Washington University School of Medicine participated in this study. All participants provided written informed consent in accordance with protocols approved by the Institutional Review Board at Washington University in St. Louis (IRB protocol number: 202104033-1001). Patients were eligible for this study if they were diagnosed with epilepsy and scheduled to undergo intracranial video monitoring for seizure onset localization. None of the included patients reported subjective cognitive impairment, and no abnormalities in eye movements were noted during clinical evaluation. Patient demographics and seizure diagnosis are described in **Supplementary Table 2 Patient Characteristics**.

Electrode implantation and clinical procedure

All patients underwent implantation of multi-contact depth electrodes (sEEG Depthalon depth electrode, PMT® Corporation, MN, USA) for seizure monitoring. Each electrode had 8–16 contacts (2 mm cylindrical contacts length, 0.8 mm diameter, spaced 3.5 mm apart center-to-

center). In 6 patients, two hybrid depth electrodes with macro- and micro-contacts (Behnke Fried Depth Electrode, Ad-Tech® Medical Instrument Corporation) were implanted. Each hybrid depth electrode has a microwire bundle in addition to 8 standard macro contacts. The microwire bundle consists of nine 40-μm-diameter wires, which were trimmed to extend up to 5 mm beyond the tip of the macroelectrode during implantation. Eight of the microwires are coated in polyamide insulation up to the tip, resulting in an impedance of 100–300 kΩ; the ninth microwire is uninsulated, serving as a reference.

The clinical team planned the electrode placement to ensure appropriate coverage of the brain for seizure network localization. T1-weighted imaging (MPRAGE sequence, voxel size $1.0 \times 1.0 \times 1.0\,mm^3$) was obtained in the presurgical workup and loaded into the planning workstation. The neurosurgeon implanted electrodes, guided by a stereotactic robotic system (ROSA ONE Brain, ZIMMER BIOMET, IN, USA). After surgery, patients underwent a CT scan, which was co-registered to their pre-operative MRI to obtain precise 3D coordinates for each electrode contact. We describe the electrode localization method in detail in the **Method Details** section below. Patients were then awakened from general anesthesia and transferred to the Epilepsy Monitoring Unit (EMU) for long-term intracranial electroencephalography (iEEG) monitoring. The duration of EMU stay varied across patients, typically ranging from several days to weeks, depending on seizure frequency. During this period, the research team introduced the study to the patients and obtained written informed consent before beginning any experimental recordings. Following consent, research sessions were scheduled in coordination with the clinical team to ensure there were no disruptions to standard clinical care. Standard clinical protocols may taper or withdraw antiseizure medications to provoke seizures during iEEG monitoring. In some cases, partial sleep deprivation was employed to increase seizure likelihood.

Method details

Study design

This study is part of a broader protocol (registered clinical trial identifier: NCT05065450) investigating how amygdala stimulation affects memory formation. To assess recognition memory, subjects were asked to perform visual encoding tasks in which they viewed a series of images of everyday objects or scenes from a standard image set[69]. Scene images were taken from the Places dataset[71] and object images were taken from the Stark Lab's Mnemonic Similarity Task image-set[72]. Memory for these images was assessed approximately 24 hours later. Patients could elect to complete multiple iterations of the study protocol across different days, depending on their availability and length of stay in the EMU. Three subjects completed two visual memory encoding

tasks on two different days, one subject completed three tasks on three different days, and each of the other four subjects completed one task. Each study iteration followed a two-day structure, comprising a visual encoding task on Day 1 and a recognition memory test on Day 2. The encoding task on Day 1 was administered in two or four sessions per participant to mitigate fatigue and accommodate clinical scheduling. The encoding task comprised 180 trials in total, with each trial defined as the presentation of a single image. The task structure remained constant across iterations. Each study instance used a unique set of images. The details of the behavioral paradigm are provided below.

In less than half of the trials, one second of electrical stimulation was delivered to the amygdala following presentation of each image. The current study focuses on normative brain activity around saccade times during visual encoding. Thus, we included only trials that did not involve any brain stimulation. Although object and scene processing might engage dissociable neural mechanisms, our primary aim was to characterize neural dynamics time-locked to saccades; therefore, we pooled object and scene trials. Categories were balanced across the set, and exploratory checks did not indicate category-dependent differences in the saccade metrics. We defined valid visual encoding trials for subsequent neural analyses based on two criteria: 1. Subjects maintained their gaze on the monitor for more than half the duration of this trial, based on the eye-tracking data; 2. No brain stimulation was delivered during this trial. These decisions yielded 1130 valid visual encoding trials and 7292 valid saccades across eight patients. A detailed description of the data set, including the total number of study iterations per participant and the total number of encoding trials, is summarized in **Supplementary Table 1**.

Behavioral paradigm

Participants completed visual encoding tasks at their bedside during their stay in the EMU. Before the main task began, participants received standardized instructions and completed a brief training session to become familiar with the task structure. The images presented during training were not repeated during the main task, and data from the training session were excluded from the analysis.

After training, participants began the encoding task. A series of trial-unique color object or scene images was presented on a 27-inch monitor (TUF GAMING VG27AQL1A, ASUS, USA) mounted on a mobile cart positioned next to the patient's bed. Each image was displayed at the center of the screen for 3 seconds, followed by a 6-second inter-stimulus interval (ISI). During the image presentation, the subjects used a keyboard to indicate either "Like" or "Dislike" for object images or "Indoor" or "Outdoor" for scene images. This design was intended to maintain subjects'

engagement and attention level throughout the task. The image occupied 5.56 × 5.56 inches on the screen at a viewing distance of approximately 60 cm, corresponding to a visual angle of 13.1°. Participants were instructed to freely view each image and remember it for a later memory test. A fixation cross was presented during the ISI, but participants were not required to fixate on it. In brain stimulation trials, 1 second of electrical stimulation was delivered to the amygdala during the first second of the 6-second ISI. Only non-stimulation trials were included in the current analysis. Approximately 24 hours after completing the encoding task, participants performed a self-paced recognition memory test. The test consisted of 160-240 previously seen images and 80 novel images, randomly intermixed. Each image was displayed for a mandatory 1-second viewing period, after which participants used a keyboard to indicate whether they had seen the exact image before ("Sure No", "Maybe No", “Sure Yes”, or “Maybe Yes”).

For subsequent analysis, we assigned binary labels (Remembered and Forgotten) to encoding figures by considering the ground-truth stimulus status (previously seen vs. novel) and the participant’s response. We labeled encoding trials “Remembered” when participants correctly judged the image’s status (i.e., correctly judged if they had seen the images). To evaluate recognition independent of subjective confidence, we labelled previously seen images responded to with “Sure Yes” and “Maybe Yes” as “Remembered “and novel images responded to with “Sure No” and “Maybe No” as “Remembered”, otherwise “Forgotten”. No feedback was provided during the memory test.

Experimental setup and data acquisition

We used a desktop computer (ASUS ROG STRIX B550-E GAMING motherboard; AMD Ryzen 9 5900X 12-core processor; 32 GB DDR4 RAM; NVIDIA GeForce RTX 3070 GPU) running the BCI2000 platform to manage stimulus presentation, behavioral logging (e.g., keyboard responses), and data synchronization[27]. We recorded and synchronized photodiode signals, eye gaze coordinates, and electrophysiological signals. A 27-inch monitor (TUF GAMING VG27AQL1A, ASUS) with a resolution of 2560 × 1440 pixels and a 170 Hz refresh rate was connected to the desktop computer and mounted to a mobile cart using an adjustable monitor arm, allowing flexible positioning to accommodate each patient’s posture and bed orientation.

A screen-based eye tracker (Tobii Pro Fusion, Tobii AB, Sweden) was mounted at the bottom edge of the monitor and recorded gaze position at 120 Hz. We performed eye-tracker calibration at the start of each task using *Tobii Pro Eye Tracker Manager* software, and repeated as needed if the relative position between the participant’s eyes and the eye tracker changed.

We recorded iEEG data using a clinical SEEG system (Neurofax EEG-1200, Nihon Kohden, Irvine, CA) with a JE-120 amplifier (256 channels). Signals from depth electrode contacts were sampled at 2,000 Hz with 16-bit resolution (±3.2 mV input range, 97.65 nV/LSB). Per standard clinical practice, two subgaleal electrodes served as the reference and ground during signal acquisition. Simultaneous scalp EEG was recorded as part of the clinical montage. We specifically used frontopolar electrodes (Fp1, Fp2) to detect oculomotor artifacts.

To capture accurate timing of visual stimulus onset, a photodiode (g.tec medical engineering GmbH, Austria) was affixed to the bottom-left corner of the screen. At the onset of image presentation, a white dot was shown at the bottom-left corner of the screen, aligned with the photodiode. The white dot disappeared at the onset of the ISI. The photodiode output was routed through a multimodal trigger conditioner box (g.TRIGbox, g.tec medical engineering GmbH, Austria), and recorded simultaneously with electrophysiological and eye-tracking recordings.

Anatomical localization of the electrode

We localized electrodes based on post-operative CT scans co-registered to pre-operative T1-weighted MRI scans (0.5 mm isotropic resolution). To co-register the CT volume to the MRI volume, we first converted the MRI and CT scans from DICOM to NIfTI format using *dicm2ni*, a tool from NeuroImaging Tools and Resources Collaboratory. We rigidly transformed the CT volume to place its geometric center at the world coordinate origin. This pre-processing step ensured robust rigid-body coregistration using the *SPM12* mutual-information-based registration. For each subject, the pre-operative MRI was treated as the anatomical reference, and the CT image was coregistered to it.

We first manually localize macroelectrode contacts using Freeview, which is the visualization tool within the FreeSurfer software package. To improve precision and reproducibility, we implemented a semi-automated algorithm to align the manually identified contact positions with the most intense local signal in the CT volume, indicative of metal artifact. For each manually identified macro contact, we extracted a local CT subvolume (5×5×5 voxels, corresponding to approximately 16 mm^3) and applied a data-driven intensity thresholding procedure. Starting from an empirical threshold, estimated via kernel density estimation of voxel intensities, the algorithm progressively lowered the threshold and identified voxels that exceeded this intensity threshold until a connected component exceeding the expected physical volume of the electrode was found. Based on manufacturer specifications, the expected physical volume was a cylinder with a 1.28-mm diameter and a 1.57-mm length. We assigned the centroid of this component as the refined electrode location and validated the refined locations using Freeview.

Next, we inferred the positions of the microelectrodes from the geometry of the macro contacts. We fitted a line to each trajectory based on the macroelectrode positions using singular value decomposition. The initial estimated micro contact was located 3 mm beyond the macro contact, along the same shank axis, most distal to the entry point. The initial estimate of 3 mm was provided by the surgeon, who trimmed the micro-wires during implantation. To determine the actual microelectrode position, we localized the most intense voxel cluster in the CT volume near the initial microwire estimation, using the same intensity-guided connected-component algorithm.

To further verify the accuracy of electrode localization and to avoid any confusion in the labeling electrodes, we exported the planned electrode trajectories from the Robotic Operating Surgical Assistant (ROSA) platform, where trajectories were defined in the coordinate space of the intraoperative imaging system. To transfer these trajectories into the same anatomical reference space as the localized electrode contacts, we performed rigid-body image coregistration between the ROSA display image and the pre-operative T1-weighted MRI. The transformation was then applied to the extracted ROSA trajectories. As a result, both the planned lead trajectories and the electrode localizations were in the same right-anterior-superior (RAS) coordinate space defined by the pre-operative MRI.

To determine the brain regions associated with each electrode, we performed anatomical brain segmentation using FreeSurfer (v7.4.1), which also creates a cortical and subcortical functional parcellation based on the Desikan-Killiany atlas[73]. We assigned functional-anatomical labels to each electrode contact using a majority-vote volumetric method, in which each electrode was assigned to the brain structure encompassing the majority of segmented voxels within a 10 mm Euclidean radius from the contact center. We chose a 10 mm Euclidean radius to approximate the spatial reach of local field potential recordings. To assess the consistency of the functional–anatomical labeling of electrode contacts, we performed two complementary analyses. First, we used a surface-based inclusion method, in which electrodes were labeled according to whether their coordinates were enclosed by the triangulated surface mesh of a segmented structure. Second, we implemented a probabilistic labeling approach, in which each structure was assigned a probability proportional to the number of its voxels within a 10 mm sphere centered on the electrode.

For group-level analysis and visualization, we mapped individual electrode locations to a common anatomical space defined by the native MRI of a reference subject. To achieve this, we used the ANTs (Advanced Normalization Tools) image registration framework to coregister each subject's preoperative T1-weighted MRI to the reference MRI. We applied only the affine

component of the transformation to the electrode coordinates to preserve their linear relationships. The affine matrices were estimated within the ANTs' non-linear optimization pipeline to account for anatomical variability.

To characterize regional differences in electrode sampling, we calculated the weighted count of electrode contacts per brain region (**Figure 1D**). In other words, when electrode contacts (~2 mm^3 volume) overlapped multiple brain regions, their contributions were proportionally allocated among these regions. We further quantified sampling density per region by dividing the weighted contact count within each brain region by the volume of that region (**Figure 1 – Figure Supplement 2**).

Eyeball-to-Electrode Distance calculation

To determine whether the observed SREP could be attributed to oculomotor signals, we performed regression analysis between the eyeball-to-electrode distance and SREP characteristics such as peak amplitude. We used the Euclidean distance from each electrode contact to the nearest eye-globe center to approximate the distance between electrode contacts and the myogenic dipole source generated by extraocular muscle activation. We identified the center of each eyeball for each subject based on their pre-operative T1-weighted MRI scans and then computed the 3-dimensional (3D) Euclidean distance from the left and right eyeballs' centers to each electrode contact's coordinates. We used the minimum of the left and right eyeball distances, representing the distance from an electrode to the closest eyeball, as the eyeball-to-electrode distance for subsequent analyses.

Assessing memory outcome

We defined two memory outcome measures in our study: 1) Recall rate as the percentage of remembered visual encoding trials over the tested visual encoding trials; and 2) Overall correct recognition rate as the sum of true positives (old stimuli correctly recalled) and true negatives (new stimuli correctly rejected) divided by the total number of test trials. To assess whether recognition memory performance exceeded chance, our primary analysis considered the expected accuracy under unbiased guessing, in which subjects respond "old" or "new" with equal probability on each trial. Under this assumption, the expected hit rate and correct rejection rate are both 50%, yielding an overall chance-level accuracy of 50%.

In cases where the recognition test included an unequal number of previously presented and novel images, we additionally evaluated two response-bias extreme strategies to characterize the range of overall recognition accuracies driven by response bias. In one extreme, a subject

could respond “old” on every test trial. Under this strategy, all previously presented images would be counted as correctly recognized, whereas all novel images would be incorrectly classified as old. In our study, 5 subjects completed task iterations that included 160 previously presented images and 80 novel images. This strategy would yield a correct recognition rate of 100% for previously presented images, a correct recognition rate of 0% for novel images, and an overall correct recognition rate of 66.7%. Based on post hoc inspection of behavioral performance (**Supplementary Table 3**), one subject (Subject ID 1) exhibited a response pattern consistent with this extreme strategy during one task iteration (Task ID 2) out of the two completed tasks.

In the opposite extreme, a subject could respond “new” on every test trial. Under this strategy, all novel images would be correctly rejected, whereas all previously presented images would be incorrectly classified as new. For the task structure including 160 previously presented images and 80 novel images, this strategy would yield a correct recognition rate of 0% for previously presented images, a correct recognition rate of 100% for novel images, and an overall correct recognition rate of 33.3%. The post hoc inspection of behavioral performance indicated that no subjects exhibited response patterns consistent with this strategy.

Given that all subjects verbally reported completing the task as instructed, and that eye-tracking showed normative visual scans during the encoding phrase of the task, we did not exclude data based on the post hoc inspection of behavioral performance.

Intracranial EEG preprocessing

To ensure the analysis focused on physiologically meaningful, non-pathological signals, we systematically identified and excluded electrodes exhibiting epileptiform discharges or artifactual activity (e.g., due to poor contact). To identify electrodes with poor contact, we computed the root-mean-square (RMS) amplitude of the 60 Hz line-noise component using a narrowband infinite impulse response (IIR) filter using *iirpeak* in MATLAB with a peak frequency of 60 Hz and a bandwidth of 0.1 Hz as inputs. Electrode contacts with 60 Hz RMS amplitude deviating more than two standard deviations (SDs) from the median were flagged and excluded. To detect potential shorted (i.e., electrically bridged) contacts, we computed pairwise Pearson correlation coefficients between all contacts within each electrode trajectory after re-referencing. For re-referencing, we applied common average referencing for each electrode trajectory after excluding electrode contacts with excessive 60 Hz line noise. We identified contacts exhibiting excessively high correlation with non-adjacent neighbors ($R^2 > 0.999$) as potentially electrically shorted and excluded them from further analysis. We did not find any shorted contacts.

To identify electrodes with epileptiform activity (e.g., sharps and spikes), we identified time periods in the signal that exhibited exceptionally sharp transients[74]. For this purpose, we first extracted high-frequency iEEG signals (>250 Hz) using a 4th-order Butterworth filter (*butter* function in MATLAB). We computed the analytic envelope of the high-pass filtered signal using the Hilbert transform (*hilbert* function in MATLAB) and identified time points at which the envelope exceeded 5 SDs above the mean. Additionally, we identified time points at which both the raw signal amplitude and its temporal gradient exceeded 5 SDs above their means. We marked the identified time points as epileptic and calculated the proportion of epileptic time per electrode. We excluded electrodes exhibiting epileptiform activity for more than 1% of the recording duration. We applied the procedures for identifying line noise and shunted contacts to microwire recordings. We did not apply the epileptiform activity exclusion criterion to microwires, as they recorded both neuronal spiking activity and LFPs. **Supplementary Table 3** summarizes per-subject counts of retained electrodes for subsequent signal processing.

To enhance spatial specificity and remove common artifactual noises, we re-referenced intracranial signals using a small Laplacian re-referencing, separately for macro electrode and micro wires. We calculated inter-contact Euclidean distances derived from the three-dimensional electrode coordinates. For each contact, neighboring electrodes were identified as those located within a predefined spatial threshold of 6 mm. We then epoched the resulting Laplacian re-referenced signals relative to stimulus onset for subsequent SREP analyses. To ensure the robustness of downstream analyses to the referencing scheme, we tracked the number of neighboring electrodes. For some electrodes located at the ends of a shank, where only a single adjacent contact was available, the small Laplacian re-referencing became bipolar referencing.

Saccade detection and characterization

The recorded eye-tracking data included three-dimensional eye position and two-dimensional gaze direction, expressed relative to the top-left corner of the display monitor. Gaze coordinates were defined on the screen plane (Z = 0), whereas the Z-coordinate of the eye position represented the eye's distance from the display along the axis orthogonal to the screen. To ensure that saccade detection was based on eye gaze sample where no eye blinks or off-screen gaze occurred, we preprocessed the eye-tracking data separately for each eye and marked eye tracking samples as invalid if they met two criteria: (1) the eye tracker reported loss of tracking (e.g., during blinks or partial eyelid closures), or (2) the gaze coordinates were outside the physical screen bounds. To account for signal artifacts at the edges of blinks or tracking dropouts, we extended each invalid segment by ±30 ms on both sides.

To account for the possibility that the eye tracker only captured one of the two eyes, we computed the proportion of valid samples for each eye, and selected the eye with the higher proportion of valid data for further analysis. We time-locked the gaze data to the image presentation. We defined each trial as the interval from 2 s before the onset of the fixation cross presentation to 2 s after image presentation offset (**Figure 1b**). To ensure that our analyses reflected periods during which subjects were encoding visual information, we excluded individual trials with more than 50% invalid eye-tracking data.

To identify saccade onsets, we segmented the continuous gaze traces into periods of fixation and saccades using the *ClusterFix* algorithm[75]. In brief, the algorithm identified eye movement events by clustering consecutive gaze coordinate samples based on distance, velocity, acceleration, and angular velocity to classify them as fixations or saccades. We linearly interpolated invalid samples in gaze data to maintain the temporal continuity required by the clustering algorithm. After clustering, we verified that both onset and offset for each identified saccade and fixation occurred during valid (e.g., noninterpolated) samples. Saccadic or fixation events overlapping interpolated segments were flagged as invalid and excluded from downstream analyses. This conservative approach ensured that only fixations and saccades derived from true gaze samples were included in the analysis. We validated that the velocity and duration of detected saccades were within the expected range of human eye-movement parameters (**Figure 1 – Figure Supplement 1**).

We calculated saccade eccentricity, saccade direction, and saccade and fixation duration based on the onset and offset time of the detected saccade or fixation. We transformed gaze coordinates into a vector representing gaze coordinates relative to eye location in the right-anterior-superior (RAS) coordinate system, and normalized it to unit length. Based on the normalized vector $\overrightarrow{(gaze_x, gaze_y, gaze_z)}$, we calculated the azimuth and elevation angle ($\theta_{azimuth}$ and $\theta_{elevation}$) in polar coordinates. In this study, we defined horizontal eye movements as saccades with azimuth angles within $\pm 20°$ of the horizontal axis, and vertical eye movements as saccades with elevation angles within $\pm 20°$ of the vertical axis.

$$\theta_{azimuth} = tan^{-1}\left(\frac{gaze_y}{gaze_x}\right)$$

$$\theta_{elevation} = tan^{-1}\left(\frac{gaze_z}{\sqrt{gaze_x^2 + gaze_y^2}}\right)$$

We calculated the angular change $\Delta\theta_{azimuth}$ and $\Delta\theta_{elevation}$ based on $\theta_{azimuth}$ and $\theta_{elevation}$ at saccade onsets and offsets. We defined the saccade eccentricity as $\sqrt{\Delta\theta_{azimuth} + \Delta\theta_{elevation}}$. We defined saccade direction θ_{dir} as the orientation of the 2D angular displacement vector connecting gaze positions before and after each saccade. In this convention, 0 rad (e.g., 0°) corresponds to rightward saccades, $\frac{\pi}{2}\,rad$ (e.g., 90°) to upward saccades, $\pi\,rad$ (e.g., 180°) to leftward saccades, and $\frac{3\pi}{2}\,rad$ (e.g., 270°) to downward saccades.

$$\theta_{dir} = tan^{-1}(\frac{\Delta\theta_{elevation}}{\Delta\theta_{azimuth}})$$

To study whether SREPs encode the direction of the next saccades, we identified consecutive saccades that occurred with both spatial and temporal continuity constraints. Specifically, we required the spatial distance between the end of the current saccade and the start of the subsequent saccade to be less than 20% of the display dimension, and the inter-saccadic interval to be shorter than 550 ms.

Identification of saccade-related evoked potentials (SREPs)

To identify SREPs, we analyzed re-referenced LFP signals time-locked to saccades. The dataset was organized hierarchically: each subject completed one or more encoding tasks, each task consisted of multiple recording sessions, and each session contained LFP signals from multiple electrode contacts. Within each session, there were multiple trials (e.g., image presentation), during which one or more saccades occurred. For each encoding task completed by a subject, we segmented the re-referenced signals into epochs relative to saccade onsets and combined all epochs across trials and sessions within that task. This study focused on saccades occurring during the encoding of the presented image. To isolate SREPs from stimulus-onset responses, we excluded saccades occurring 200 ms before or after the image onset. For control analyses, we separately analyzed saccades made during fixation-cross presentation, when the screen background was uniformly black with a central white fixation cross occupying approximately 2% of the screen's horizontal dimension. The fixation-cross presentation period provided a baseline condition for evaluating whether peri-saccadic EPs reflected visual transients. For each epoch, we defined the pre-saccadic interval from -200 to -10 ms relative to the saccade onset as the baseline period. We normalized each epoch by z-scoring its LFP signal based on the baseline mean and SD. To obtain the mean SREP waveform for each electrode contact, we averaged the normalized LFP signals across all saccades, trials, and sessions.

To determine whether SREPs were consistent across epochs, we calculated the pairwise Pearson correlation coefficients among normalized epochs within the peri-saccadic window (-10 to +40 ms relative to saccade onset) and, for comparison, within the baseline window[30]. These windows were defined to capture the immediate neural dynamic following a saccade while avoiding temporal overlap between EPs arising from consecutive saccades. To ensure robustness of subsequent analyses, we systematically varied the baseline window length and confirmed consistent results (**Figure 2—Figure Supplement 4**). Unless otherwise noted, the results presented in this study were derived using the −200 to −10 ms baseline.

The distribution of correlation coefficients during the peri-saccadic period exhibited a bimodal pattern, suggesting SREPs of two polarities (**Figure 2d**). To statistically evaluate this observation, we quantified the extent to which the peri-saccadic correlation distribution deviated from the unimodal baseline distribution. We quantified bimodality based on the separation between the inter-trial correlation distributions during the peri-saccadic and baseline periods. We computed the intersection point of their cumulative distributions and measured the absolute difference in area under the curve (AUC) between them as their separation effect size (**Figure 2 – Figure Supplement 2**). This separation effect size reflected the extent to which inter-trial correlations during the peri-saccadic period were bimodal, with larger values indicating stronger bimodality. To assess statistical significance, we applied Kolmogorov–Smirnov tests to determine the separation effect size threshold corresponding to the significance level adjusted for multiple comparisons.

This analysis confirmed the presence of bimodal SREPs. To identify the two types of SREPs, we applied hierarchical clustering to the inter-trial correlation matrix using the MATLAB *linkage* and *cluster* functions with *maxclust* input set to 2. Each element of this matrix represented the correlation coefficient between a pair of epochs. In brief, hierarchical clustering groups epochs based on their pairwise correlation, and then iteratively merges those with the most similar waveforms to form a dendrogram that captures the hierarchical relationship among epochs. To ensure the robustness of the hierarchical clustering algorithm, we required a minimum cluster size of 25% of the total number of epochs. Failure to meet this criterion could occur when the inter-trial correlation structure was weakly bimodal. In this study, only three electrode contacts had peri-saccadic correlation matrices that failed to meet this criterion. For these electrode contacts, we implemented an adaptive re-clustering procedure that iteratively removed epochs with globally weak correlations, defined as the lowest mean absolute correlation across epochs, and repeated the clustering until both clusters satisfied the size criterion.

After identifying SREPs of two polarities, we quantified the separability between peri-saccadic and baseline correlation distributions for each cluster. To do so, we computed the receiver operating characteristic (ROC) curve, which characterizes how well the two distributions can be distinguished. The ROC curve plots the true positive rate (TPR), defined as the fraction of peri-saccadic correlations exceeding a given threshold, against the false positive rate (FPR), defined as the fraction of baseline correlations exceeding the same threshold. Thresholds were sampled uniformly between −1 and 1. The area under the ROC curve (AUC) measures the separability. Larger AUC values indicate greater divergence of peri-saccadic correlation structure from baseline, reflecting more consistent SREP waveforms.

As a control, we repeated the clustering and separability quantification procedures described above after permutating the peri-saccadic and baseline correlation matrices. We applied the identical adaptive hierarchical clustering procedure on the baseline correlation matrix. We then recomputed the ROC curve following the same procedure, but with the roles of peri-saccadic and baseline correlations reversed. In other words, the TPR now represented the fraction of baseline correlations exceeding a given threshold, and the FPR represented the fraction of peri-saccadic correlations exceeding the same threshold. We then compared the observed and control AUC values to identify electrode contacts with consistent SREPs, using AUC difference as a measure of consistency. This control analysis accounts for potential bias introduced by the clustering algorithm and enables estimation of separability specifically attributed to peri-saccadic LFP waveform similarity.

Quantification of SREP consistency and regional SREP prevalence

To identify the brain region where LFP waveforms in the peri-saccadic window were most consistent, we computed the SREP prevalence for each brain structure. The SREP prevalence was defined as the proportion of electrode contacts whose peri-saccadic AUC exceeded the mean + 2 SDs of their respective baseline AUC values (**Figure 2G**). The use of proportion rather than the number of electrode contacts controls for varying sampling density across the cerebrum. We calculated the SREP prevalence for the following structures: White Matter (Left, Right), Hippocampus (Left, Right), Amygdala (Left, Right), Basal Ganglia, Thalamus, Orbitofrontal (Left, Right), Inferior Frontal (Left, Right), Middle Frontal (Left, Right), Superior Frontal (Left, Right), Anterior Cingulate, Posterior Cingulate, Motor (Left, Right), Anterior Temporal (Left, Right), Middle Temporal (Left, Right), Superior Temporal (Left, Right), Inferior Temporal (Left, Right), Medial Temporal (Left, Right), Fusiform (Left, Right), Parietal (Left, Right), Occipital (Left, Right), and Insula (Left, Right).

To robustly quantify the fraction of electrode contacts within a region that exhibit consistent saccade-related activity, we systematically varied the responsiveness threshold from mean + 1 SD to mean + 4 SD of baseline AUC (**Figure 2—Figure Supplement 1**). For each threshold, we calculated the proportion of electrode contacts exceeding the threshold. This yielded a curve where the y-axis represented the SREP prevalence defined before, and the x-axis represented the responsiveness threshold. As an integrated measure of regional LFP waveform consistency following saccades, we computed the area under this curve (AUC) across all thresholds. To control for the number of sampling electrodes across brain structures, we resampled electrodes with replacement to equalize sample sizes across regions, then repeated the AUC calculation. We computed the Pearson correlation coefficient between AUC with and without resampling, and demonstrated the stability of the AUC value with respect toregional sampling density.

To determine the spatial distribution of the degree of LFP waveforms consistency following saccades, we computed the difference in AUC between peri-saccadic and baseline inter-trial correlation distributions (**Figure 2–Figure Supplement 2c**). As a complementary measure, we defined the degree of consistency as the average AUC of the probability density over inter-trial correlation following saccades, computed separately for the two clusters and then averaged (**Figure 2–Figure Supplement 2D**).

Characterization of SREP waveforms

To test whether the observed SREPs represented oculomuscular signals or neural mechanisms of visual encoding, we quantified their waveform characteristics, including latency, peak amplitude, peak time, trough time, and peak-to-trough amplitude. We used these SREP characteristics in subsequent analysis of the correlation between SREP peak amplitude and saccade eccentricity, and in machine learning models to map their relationship with successful visual encoding. We calculated SREP characteristics at both averaged and single-trial levels. Here, averaged SREPs refer to SREPs across all saccades, trials, and sessions; and single-trial SREPs refers to the LFP trace following a single saccade.

For each electrode contact and cluster identified by the hierarchical clustering procedure described above, we computed the average SREP and quantified its characteristics. We normalized SREP amplitude using a z-score based on the baseline. We used MATLAB's *findchangepts* function on the first derivative of the averaged SREPs to identify two change points. This function partitions the time series into segments whose means differ maximally, thus detecting points of abrupt change in slope. We defined the first change point SREP latency, corresponding to the earliest statistical deviation from baseline (**Figure 3A**). Within a ±10 ms

window around the second change point, we identified the peak time as the point of maximal normalized amplitude for positive-polarity clusters, or minimal amplitude for negative-polarity clusters. We extracted the peak amplitude and peak-to-trough amplitude based on the averaged SREP. We defined trough time as the time point within a 10-ms window around latency at which the normalized amplitude was minimal for positive clusters or maximal for negative clusters.

For each single-trial SREP, we centered the ±10 ms latency search window on the latency of the averaged SREP from its assigned cluster. We applied MATLAB's *findchangepts* function to the first derivative of the single-trial LFP to detect one change point. We defined this inflection point as the single-trial SREP latency. Similarly, we defined peak-amplitude search windows centered on the averaged SREP peak time from the associated cluster. We identified single-trial SREP peak amplitude as the maximum (for positive clusters) or minimum (for negative clusters) amplitude within this window. We identified the single-trial SREP trough between latency and the peak time, defined as the minimal (for positive clusters) or maximal (for negative clusters) amplitude in this interval. We flagged a trial as having an invalid peak–trough identification if the detected trough amplitude exceeded the detected peak amplitude for positive clusters or the detected peak amplitude exceeded the detected trough amplitude for negative clusters. This happened for 1% of the electrode contacts. To verify that the hierarchical clustering procedure reliably separated SREP waveforms of two polarities, we quantified the similarity between each single-trial SREP and its cluster-level averaged waveform using Spearman's correlation coefficient. For subsequent analysis, unless specified otherwise, we included single-trial SREPs whose waveforms were similar to the averaged SREP, defined as those with a Pearson correlation coefficient above the median.

Assessing the relationship between SREP characteristics and saccadic properties

To test whether the observed SREPs reflected oculomuscular activity, we evaluated three predictions derived from an ocular artifact model. The first prediction is that cluster-level averaged SREP amplitude, including peak and peak-to-trough amplitude, should vary systematically with eyeball-to-electrode distance. To test this prediction, we performed linear regression on cluster-level averaged SREP amplitudes with eyeball-to-electrode distance as the independent variable, using the Python library *statsmodels* (**Figure 3D**). We computed the explained variance, that is, the coefficient of determination (R^2). As a control, we extracted electrooculogram (EOG) signals derived from the differential potential between fronto-polar scalp EEG electrodes (Fp1 and Fp2), and applied the same epoching, clustering, and waveform characterization procedures to EOG signals as for intracranial EPs. We computed R^2 using the same method. We then compared R^2

between intracranial electrode contacts and EOG signals using statistical tests described in the **Quantification and Statistical Analysis** section.

The second prediction of the ocular artifact model is that single-trial SREP amplitude should covary with saccade kinematics such as saccade eccentricity. To test this, we performed linear regressions between single-trial SREP amplitude, including peak amplitude and peak-to-trough amplitude, and saccade eccentricity. Data was omitted when we failed to detect trough. We conducted regression separately for intracranial LFPs and EOG signals, treating eccentricity as the independent variable. As complementary analyses, we calculated the Pearson's correlation coefficient between single-trial SREP amplitude and saccade duration.

The third prediction of the ocular artifact model is that SREP polarity reflects the directional movement of extraocular muscles; therefore, it should be associated with saccade direction. We examined the relationship between saccade direction and the polarity of EP at saccade times derived from EOGs and the relationship between saccade direction and the polarity of SREPs from intracranial signals. We first quantified directional clustering of saccades using the Rayleigh statistic. For each electrode contact, we extracted the saccade direction associated with each polarity and measured the degree of unimodal bias of the circular distribution of directions using Rayleigh statistics (Monopolar condition). We compared them against Rayleigh statistics computed from the same number of saccades pooled across both polarities (Combined condition).

To avoid the potential confounds of sample size on the calculation of Rayleigh statistics, we resampled the same number of saccade directions for positive, negative, and combined polarities. To avoid unstable estimates due to sparse saccades associated with a single polarity, we imposed a minimum-saccade criterion based on a global quantile threshold ($q = 0.2$). This yields sample sizes for positive and negative EPs at saccade times from EOG (Positive $n = 15$, Negative $n = 18$, Combined $n = 21$). We tested for differences in the circular distributions of saccade directions between opposing polarities for SREPs derived from intracranial recordings and EOG-derived EPs at saccade times (see **Quantification and Statistical Analysis** section). We performed the analysis in two ways: (1) treating saccades during image presentation and fixation-cross presentation as separate samples, and (2) pooling saccades across both task epochs. The results were consistent across both analyses.

Oscillation detection and quantification

To test if pre-saccadic oscillatory activity influenced SREP polarity, we first identified the dominant oscillation frequency for each electrode contact. We computed the power spectral density (PSD)

using Welch's method on continuous re-referenced LFPs. Specifically, we used MATLAB's *pwelch* function using 1-s Hanning windows (2,048 samples) with 50% overlap and a 2-s discrete Fourier transform length (4096 samples). To separate periodic oscillatory components from the aperiodic activity, we fitted a 1/f model to the PSD in log–log space using MATLAB's *polyfit* function. To minimize the influence of 60 Hz line noise, we fitted a linear model to the log-transformed PSD curve within the frequency range of 1-58 Hz. We calculated PSD residues as the pointwise difference between the original PSD curve and the fitted line. To ensure that oscillatory peaks did not bias the aperiodic fit, we excluded frequencies whose residuals were positive and exceeded the median residual, then recalculated the 1/f fit. We defined the dominant oscillation frequency for each contact as the frequency at which the residual PSD curve reached its maximum. To quantify oscillation strength for each electrode contact, we computed the residual PSD value at the dominant oscillation frequency.

To quantify the instantaneous phase and power of the oscillation at the dominant frequency, we applied the Hilbert transform to narrowband-filtered signal segments surrounding each saccade. To ensure that estimates of pre-saccadic oscillatory activity were not affected by the presence of SREP, we segmented LFPs from -3 s before saccade onset up to SREP latency. For each electrode contact and each encoding task, we estimated the instantaneous oscillation phase and power separately for two clusters of SREPs. To minimize edge artifacts potentially introduced by filtered signals and the Hilbert transform, we symmetrically padded both ends of each segment with 500 ms of data before filtering. We applied a second-order Butterworth band-pass filter centered on the identified dominant oscillation frequency with a half-bandwidth of 3 Hz using MATLAB's butter function. To implement zero-phase digital filtering, we used MATLAB's *filtfilt* function to apply the filter in both the forward and reverse directions. We then used MATLAB's Hilbert function to obtain the analytic signal. To ensure unbiased estimates, we only derived the instantaneous power and phase from the portions of the analytic signal corresponding to the unpadded original LFPs. Because the oscillation cycle (OC) duration varied with the dominant oscillation frequency, we defined pre-saccadic time points relative to each electrode contact's OC. Our time points of interest included 0.5, 1, 1.5, 2, and 3 OC before the latency.

$$OC = \frac{1}{dominant\ oscillation\ frequency}$$

To study the interplay between SREP and oscillatory activities, we estimated instantaneous oscillation power and phase after SREP latency. For this purpose, we segmented LFPs from -300 to 300 ms relative to the saccade onset and repeated the padding, filtering, and

Hilbert-transform procedures. To enable subsequent cross-session and cross-subject comparisons, we z-scored instantaneous power relative to a baseline window, defined as -200 ms to -90 ms relative to saccade onset.

Assessing the relationship between pre-saccadic oscillation phase and SREP polarity

To test whether the oscillatory phase preceding saccades differed between SREP polarities, we first wrapped phase values from [–π, π] to [–2π, 2π] to preserve periodicity and continuity. We then estimated the probability density functions separately for each polarity. To quantify the separation in phase between polarities, we calculated the absolute difference in area under the probability density curve. To determine statistical significance, we generated null distributions by randomly permuting SREP polarity labels (50 iterations per electrode contact) and recalculated the separation metric for each permutation. Observed and null values were compared using two-sided Wilcoxon signed-rank tests (n = 1,970 electrode contact pairs per condition). Effect sizes were quantified using the rank-biserial correlation, which increased progressively from 0.204 to 1.000 across the five pre-saccadic time points, indicating a gradual divergence of oscillatory phase between SREP polarities as saccades approached.

To evaluate whether the pre-saccadic oscillation phase influenced the polarity of SREPs, we quantified phase separation between positive and negative SREP clusters at both the single-contact and contact-averaged levels. Positive and negative SREP clusters refer to sets of SREPs with positive and negative waveform polarities. Analysis in this section used the instantaneous phase derived from LFPs truncated before the SREP latency (see **Oscillation detection and quantification**). Because the phase is circular, direct density estimation on [–π, π] can introduce boundary artifacts, as probability mass at the endpoints (–π and +π) is artificially split. To avoid this, we extended the phase range by concatenating copies of the phase values shifted by ±2π, preserving continuity across the circular boundary ±π. At the single-contact level, we computed phase histograms for positive and negative polarities using 72 equally spaced bins spanning [–2π, 2π] using the *histogram* function from the *Numpy* Python package. To obtain a continuous phase probability density function (PDF), we applied a Gaussian kernel filter (σ = 1 radian) using the *gaussian_filter1d* function from the SciPy Python package. We normalized each estimated phase PDF such that its integral over the canonical [–π, π] range equaled 1, using the *Simpson* function from the Scipy Python package. We calculated phase separation as the area under the absolute difference between the two normalized PDFs using the same *Simpson* function. At the

single-contact level, we computed phase separation for each electrode contact across the five pre-saccadic time points of interest.

To determine statistical significance, we generated null distributions by randomly permuting SREP polarity labels and recalculated the phase-separation metric for each permutation. We conducted 50 permutations per electrode contact. We then compared observed and null separation values at the five pre-saccadic time points of interest, as detailed in the **Quantification and Statistical Analysis** section.

Analysis of oscillatory power and phase synchronization associated with SREPs

To investigate how SREPs interacted with ongoing neural oscillations, we analyzed temporal changes in oscillation power and phase synchronization around saccade times. To quantify inter-trial phase alignment, we computed the inter-trial phase coherence (ITPC) for each polarity and each electrode contact, based on the instantaneous phase of the narrowband analytic signal filtered at each contact's dominant oscillation frequency, which is detailed in the Oscillation detection and quantification section. ITPC is defined as:

$$\mathrm{ITPC}(t,f) = \left| \frac{1}{K} \sum_{\mathrm{k}=1}^{K} e^{i\phi_k(t,f)} \right|,$$

where $\boldsymbol{\phi_k(t,f)}$ denotes the instantaneous phase of saccade $\mathbf{k}$ at time $\boldsymbol{t}$, and $\boldsymbol{f}$ denotes the dominant oscillation frequency. For each electrode contact, we quantified ITPC at time points of interest, including 0.5, 1, 1.5, 2, and 3 OCs before the SREP latency, at latency, peak time, and 0.5 OCs after peak time. To understand whether phase synchronization was accompanied by increased oscillation power, we computed Pearson's correlation between changes in ITPC and changes in instantaneous power relative to 2 OCs before SREP latency at time points of interest, using the *pearsonr* function from the *Scipy* Python library for calculating.

Quantifying intra- vs inter-contact variability of SREP characteristics

We observe trial-by-trial variations in recognition memory. Thus, if SREPs contribute to encoding, within-electrode-contact SREP characteristics should vary across saccades and trials. if SREPs reflect a spatially organized neural process, we also expect across-electrode contact variability in SREP characteristics such as peak amplitude and onset latency. It is our intention to quantify intra-contact versus inter-contact (spatial) variability in SREP latency and peak amplitude to determine whether SREPs were anatomically organized. To ensuring comparability, we estimated intra-contact and inter-contact variability based on matched sample sizes.

To compute intra-contact variability, we first resampled SREP characteristics, including latency and peak amplitude, within each electrode contact to the median saccade count (e.g., 144) across contacts to minimize the effect of sample size on the estimation of variability, thereby ensuring comparability across contacts. We then computed the standard deviation (SD) of SREP latency and peak amplitude for each contact. To estimate inter-contact (e.g., spatial) variability with matched sampling, we resampled electrode contacts to equalize the sample number used for intra-contact SD estimation. We calculated the SD of latency and peak amplitude from the averaged SREP waveform. We repeated this procedure 100 times and averaged the SD of latency for statistical comparison.

To assess whether polarities affected the SREP latency or peak amplitude distribution, at each contact, we computed SREP latency from the trial-averaged waveform separately for each polarity and assessed Pearson correlation between the paired latencies or peak amplitudes across contacts. To further validate that the SREP characteristics differences, including latency and peak amplitude differences, between contacts capture the spatial organization of saccadic modulation, we related the between-contact SREP characteristic differences derived from trial-averaged SREPs to the effect size of latency differences estimated from single-trial SREPs. Because the number of contact pairs is large, we randomly sampled 2,000 contact pairs per polarity and computed the Pearson correlation.

Spatial visualization of SREP characteristics

To illustrate the spatial organization of SREPs at both the brain-region and electrode-contact levels, we developed a surface-based visualization framework that maps outcome values onto a brain model, allowing us to convey findings related to the spatial organization intuitively. Using this framework, we visualized SREP characteristics, such as latency and amplitude (**Figure 5B–C**) and other outcomes, such as proportion of electrode contact showing early SREP (**Figure 5D**) and feature importance in predicting recognition memory (detailed in **Model Evaluation**). For region-level mapping, we assigned each electrode contact an anatomical label using the majority-vote volumetric approach, detailed in the **Anatomical localization of the electrode** section. We computed the average outcome value, such as the mean SREP latency, across electrode contacts within each region. For each brain region, we reconstructed and rendered three-dimensional surfaces from a reference MRI volume using the PyVista Python package. We mapped regional average values onto the corresponding cortical or subcortical surface meshes and color-coded the surfaces using a sequential colormap (e.g., pale to dark green).

To provide higher-resolution spatial information, we constructed 2D glass-brain heatmaps projected from the 3D brain model. Briefly, we projected electrode coordinates in the common anatomical space onto a 2D plane orthogonal to a vector representing the viewing angle. Given the electrode size and approximately 1-cm reach of signals. We discretized this 2D space into grid elements, each as a 5 mm × 5 mm square, unless specified otherwise. For each grid element, we computed the local mean outcome values, for example, mean EP latency, across nearby contacts. For each grid cell, we defined nearby contacts as those located within a 10-mm radius. We color-coded each grid element based on the local mean outcome values using a white-to-red colormap. Grid elements without nearby electrode contacts were rendered transparent to truly represent electrode coverage.

Spatial modeling of SREP latency using Gaussian Mixture Models (GMMs)

To examine whether early SREPs were spatially localized, we stratified electrode contacts into percentile bins based on their average SREP latency (e.g., 0–15th, 30–45th, 60–75th percentiles). For each latency percentile bin, we applied 3D GMMs to the spatial coordinates of electrode contacts in the common anatomical space. We implemented GMMs using the *GaussianMixture* function from the *sklearn* Python package, with the number of components (e.g., *n_component*) set to 2 to identify bilateral spatial clusters corresponding to the two hemispheres. We extracted the centroids of identified clusters to determine their hemispheric localization. We quantified the spatial spread as the Euclidean norm of standard deviations along X, Y, and Z axes, estimated by the GMMs. To assess if there is progressive spatial expansion of SREPs across regions, we calculated spatial spread across latency percentile bins and assessed monotonic trends using Spearman's rank correlation coefficient. A significant positive trend would suggest early focal localization of SREP and later widespread involvement.

To quantify the temporal involvement across anatomical regions, we quantified the proportion of electrodes within each region exhibiting SREPs in each latency percentile bin, which was defined as the number of electrode contacts with SREPs in a given latency range divided by the total number of sampled electrodes in that region. To identify regions showing systematic early or late SREPs, we assessed monotonic change using Spearman's rank correlation coefficient. To examine whether regions showing strong SREPs also exhibited spatial clustering, we repeated the GMM analysis and proportion–percentile correlation analyses described above for SREP peak amplitude.

Saccade-Related Neural Dynamics (SRND) model

SREPs and the preceding oscillatory activity jointly reflect transient neural dynamics that may contribute to visual encoding. The finding that the pre-saccadic oscillation phase influenced SREP polarity, combined with the finding that SREPs were accompanied by increase in oscillation power and inter-trial phase coherence, motivated us to develop a model, the SRND model, to parameterize and reconstruct the neural dynamics around saccade onsets (**Figure 6A**). For each electrode contact and saccade, we reconstructed the saccade-related neural dynamic $SRND(t)$ as a composite of (1) a sigmoidal SREP waveform and (2) its preceding oscillatory activity. We modeled SREP waveforms $EP(t)$ as sigmoidal rise-and-fall functions parameterized by three temporal features: latency $t_{latency}$, peak time t_{peak}, and peak-to-trough amplitude Amp. As SREPs exhibited opposing polarities, we used signed peak-to-trough amplitude to describe their magnitude, capturing both polarity and peak amplitude.

$$EP(t) = OSC\left(t_{latency}\right) + Amp \cdot S\left(t; t_{latency}; t_{peak}\right), \quad t \leq t_{latency}$$

$$S(t) = \begin{cases} \dfrac{1}{1 + exp(-12(\dfrac{t - t_{latency}}{t_{peak} - t_{latency}} - \dfrac{1}{2}))}, & t_{latency} \leq t \leq t_{peak} \\ \dfrac{1}{1 + exp(-12(\dfrac{t - t_{peak}}{t_{end} - t_{peak}} - \dfrac{1}{2}))}, & t_{peak} \leq t \end{cases}$$

We modeled the preceding oscillatory activity $Osc(t)$ as a sine wave parameterized by instantaneous power and phase ϕ of oscillation at the dominant frequency at half OCs before SREP latency.

$$Osc(t) = \sqrt{power}(2\pi f t + \phi)$$

The combined LFP trace $SRND(t)$ is the linear combination of $EP(t)$ and $Osc(t)$. We ensured continuity at SREP latency by adding $Osc\left(t_{latency}\right)$ to $EP(t)$. To truly represent the transient saccadic modulation, we confined the support for time t as [-50, 100] ms relative to saccade onset.

Assessing the relationship between eye movement parameters and encoding performance

To assess whether eye movement parameters were related to visual encoding performance assessed by recognition accuracy on the following day, we compared saccade eccentricity, duration, and direction between remembered and forgotten trials. We quantified the saccade

direction dissimilarity as the absolute area between circular kernel density estimates of saccade direction for the two conditions. To evaluate statistical significance, we compared the observed direction dissimilarity with a null distribution generated from 2,000 random permutations of trial labels (remembered vs. forgotten).

Random forest classifier

To test our primary hypothesis that the SRND model predicts visual encoding performance, we trained random forest (RF) classifiers to learn the mapping between SRND parameters and recognition memory outcomes (remembered vs. forgotten), as illustrated in **Figure 6C**. In brief, an RF consists of an ensemble of decision trees, where each tree predicts the class of an observation based on feature thresholds, that is, each tree partitions the feature space through a sequence of decisions. The final prediction aggregates predicted probabilities across all trees. Each tree is trained on a bootstrap sample of the data. Training a tree involves partitioning the feature space using thresholds (i.e., identifying subsets of features and split thresholds) that maximize impurity reduction (Gini index) at each decision node. For a node i containing samples from K classes, the Gini index is defined as:

$$Gini\ index\ (i)\ =\ 1\ -\ \sum_{k=1}^{K} p_k^2,$$

where p_k denotes the proportion of samples that belong to class k. After training, each terminal leaf for each tree stores the empirical class distribution of the training samples that reached it, which defines the predicted probability for each class.

Training and testing data structure

A sample for the RF classifier corresponded to SRND parameters derived from LFPs at a single saccade event from one electrode. We labeled the sample as “remembered” if the image viewed during that saccade’s trial was later recognized by the patient, or “forgotten” if not. Here, a “trial” denotes one image presentation during the encoding task. The input feature vector comprised electrode spatial coordinates along the right-left (x), anterior-posterior (y), and superior-inferior axes (z), and the five SRND parameters. The electrode coordinates (x, y, z) for all participants were expressed in a common anatomical space, as detailed in the **Anatomical localization of the electrode** section. The five SRND parameters included SREP latency, peak-to-trough amplitude, peak time, and instantaneous power and phase of the preceding oscillation at half OCs before SREP latency.

Because multiple saccades, and thus multiple samples across electrode contacts, could occur within a trial, we grouped samples by trial before splitting the dataset into training and testing

sets. This choice ensures that all samples from the same trial are assigned exclusively to either training or testing, preventing the model from learning trial-specific idiosyncrasies, such as stimulus content. Therefore, by splitting data at the trial level, we evaluated whether SRND features alone carry information predictive of recognition memory. If the RF classifier successfully predicts recognition from SRND parameters at a specific location, it provides strong evidence that SRNDs reflect neural mechanisms relevant to visual encoding.

Training RF classifiers

Given class imbalance, we implemented balanced RF classifiers using the *imbalanced-learn* and *scikit-learn* Python libraries. A balanced RF classifier draws a bootstrap sample from the minority class (e.g., forgotten) and samples with replacement the same number of samples from the majority class (e.g., remembered). To learn the regional mapping between SRND parameters and visual encoding, while avoiding overfitting to electrode contact-specific locations, we added Gaussian spatial jitter to electrode coordinates in the training data using *normal* function from the *Numpy.random* Python library. We sampled the random *noise* from a normal distribution with standard deviation proportional to the variance of that coordinate across electrodes.

$$spatial\ jitter \sim N(0, 0.1 \times \sqrt{Var_{coordinates}})$$

To reliably evaluate model performance, we implemented 5-fold cross-validation using the *StratifiedKFold* function from the *Scikit-learn* Python library. Unless otherwise specified, we used default hyperparameters of 200 decision trees, a maximum depth of 20, and a minimum leaf size of 1. The results were from this setting unless otherwise noted. To verify that the chosen hyperparameters achieved an appropriate model complexity (i.e., neither underfitting nor overfitting), we systematically varied them and reevaluated model performance (**Figure 6F**).

Model evaluation

Our primary metric for model evaluation was balanced accuracy on held-out test data to account for class imbalance:

$$Balanced\ accuracy\ = \frac{1}{2}(TPR\ +\ TNR),$$

where TPR (true positive rate) is the proportion of correctly classified remembered trials among all remembered trials, and TNR (true negative rate) is the proportion of correctly classified forgotten trials among all forgotten trials. We also report the area under the receiver operating characteristic curve (ROC AUC) and standard accuracy. ROC AUC summarizes the true-positive

vs. false-positive trade-off across thresholds and is not affected by prevalence. Operationally, we constructed an ROC curve by plotting the TPR against the FPR (false positive rate) as the classification threshold varied from 0 to 1.

We evaluated model performance at the location-, saccade-, and trial levels. As we observed SREPs across the cerebrum, we reasoned that if the RF model learned local mapping between SRND parameters and visual encoding outcomes, combining predictions across locations within a saccade (e.g., spatial aggregation) should yield a more reliable estimate of the visual encoding outcome than location-level prediction. At the location-level, the model predicted the probability of being remembered and the class of each sample, that is, the set of five SRND parameters at one electrode contact location for a single saccade. For the RF classifier, the predicted probability $\widehat{P_{remember}}(i)$ for a sample i was computed as the mean of predicted probabilities estimated by all decision trees in the ensemble. Tree t's predicted probability for sample i, $p_{i,t}$, equals the proportion of training samples belonging to the "remembered" class in the terminal leaf where that sample falls.

$$\widehat{P_{remember}}(i) = \frac{1}{T}\sum_{t=1}^{T} p_{i,t},$$

where T is the number of trees and $p_{i,t}$ denotes the proportion of "remembered" samples in the terminal leaf reached by sample i in tree t. For each sample, we determined the predicted class label $\widehat{class}_i$ by comparing the predicted probability with 0.5:

$$\widehat{class}_i = \begin{cases} remembered, & if\ \widehat{P_{remember}}(i) \geq 0.5 \\ forgotten, & otherwise. \end{cases}$$

We computed location-level balanced accuracy and ROC AUC directly from these sample-level predictions.

$$ROC\ AUC\ = \int_0^1 TPR(FPR)d(FPR)$$

At the saccade level, we averaged the model's predicted probabilities across all electrode contacts during that saccade to obtain one probability of successful encoding per saccade. We obtained the predicted class $\widehat{class}_i$ similarly and computed balanced accuracy and $ROC\ AUC$ on these saccade-level predicted probabilities and classes. At the trial level, we aggregated predicted probabilities within a trial to yield a single predicted probability per trial. We then derived the predicted class and computed balanced accuracy and ROC AUC accordingly.

To test whether performance exceeded chance under the null hypothesis of no relationship between SRND features and successful visual encoding, we generated a null distribution by permuting labels. We then retrained and reevaluated the RF models on the permuted data using the same pipeline detailed in **Training and testing data structure**, **Training RF classifiers**, and **Model evaluation sections**. We compared the observed performance metrics, including balanced accuracy and ROC AUC, against their corresponding null distributions derived from permuted data.

To assess whether the model's probabilistic outputs meaningfully aligned with behavioral outcomes, we compared the average predicted probability between remembered and forgotten trials, as a complementary diagnostic of model validity. In addition, we quantified and compared the proportions of predicted remembered and forgotten saccades across actual visual-encoding outcomes. To assess inter-subject generalizability, we evaluated the model's performance separately for each subject's test data. For each subject, we computed the mean saccade- and contact-level balanced accuracy across CVs. To determine whether observed performance exceeded chance, we generated a subject-specific null distribution by retraining RF models on permuted labels using the identical pipeline. We quantified the percentile rank of each subject's observed performance relative to the null distribution at the individual level (**Figure 6 -Figure Supplement 1E**).

Assessing the reproducibility of learned mappings between SRND and visual encoding outcome

To verify that RF models learned the underlying mapping between SRND parameters and recognition memory performance, we quantified the reproducibility of learned mappings across cross-validations (CVs). We first analyzed the consistency of feature importance across folds. For each fold, the importance of a feature f_j was the mean reduction in Gini index across all decision nodes where the feature was used:

$$FI(f_j) = \frac{1}{T}\sum_{t=1}^{T}\sum_{n\in N_{j,t}}\frac{N_n}{N_t}\,\Delta G(n),$$

where T is the number of trees, $N_{j,t}$ is the set of nodes in tree t that split on feature f_j, N_t is the total number of samples used to train tree t, and N_n is the number of samples reaching node n, thus, $\frac{N_n}{N_t}$ represents the proportion of samples affected by the split at node n. $\Delta G(n)$ denotes the reduction in Gini impurity index at node n before and after the split:

$$\Delta G(n) = Gini\ index_{\text{parent}}(n) - \left(\frac{N_L}{N_n} Gini\ index_L + \frac{N_R}{N_n} Gini\ index_R\right),$$

where $Gini\ index_{\text{parent}}(n)$ is the Gini impurity index of the parent node n before splitting. $Gini\ index_L$, and $ini\ index_R$ denote the Gini impurity index of the left, and right children's node, respectively, where N_L and N_R denote their respective sample counts, and $N_n = N_L + N_R$.

To complement Gini index-based feature importance measures, we also evaluated the reproducibility of Shapley value–derived feature contributions. Originating from cooperative game theory, the Shapley value for a given sample and a feature represents the feature's marginal contribution to the model output[37]. For instance, for a sample x with model output $f(x)$, the Shapley value $Shapley_j(x)$ for a feature j is the average change in the prediction when adding the feature j to all possible subsets of the other features. (see **Shapley additive explanation** section for detailed computation). For each CV iteration, we computed the mean absolute Shapley value of each feature across training samples, which represents a model-agnostic quantification of each feature's marginal impact on the model output.

We normalized feature importances using the *norm* function from *Numpy.linalg* Python package and ranked them within each CV iteration. We quantified the concordance of feature rankings across folds, for both Gini index-based and Shapley-value derived feature importance, using Kendall's coefficient of concordance (W). Kendall's coefficient of concordance is a rank-based measure of agreement that ranges from 0 (no concordance) to 1 (perfect concordance).

$$W = \frac{12S}{m^2(n^3 - n)}$$

$$S = \sum_{j=1}^{n} \left(R_j - \bar{R}\right)^2$$

m is the number of folds, n is the number of features, R_j is the sum of ranks assigned to feature j across folds, and $\bar{R} = n(m+1)/2$ is the expected rank sum under uniform ranking.

To evaluate the statistical significance of the observed concordance, we generated a null distribution of W values derived from RF models trained on data with permuted class labels. For each permutation, we performed 5-fold CV and obtained a rank vector of feature importance for the five trained RF models. We then computed W values for 1,000 randomly sampled sets of five permuted-label models, yielding an empirical null distribution for comparison against the observed W.

In addition, we verified that trained RF models across CVs learned similar decision rules. Each decision rule corresponds to a split threshold on a specific feature that maximizes the reduction in impurity. We reasoned that if independently trained models converged on the same underlying mapping between SRND parameters and memory outcomes, the distributions of these split thresholds should be consistent across folds. For each RF model and each feature, we extracted split thresholds across all nodes and trees. To enable comparability across models, we established a set of reference bins for each feature. Specifically, we computed 100 quantile-based bin edges using the empirical distribution of split thresholds from a reference model (i.e., the model from the first fold). To ensure strictly increasing bin boundaries, we added a small constant (10^{-8}) to the second of any consecutive quantiles with equal values. We then ordered features along the x-axis and constructed a composite split histogram for each RF model, where each bin index represented a unique combination of feature identity and threshold range. In this representation, each histogram summarizes how frequently each feature contributed to splits within specific threshold intervals for a given fold.

To ensure comparability across folds, we normalized each composite split histogram by its total number of splits so that the resulting density distribution summed to one. We quantified the similarity of decision rules between pairs of RF models by computing the area under the absolute difference curve (AUC) between their corresponding kernel density estimates. We obtained kernel density estimates using the *gaussian_kde* function from the *scipy.stat Python* package, with a bandwidth parameter of 0.01.

To assess the statistical significance of the observed decision-rule similarity between pairs of RF models, we compared observed similarities from the actual data to a generated null distribution. Specifically, we permuted the class labels 20 times and applied 5-fold cross-validation to each permutation, yielding 100 RF models trained under random label conditions. From this pool, we randomly selected pairs of RF models and computed the decision rule similarity using the same procedure as for the actual data.

To further demonstrate that RF models convergently learned the mapping between SRND parameters and visual encoding outcome, we examined the consistency of predicted probabilities and classes across models trained on different CV iterations. For each pair of models trained on actual data but in different folds, we input 200 testing samples from the shared test set, which are observations that were not included in the training data of either model. We then computed Pearson's correlation coefficient between the predicted probabilities of "remembered" for the input testing samples using the *pearsonr* function from the *scipy.stats* Python package. For the same

model pairs, we also computed the disagreement ratio as the proportion of test samples for which the predicted classes differed, defined as disagreement ratio. This disagreement ratio captures divergence in binary decisions rather than probabilistic calibration. To assess the statistical significance of the observed output correlation and disagreement ratio across CV iterations, we generated their corresponding null distributions by randomly pairing RF models trained on permuted labels 200 times and recalculating these two output (dis)agreement metrics.

Logistic regression for linear mapping between SRND parameters and visual encoding outcomes

To determine if a linear relationship could explain the mapping between SRND parameters and visual encoding outcomes, we trained logistic regression models using the same dataset and class labels as those used for training RF models (see **Training RF classifiers** section). Given that the brain's functional organization is spatially nonlinear, we expected the logistic regression models to perform worse than the RF models. Nonetheless, this analysis served as a control to quantify the extent to which a linear model could capture the relationship between SRND features and visual encoding outcomes.

We implemented logistic regression with a logit link function and L2-norm regularization using the *LogisticRegression* class from the *Scikit-learn* Python package. The training and testing data structure followed the same rationale and procedures described in the **Training and Testing Data Structure** and **Training RF Classifiers** sections. To address class imbalance between samples labeled "remembered" and "forgotten", we applied the Synthetic Minority Over-Sampling Technique (SMOTE) using the *SMOTE* function from the *imblearn.over_sampling* package. In brief, SMOTE augments the minority class by generating synthetic samples in feature space[76]. For each minority-class sample, SMOTE generated synthetic examples along the line segments connecting that sample to any of its k minority class nearest neighbors (default k = 5), thereby reducing classifier bias toward the majority class.

As in RF mode training, we introduced spatial jitter to the electrode coordinate features to mitigate overfitting to exact electrode coordinates, and we implemented 5-fold cross-validation (see the **Training RF classifiers** section). After model training, we evaluated the logistic regression model's performance using balanced accuracy and ROC AUC on the held-out testing data. The quantification of these performance metrics and assessment of their statistical significance (i.e., comparing performance metrics to their permutation-based nulls) are detailed in the **Model evaluation** section. To interpret the learned mapping, we extracted the regression coefficients for each SRND parameter at each electrode contact location. Positive coefficients

indicated that higher feature values increased the likelihood of successful encoding, whereas negative coefficients indicated the opposite. Because logistic regression assumes linearity and monotonic effects, caution is warranted when interpreting coefficients for circular variables, that is, the phase of preceding oscillatory activity.

Shapley additive explanation

To interpret how specific SRND parameters contributed to the random forest (RF) model's predictions of visual encoding outcomes, we employed the Shapley additive explanation framework, a model-agnostic approach for explaining machine learning models[37]. The Shapley value is the average marginal contribution of a feature value across all possible coalitions, quantifying how much a given feature value increases or decreases the predicted probability of a machine learning model. Below, we provide the mathematical definitions and properties of Shapley values as formulated initially by Lloyd Shapley.

For a given sample x_i and feature j, the Shapley value $Shapley_{i,j}$ quantifies the *expected* marginal contribution of feature j to the model's predicted probability of successful visual encoding. The marginal contribution of a feature is defined as the *expected* change in the model's prediction when that feature is included compared with when it is excluded, given a specific subset of other features $S \subseteq F \setminus \{j\}$. Here, F is the full feature set, and S is a subset of F excluding feature j. Operationally, we computed the Shapley value by averaging marginal contributions across all possible subsets S, weighted by the probability of each subset that would occur if we randomly ordered all features. Specifically, a subset S of size $|S|$ would occur with probability $\frac{|S|!(|F|-|S|-1)!}{|F|!}$, which is the number of ways features could be ordered such that the features in S appear before feature j, and the remaining features in $F \setminus S$ appear after j. For example, if $F = (j_1, j_2, j_3, j)$, and $S = \{j_1, j_2\}$, there are $|S|! \times (|F| - |S| - 1)! = 2! \times 1! = 2$ permutations where features in S appear before feature j: $(j_1, j_2, j, j_3)$and (j_2, j_1, j, j_3). Mathematically, Shapley value is defined as:

$$\text{Shapley}_{i,j} = \sum_{S \subseteq F \setminus \{j\}} \frac{|S|!\ (|F| - |S| - 1)!}{|F|!} \left[f_{S \cup \{j\}}\left(x_{i,S \cup \{j\}}\right) - f_S\left(x_{i,S}\right) \right]$$

where |S| is the number of features in subset S, and |F| is the total number of features. The term $x_{i,S}$ denotes the subset of feature values from sample x_i corresponding to the feature set $S \subseteq F \setminus$

$\{j\}$, while $x_{i,S\cup\{j\}}$ denotes the same sample but with feature j additionally included. $f_S(x_{i,S})$ represents the expected model prediction when only features in S are known.

$$f_S(x_{i,S}) = E_{x_{F\setminus S}}[f([x_{i,S}, x_{i,F\setminus S}])]$$
$$= \int f([x_{i,S}, x_{i,F\setminus S}])p(x_{F\setminus S}|x_{i,S})dx_{F\setminus S},$$

where $x_{F\setminus S}$ represents all the other feature values that are not in S, $x_{i,S}$ is the subset of feature values for sample i corresponding to features in S. Therefore, $f([x_{i,S}, x_{i,F\setminus S}])$ is the model output from a complete feature vector where the features in subset S take the actual values from sample i (i.e., $x_{i,S}$), and the remaining features in $F \setminus S$ take some possible values drawn from the distribution $\sim p(x_{F\setminus S}|x_{i,S})$. Thus, $f_{S\cup\{j\}}(x_{i,S\cup\{j\}}) - f_S(x_{i,S})$ represents the marginal contribution of feature j to the model's prediction for x_i. The weighting term $\frac{|S|!\,(|F|-|S|-1)!}{|F|!}$ guarantees additivity, meaning that each sample's prediction can be exactly decomposed into the sum of feature contributions. By summing the Shapley value for a sample x_i across all features, we get:

$$\sum_{j\in F} Shapley_{i,j} = \sum_{j\in F}\sum_{S\subseteq F\setminus j} \frac{|S|!\,(|F|-|S|-1)!}{|F|!}[f_{S\cup j}(x_{i,S\cup j}) - f_S(x_{i,S})]$$
$$= f(x_i) - f_\emptyset \;=\; f(x_i) - E[f(x)]$$

In tree-based models, $f_S(x_{i,S})$ can be expressed as the expectation of the model's output conditioned on x_S.

$$f_S(x_{i,S}) = \sum_{L\in \text{leaves}} P(L|x_{i,S})\, v_L,$$

where $x_{i,S}$ denotes the subset of feature values from sample x_i corresponding to the feature set $S \subseteq F$, v_L denotes the predicted value (e.g., predicted probability of successful visual encoding) at leaf L. $P(L|x_{i,S})$ represents the probability of reaching leaf L given only the observed features $x_{i,S}$.

For a given leaf L, we computed this probability $P(L|x_{i,S})$ using the chain rule of probability applied along the path from the root node to L, that is, the product of conditional probabilities of following each successive branch along this path. For node n splits on a feature in S, the observed feature value $x_{i,S}$ deterministically specifies which branch the sample follows. The probability of taking the branch toward L is 1 if $x_{i,S}$ satisfies the split condition for that branch, and 0 otherwise.

If node n splits on a feature not in S, the conditional probability of following the branch toward L is empirical frequency $r_{n\to L}/r_n$ from the training data, where r_n is the number of training samples reaching node n, and $r_{n\to L}$ is the number that proceed down the branch toward L. In other words, given training data, the tree defines a discrete probability distribution over leaves $P(L \mid x_{i,S})$, the likelihood that a random training sample reaches leaf L when only features in S are known.

$$P(L \mid x_{i,S}) = \prod_{n \in path(L)} \begin{cases} 1, & split\ feature(n) \in S\ AND\ x_{i,S}\ directs\ x_i\ toward\ L \\ 0, & split\ feature(n) \in S\ AND\ x_{i,S}\ down\ a\ different\ branch \\ r_{n\to L}/r_n, & split\ feature(n) \notin S \end{cases}$$

To illustrate, consider a simple decision tree in which the root node (Node 0) splits on feature A with a threshold of 5. The left branch ($A < 5$) leads directly to a single leaf L_1 with an output value v_{L_1}= 0.8, while the right branch ($A \geq 5$) leads to another leaf L_2 with v_{L_2} = 0.2. 60 % of the training sample falls on the left side of the split (L_1) and 40 % on the right (L_2). These proportions define the empirical branch probabilities $r_{\text{left}}/r_{\text{root}} = 0.6$ and $r_{\text{right}}/r_{\text{root}} = 0.4$. The table below summarizes the tree structure.

Node	Split	Left	Right	Training proportion
0	Left if $A < 5$	$L_1(v_{L_1} = 0.8)$	$L_2(v_{L_2} = 0.8)$	$r_{0\to L_1}/r_0 = 0.6$ $r_{0\to L_2}/r_0 = 0.4$

To calculate $Shapley_{i,A}$ for $x_{i,A} = 3$, we have

$$Shapley_{i,A} = \sum_{S \subseteq F \setminus \{A\}} \frac{|S|!\ (|F| - |S| - 1)!}{|F|!} \left[f_{S\cup\{A\}}(x_{i,S\cup\{A\}}) - f_S(x_{i,S})\right].$$

As *F* = *A, S* can only be ∅. *Note that* $|\emptyset| = 0$, *therefore*

$$Shapley_{i,A} = \frac{|A|!\ (|A| - |\emptyset| - 1)!}{|A|!} \left[f_A(x_{i,A}) - f_\emptyset\right]$$

$$= f_A(x_{i,A}) - f_\emptyset$$

$$f_\emptyset = \sum_{L \in leaves} P(L|x_{i,\emptyset}) v_L$$

$$= r_{0\to L_1}/r_0 \cdot v_{L_1} + r_{0\to L_2}/r_0 \cdot v_{L_2}$$

$= 0.6 \times 0.8 + 0.4 \times 0.2 = 0.56$

$$f_A(x_{i,A}) = \sum_{L \in leaves} P(L|x_{i,A}) v_L$$

$$= r_{0\to L_1}/r_0 \cdot v_{L_1} + r_{0\to L_2}/r_0 \cdot v_{L_2}$$

$= 1 \times 0.8 + 0 \times 0.2 = 0.8$

Now consider a deeper decision tree in which the root node (Node 0) splits on feature A at a threshold of 5. Samples with $A < 5$ proceed to the left child node (Node 1), whereas those with $A \geq 5$ terminate at a right leaf L_3 (v_{L_3}= 0.4). At Node 1, the data are further partitioned based on feature B with a threshold of 2: samples with $B < 2$ reach leaf L_1 with v_{L_1}=0.6, and samples with $B \geq 2$ reach leaf L_2 with v_{L_2}= 0.5. At the root node, the left and right branch proportions are $r_{0\to 1}/r_0 = 0.6$ and $r_{0\to L_3}/r_0 = 0.4$ respectively. At Node 1, the split on feature B partitions the data evenly, with $r_{1\to L_1}/r_1 = 0.5$ and $r_{1\to L_2}/r_1 = 0.5$. The table below summarizes the tree structure.

Node	Split	Left	Right	Training proportion
0	Left if $A < 5$	$Node\ 1$	$L_3(v_{L_3} = 0.4)$	$r_{0\to 1}/r_0 = 0.6$ $r_{0\to L_3}/r_0 = 0.4$
1	Left if $B < 2$	$L_1(v_{L_1} = 0.6)$	$L_2(v_{L_2} = 0.5)$	$r_{1\to L_1}/r_1 = 0.5$ $r_{1\to L_2}/r_1 = 0.5$

We illustrate how to calculate $Shapley_{i,A}$ with $x_{i,\{A,B\}} = [1,1]$. As $F = \{A, B\}$, S can be $\emptyset$ or $\{B\}$.

$$Shapley_{i,A} = \sum_{S \subseteq F \setminus \{A\}} \frac{|S|!\ (|F| - |S| - 1)!}{|F|!} \left[f_{S\cup\{A\}}(x_{i,S\cup\{A\}}) - f_S(x_{i,S})\right]$$

$$= \frac{1}{2}\left[f_A(x_{i,A}) - f_\emptyset\right] + \frac{1}{2}\left[f_{\{A,B\}}(x_{i,\{A,B\}}) - f_B(x_{i,B})\right]$$

Similarly, we have

$$f_\emptyset = \sum_{L \in leaves} P(L|x_{i,\emptyset}) v_L$$

$$= P(L_1|x_{i,\emptyset})v_{L_1} + P(L_2|x_{i,\emptyset})v_{L_2} + P(L_3|x_{i,\emptyset})v_{L_3}$$

$$= r_{0\to 1}/r_0 \cdot r_{1\to L_1}/r_0 \cdot v_{L_1} + r_{0\to 1}/r_0 \cdot r_{1\to L_2}/r_0 \cdot v_{L_2} + r_{0\to L_3}/r_0 \cdot v_{L_3}$$

$$= 0.6 \times 0.5 \times 0.6 + 0.6 \times 0.5 \times 0.5 + 0.4 \times 0.4 = 0.49$$

$$f_A(x_{i,A}) = \sum_{L \in leaves} P(L|x_{i,A})v_L$$

$$= P(L_1|x_{i,A})v_{L_1} + P(L_2|x_{i,A})v_{L_2} + P(L_3|x_{i,A})v_{L_3}$$

$$= 0.5 \times 0.6 + 0.5 \times 0.5 + 0 \times 0.4 = 0.55$$

$$f_B(x_{i,B}) = \sum_{L \in leaves} P(L|x_{i,B})v_L$$

$$= P(L_1|x_{i,B})v_{L_1} + P(L_2|x_{i,B})v_{L_2} + P(L_3|x_{i,B})v_{L_3}$$

$$= 0 \times 0.6 + 0 \times 0.5 + 1 \times 0.4 = 0.4$$

$$f_{\{A,B\}}(x_{i,\{A,B\}}) = \sum_{L \in leaves} P(L|x_{i,\{A,B\}})v_L$$

$$= P(L_1|x_{i,\{A,B\}})v_{L_1} + P(L_2|x_{i,\{A,B\}})v_{L_2} + P(L_3|x_{i,\{A,B\}})v_{L_3}$$

$$= 1 \times 0.6 + 0 \times 0.5 + 0 \times 0.4 = 0.6$$

Therefore, $Shapley_{i,A} = \frac{1}{2}[0.55 - 0.49] + \frac{1}{2}[0.6 - 0.4] = 0.13$

Similarly, we have

$$Shapley_{i,A} = \frac{1}{2}[f_B(x_{i,B}) - f_\emptyset] + \frac{1}{2}[f_{\{A,B\}}(x_{i,\{A,B\}}) - f_A(x_{i,A})]$$

$$= \frac{1}{2}[0.4 - 0.49] + \frac{1}{2}[0.6 - 0.55] = -0.02$$

We have $Shapley_{i,A} + Shapley_{i,B} = f(x_i) - E[f(x)] = 0.6 - 0.49 = 0.11$.

We implemented this analytical solution using *TreeExplainer* function from the *SHAP* Python package. For each input sample, this function recursively traverses all decision paths through each tree, computing $P(L|x_{i,S})$ for each feature subset S. Given that our previous analyses demonstrated high reproducibility of learned mapping across CV iterations, and that Shapley value computation is computationally intensive, we computed Shapley values for the

trained RF model in a randomly selected CV iteration. This analysis allows us to identify feature values that increase or decrease the model's predicted probability of successful encoding, thereby translating the RF classifier into interpretable electrophysiological rules.

To further illustrate the meaning of Shapley values, we compared the feature value-Shapley value plots with partial dependence plots (**Figure 7A–B**). A partial dependence plot provides a global, approximate summary of how the model's output changes as that feature varies while averaging over the effects of all other features. In contrast, Shapley values capture the local (e.g., specific to an anatomical location), sample-specific contribution of each feature by considering all possible feature interactions. To visualize how multiple features jointly influenced model prediction of successful visual encoding, we systematically varied SRND parameters for each electrode contact. We input the feature combination into the trained RF model to estimate the probability of successful encoding. We then reconstructed waveforms from the SRND parameters and assigned the predicted encoding probability to each waveform (**Figure 7C**).

Shapley value-informed thresholds and directions

To better interpret the RF model's mapping between SRND parameters and visual encoding outcomes, we derived Shapley value–informed thresholds and directions for each feature at each electrode contact location. Conceptually, this procedure mimics the decision process of a random forest and allows us to identify the range of SRND parameters conducive to successful visual encoding. For non-circular features, such as peak-to-trough amplitude, we sorted observations by their feature values. We then identified a change point τ_f that minimized the within-segment variance of Shapley values, partitioning values into encoding-favorable versus unfavorable ranges.

$$\tau_f = \arg\min_t \left[\sum_{x_i < t} \left(Shapley_{i,f} - \overline{s_{<t}} \right)^2 + \sum_{x_i \geq t} \left(Shapley_{i,f} - \overline{s_{\geq t}} \right)^2 \right],$$

where $Shapley_{i,f}$ is the Shapley value for sample x_i and feature f, and $\overline{s_{<t}}$ and $\overline{s_{\geq t}}$ are mean Shapley values on either side of the candidate threshold t.

For the circular feature (i.e., instantaneous phase of preceding oscillations), we identified the angular window $\left[\theta_{1_f}, \theta_{2_f}\right]$ on the unit circle that minimized the variance of Shapley values inside versus outside the window.

$$\left[\theta_{1_f}, \theta_{2_f}\right] = \arg\min_{\theta_1,\theta_2 \in [0,2\pi)} \left(\sum_{i \in W(\theta_1,\theta_2)} \left(Shapley_{i,f} - \overline{s_W}\right)^2 + \sum_{i \notin W(\theta_1,\theta_2)} \left(Shapley_{i,f} - \overline{s_{\neg W}}\right)^2 \right),$$

where $W(\theta_1, \theta_2)$ denotes the set of samples whose feature value lies within the angular interval $[\theta_1, \theta_2]$. $\overline{s_W}$ and $\overline{s_{\neg W}}$ denote mean Shapley values of samples inside and outside the candidate window, respectively.

For each feature, we defined the direction (higher vs. lower or inside vs. outside) associated with successful encoding by comparing the mean Shapley values for observations on either side of the identified threshold, or, for circular features, inside vs. outside the angular window. For non-circular features, if the mean Shapley value on one side was higher, feature values that are higher (or lower) than τ_f contributed to successful encoding. For circular features, we computed the mean Shapley value within and outside the angular window $\left[\theta_{1_f}, \theta_{2_f}\right]$. We defined the Shapley value-informed direction as the phase range yielding the higher mean Shapley value. We then quantified how strongly each observation's feature value aligned with the encoding-favorable direction by computing a recall likelihood $L_{recall}(i)$. For a non-circular feature and a sample x_i,

$$L_{recall}(i) = 0.5 \pm \frac{\left|x_{i,f} - \tau_f\right|}{3\sigma_f},$$

where the sign depends on the feature's direction ("higher" or "lower" associated with successful encoding), and $\sigma_f$is the standard deviation of the feature computed from the training data. For circular features, let the phase be $\phi_i \in [0,2\pi)$ and the window $W_f = \left[\theta_{1,f}, \theta_{2,f}\right]$. For sample x_i with direction as "within",

$$L_{recall}(i) = 0.5 + (2 \times I_W(\phi_i) - 1) \times d_W(\phi_i)/(3\sigma_f),$$

$$I_W(\phi) = \begin{cases} 1, if\ (\theta_1 \le \theta_2 \text{ and } \theta_1 \le \phi \le \theta_2) \text{ or } (\theta_1 > \theta_2 \text{ and } \phi \ge \theta_1 \text{ or } \phi \le \theta_2) \\ 0, \qquad\qquad\qquad\qquad\qquad\qquad\qquad\qquad otherwise, \end{cases}$$

$$\Delta_c(a, b) = \min(|a - b|, 2\pi - |a - b|),$$

$$d_W(\phi) = \min\left(\Delta_c(\phi, \theta_1), \Delta_c(\phi, \theta_2)\right).$$

$d_W(\phi)$ represents the minimum circular distance from an angle ϕ to either boundary of the encoding-favorable phase window. We clipped $L_{recall}(i)$ to the interval [0,1].

To validate that the Shapely value-informed thresholds and directions reflected meaningful SRND-visual encoding mappings, we compared recall likelihood averaged across electrode contacts between remembered and forgotten trials. In addition, we evaluated classification performance based on Shapley value-informed thresholds and compared the performance metrics, including balanced accuracy and ROC AUC, to their surrogate null distribution. Specifically, for each feature, we generated surrogate models by uniformly resampling feature thresholds within a range determined by the empirical minimum and maximum of the observed thresholds, while randomly permuting the direction. We then recompute recall likelihoods based on the surrogate configuration. Based on recall likelihood, for each sample and each feature, we classified it as "remembered" if $L_{recall}(i) \geq 0.5$, and those with $L_{recall}(i) < 0.5$ as forgotten. We then computed balanced accuracy based on class prediction and ROC AUC based on recall likelihood, for electrode contact, saccade, and trial level. Please see **Model evaluation** section for computation details.

Visualization of the SRND-visual encoding relationship

After confirming that the Shapley value-informed thresholds and directions distinguished successful from unsuccessful visual encoding outcomes, we visualized them to illustrate how SRND features contributed to successful visual encoding across anatomical regions (**Figure 7I–M**). For non-circular features, we used two complementary color schemes to represent the Shapley-informed direction, that is, whether higher or lower feature values favored successful encoding. A red colormap (light to dark red) indicated that higher feature values were associated with successful encoding, whereas a blue colormap (light to dark blue) indicated that lower feature values were associated with successful encoding. We used color saturation to reflect the magnitude of the threshold, with more saturated hues corresponding to more extreme thresholds, in other words, higher thresholds for "higher" directions and lower thresholds for "lower" directions.

For circular features (i.e., the instantaneous phase at 0.5 OCs before EP latency), we computed the circular mean of the encoding-favorable phase window $\left[\theta_{1_f}, \theta_{2_f}\right]$ when the direction was "within," or its complementary phase range $\neg\left[\theta_{1_f}, \theta_{2_f}\right]$ when the direction was "outside." We color-coded the circular mean of the encoding-favorable phase using the *twilight* circular colormap from the *Matplotlib* Python Package.

To visualize the SRND-visual encoding relationship at electrode contact resolution, we projected the 3D cortical and subcortical surfaces, along with electrode coordinates, onto a 2D plane and discretized this space into a 5 mm × 5 mm grid, as detailed in the **Spatial visualization**

of SREP characteristics section. We assigned each electrode contact's mean absolute Shapley value or Shapley value-informed threshold to grid cells within 10 mm. Grid cells with no assigned values were rendered transparent. The resulting heatmaps depict the regional gradient of model contributions, with color intensity encoding the mean absolute Shapley values. Background anatomical surfaces were overlaid for spatial reference and color-coded by anatomical region without encoding Shapley values.

RF regression for predicting saccade direction

To test whether SRND parameters contain information about saccade direction, we split the training and testing datasets at the saccade level and trained RF regressors. Similar to the random forest model for classifying remembered vs. forgotten trials, the random forest regressor consists of an ensemble of decision trees, and each tree splits the data recursively based on feature thresholds. During training, the random forest regressor learned a set of features and split thresholds that minimize mean square error within each split node. After training, the output at each leaf node was the average target values across the training samples that reached that node.

The input feature set was identical to that used for visual encoding outcome prediction parameters (i.e., SREP latency, peak-to-trough amplitude, peak time, phase, and power of preceding oscillatory activity). Training RF regressors largely followed the same framework described in the **Training RF classifiers** section, including adding Gaussian spatial jitter to electrode contact location and using 5-fold cross-validation. In addition, we verified that the RF regression model was neither overfitting nor underfitting by systematically varying key hyperparameters (**Figure 8-Figure Supplement 1A**). The differences, compared to training an RF classifier to learn the SRND-visual encoding mapping, were the target variable, objective function, and model output. Because saccade direction is a circular variable, its numerical representation in radians is discontinuous at the $\{0, 2\pi\}$ boundary. For instance, 0 rad and 2π rad correspond to the same direction but differ numerically by 2π. To allow the RF regression model to optimize the loss function in Euclidean space and avoid treating saccade direction as a linear quantity, we transformed each saccade's direction θ into a two-dimensional direction vector in Cartesian space:

$$y_i = [\sin(\theta_i),\ \cos(\theta_i)].$$

This maps angular saccade directions to continuous coordinates in Euclidean space, where opposite directions remain far apart in vector space, while equivalent directions are identical, preserving angular continuity. After transformation, we trained RF regression models

using a standard mean squared error (MSE) objective function. We implement the RF regression model using *RandomForestRegressor* from the *Scikit-learn* Python package. In brief, each decision tree learned feature-split thresholds that minimized MSE over the two-dimensional direction vectors. For each sample, the trained RF model routes it to a terminal leaf in every individual decision tree. The predicted output for that sample from a single tree is the mean direction vector computed across all training samples that reached the same terminal leaf. The final ensemble prediction is the average predicted direction vector across all trees $\widehat{y_i}$. We reconstructed the predicted saccade direction $\hat{\theta}_i$ for sample i in angular space using the two-argument arctangent function:

$$\hat{\theta}_{\mathrm{i}} = \mathrm{atan2}\left(\widehat{y_{i_1}}, \widehat{y_{i_2}}\right).$$

RF regression evaluation

We evaluated RF regression model performance on held-out testing data using both MSE and mean absolute error (MAE). Specifically, we calculated the MSE between the predicted and true direction vectors.

$$\mathrm{MSE} = \frac{1}{N}\sum_{i=1}^{N} ||\widehat{y_i} - y_i||^2,$$

where $||\cdot||$ denotes the Euclidean norm. Lower MSE values indicate better prediction accuracy. In addition, we computed the MAE between the reconstructed angular predictions and actual saccade directions

$$\mathrm{MAE} = \frac{1}{N}\sum_{i=1}^{N} \left|\hat{\theta}_i - \theta_i\right|,$$

where angular differences $\widehat{\theta_i} - \theta_i$ were wrapped into the range $[-\pi, \pi]$ before taking the absolute value. We computed the MSE and MAE at both the location and saccade levels. For saccade-level evaluation, we averaged the predicted direction vectors across all electrodes within each saccade. To assess statistical significance, we generated null distributions for MSE and MAE by repeating the cross-validation training procedure with permuted saccade directions. Specifically, for each of 100 permutations, we randomly shuffled target direction vectors y_i, repeated the RF regression model training procedure, and computed the performance metrics.

Quantifying directional modulation

To confirm that SRND parameters did not encode saccade direction for most electrode contacts, we compared the observed testing MSE for each electrode contact against its null distribution from permutations. We calculated the contact-wise percentile rank of testing MSE relative to its null distribution. We identified direction-informative electrode contacts as those with observed MSEs below the 5th percentile of their null distribution. To complement the model-based approach, we quantified directional non-uniformity of SRND parameters. For each electrode contact and feature, we estimated the circular kernel density of the feature values as a function of saccade direction. Operationally, we discretized the angular space into 60 equal bins covering $0 - 2\pi$ radians. For each bin centered at angle ϕ_j, we computed the mean feature value of saccades within a $\pm 6°$ window around ϕ_j. For circular features (i.e., instantaneous phase), we computed the circular mean using the *circmean* function from the *scipy.stats* Python package. We then applied von Mises kernel regression, implemented via *vonmises* from the *scipy.stats python package* (concentration parameter κ = 15).

For each feature, we quantified directional non-uniformity D_f as the integral of the absolute difference between the circular kernel density and its mean across the angular domain:

$$D_f = \int_0^{2\pi} \left| p_f(\theta) - \overline{p_f} \right| \, d\theta,$$

where $p_f(\theta)$ denotes the kernel density estimate for feature f, and $\overline{p_f}$ is its circular mean. A higher D_f value indicates greater directional modulation.

To evaluate statistical significance, we generated null distributions of D_f by permuting saccade directions 200 times and recomputing the directional non-uniformity for each permutation. We then computed the percentile rank of directional non-uniformity for each electrode contact and feature relative to the corresponding null distribution. For each feature, we computed the proportion of electrode contacts whose directional non-uniformity is less than the 95th percentile of their relative null distribution, indicating a lack of direction-specific modulation.

Neural networks for identifying saccade direction information in SRND

To validate the observed lack of saccade-direction information in SRND parameters, we implemented several complementary modeling approaches. These analyses aim to demonstrate that the lack of saccade-direction encoding across nonlinear, linear, and binary classification frameworks, and therefore confirm that SRND primarily reflects cognitive rather than motoric components of saccade processing. Specifically, we trained (1) neural networks with either

saccade direction or transformed direction vector as output, (2) a linear model for angular prediction, and (3) a binary RF classifier to distinguish leftward versus rightward saccades. These analyses aimed to detect any nonlinear or linear mapping between SRND parameters and saccade direction.

As a nonlinear control model, we implemented a feedforward neural network consisting of three fully connected hidden layers, each followed by a Rectified Linear Unit activation function using the *PyTorch* Python package. The input layer received the same feature set as the RF models, including electrode spatial coordinates and SRND parameters, described in the **Training and testing data structure** section. The network's output layer contained two units representing the two-dimensional Cartesian saccade direction vector $[\sin(\theta), \cos(\theta)]$. To ensure that predictions represented saccade directions, we required the network to normalize its outputs to the unit circle:

$$\hat{y}_i = \frac{u_i}{|u_i|}, \qquad u_i = f_\theta(x_i),$$

where $f_\theta(x_i)$ denotes the network output for input x_i. We trained this neural network to minimize MSE between predicted and true direction vectors. Consistent with previous machine learning model training and evaluation, we used the 5-fold cross-validation procedure. We trained the network using the Adam optimizer from the *PyTorch* Python package with a learning rate of 1×10^{-3}, a batch size of 256, and up to 50 epochs.

To confirm that the transformation of saccade direction into a two-dimensional Cartesian direction vector did not prevent the neural network from learning the relationship between SRND parameters and saccade direction, we implemented a complementary neural network trained to minimize angular loss directly. This model had the same three-layer architecture and inputs as above, but used a single-unit output layer representing the angular direction in radians. We used a loss function to represent the wrapped angular distance between the predicted direction ($\hat{\theta}$) and true directions (θ):

$$\mathcal{L}_{angular} = 1 - cos(\hat{\theta} - \theta).$$

This formulation penalizes large angular deviations and is continuous at the $0 - 2\pi$ boundary. We evaluated both neural networks at the electrode contact and saccade levels using MSE, computed analogously to the RF regression evaluation (see the **RF regression evaluation** section). For the network with two outputs, we reconstructed the predicted angular direction from the predicted

direction vector using the two-argument arctangent function. We then computed the MSE between reconstructed and true saccade directions after wrapping angular differences into the range [−180°, 180°]. To evaluate whether prediction accuracy exceeded chance, we generated null distributions of MSE by training neural networks with the same architecture on data with permuted saccade directions. Specifically, we randomly shuffled target direction vectors $[\sin(\theta), \cos(\theta)]$ across saccades 100 times and repeated the full cross-validation training and evaluation procedure for each permutation.

Kernel regression by minimizing the von Mises negative log-likelihood

To test whether SRND parameters could linearly explain saccade direction, we implemented a linear regression by minimizing the von Mises negative log-likelihood. The von Mises distribution is the circular analog of a Gaussian distribution for angular data, modeling angular data defined on the unit circle while accounting for the periodicity at the 0–2π boundary. Formally, we modelled the saccade direction θ_i as a circular variable whose mean direction μ_i depends linearly on the SRND features:

$$\mu_i = X_i\beta,$$

where X_i is the feature vector comprising SRND parameters and electrode coordinates, and β is the vector of regression coefficients to be estimated. Under the von Mises assumption, the probability density of observing θ_i is given by

$$p(\theta_i \mid \mu_i, \kappa) = \frac{1}{2\pi I_0(\kappa)} \exp[\kappa \cos(\theta_i - \mu_i)],$$

where κ is the concentration parameter which we set to 1. $I_0(\kappa)$ is the modified Bessel function of the first kind of order 0. We estimated the regression parameters by minimizing the von Mises negative log-likelihood:

$$\mathcal{L}(\beta) = -\sum_i \kappa \cos(\theta_i - X_i\beta) + N\log\big(2\pi I_0(\kappa)\big),$$

To fit this model, we used the BFGS optimization algorithm implemented via the *minimize* function from the *scipy.optimize* Python package. We obtained the predicted saccade direction from the model as

$$\widehat{\mu_i} = X_i\widehat{\beta},$$

$$\widehat{\theta_i} = \widehat{\mu_i}\ mod\ 2\pi,$$

where $\hat{\beta}$ denotes the estimated model parameters, and mod denotes the modulo operation, which ensures that predicted directions remain within the circular domain $[0,2\pi)$.

Consistently, we evaluated model performance using contact- and saccade-level MSEs between predicted and true saccade directions. We assessed the statistical significance of prediction accuracy by comparing MSEs to their null distributions generated via 100 permutations of saccade labels.

Binary classification of left vs. right saccades

To parallel the classification framework used for predicting successful visual encoding, we also trained a balanced RF classifier to discriminate between leftward and rightward saccades. We binarized saccade directions as left and right based on their angular position. All procedures for data splitting, feature selection, model training, evaluation, and statistical testing followed those described in the **Random forest classifier**, **Training and testing data structure**, **Training RF classifiers**, and **Model evaluation** sections.

Prediction of subsequent saccade direction

Finally, to determine whether SRND represents neural computations related to the planning of subsequent eye movements, we trained an RF regressor to predict subsequent saccade direction based on SRND parameters at the current saccade. We defined subsequent saccades using combined temporal and spatial proximity criteria: (1) For the temporal proximity criterion, for each valid saccade, we searched for the next non-fixation saccade occurring within the same trial and within 500 ms of the current saccade offset; (2) The spatial proximity criterion required that the difference between the gaze positions at saccade offset for the current and subsequent saccades be less than 20% of the screen dimension in both the x and y axes.

For each valid pair of saccades, we used the direction of the next saccade as the target variable in the RF regression model. Model training and evaluation followed the same procedures as described in the **RF regression for predicting saccade direction** section. We quantified prediction performance using MSE between predicted and true subsequent saccade direction vectors and MAE between predicted and true subsequent saccade directions in radius. We assessed statistical significance by comparing observed performance against null distributions derived from models trained on data with permuted saccade directions.

Quantification and Statistical Analysis

All data were analyzed and plotted with MATLAB and Python. For comparison between two conditions, when assumptions of normality and equal variances were met, we used Student's unpaired t-test. When samples were paired (e.g., within-subject or within-electrode comparisons) and these assumptions were met, we used paired Student's t-tests. When these assumptions were not met, we used the Mann–Whitney U test for comparisons between independent samples, and the Wilcoxon signed-rank test for paired comparisons. For comparison of the mean direction between two (or more) circular distributions, we used Watson-Williams F test. For comparison of the full circular distributions (i.e, differences in shape), we used Mardia–Watson–Wheeler test. For testing if the distribution of intertrial correlation differed from baseline, we used Kolmogorov-Smirnov tests.

For linear regression analyses, we assessed the statistical significance of regression coefficients using two-sided t-tests. For correlation analyses, we converted Spearman's or Pearson's correlation coefficient to t-statistics and assessed their significance against the Student's t-distribution. For testing if a learning model's performance exceeded chance, we performed permutation testing, in which data labels were randomly permuted to generate a surrogate null distribution; and we compared the true performance metric value to this distribution to obtain a percentile-based p-value.

Statistical significance is defined as NS (non-significant), $*$ $p < 0.05$, $**$ $p < 0.01$, $***$ $p < 0.001$. We report statistical details in the Results section and figure legends, including the statistical tests used, statistics, effect size, and exact value of n. Effect sizes are reported as: regression coefficients for linear models, Pearson's or Spearman's r for correlation analyses, Cohen's d or rank-biserial correlation for pairwise comparisons, and percentile score relative to the null distribution for permutation tests. When more than 10 comparisons were used to support a conclusion, Bonferroni correction was applied.

References

1. Rayner, K., McConkie, G. W. & Zola, D. Integrating information across eye movements. *Cognit. Psychol.* **12**, 206–226 (1980).

2. Wurtz, R. H. NEURONAL MECHANISMS OF VISUAL STABILITY. *Vision Res.* **48**, 2070–2089 (2008).

3. Jutras, M. J., Fries, P. & Buffalo, E. A. Oscillatory activity in the monkey hippocampus during visual exploration and memory formation. *Proc. Natl. Acad. Sci.* **110**, 13144–13149 (2013).

4. Doucet, G., Gulli, R. A., Corrigan, B. W., Duong, L. R. & Martinez-Trujillo, J. C. Modulation of local field potentials and neuronal activity in primate hippocampus during saccades. *Hippocampus* **30**, 192–209 (2020).

5. Lee, S., Dormán, H., Nádasdy, Z. & Gothard, K. M. Saccade-related LFP power transients in the primate amygdala and hippocampus linked to the perception of social status. *Proc. Natl. Acad. Sci.* **123**, e2516365123 (2026).

6. Rajkai, C. *et al.* Transient Cortical Excitation at the Onset of Visual Fixation. *Cereb. Cortex* **18**, 200–209 (2008).

7. Ito, J., Maldonado, P., Singer, W. & Grün, S. Saccade-Related Modulations of Neuronal Excitability Support Synchrony of Visually Elicited Spikes. *Cereb. Cortex* **21**, 2482–2497 (2011).

8. Katz, C. N. *et al.* A corollary discharge mediates saccade-related inhibition of single units in mnemonic structures of the human brain. *Curr. Biol.* **32**, 3082-3094.e4 (2022).

9. Sobotka, S. & Ringo, J. L. Saccadic eye movements, even in darkness, generate event-related potentials recorded in medial septum and medial temporal cortex. *Brain Res.* **756**, 168–173 (1997).

10. Andrillon, T., Nir, Y., Cirelli, C., Tononi, G. & Fried, I. Single-neuron activity and eye movements during human REM sleep and awake vision. *Nat. Commun.* **6**, 7884 (2015).

11. Yao, T., Ketkar, M., Treue, S. & Krishna, B. S. Visual attention is available at a task-relevant location rapidly after a saccade. *eLife* **5**, e18009 (2016).

12. Gallant, J. L., Connor, C. E., Rakshit, S., Lewis, J. W. & Van Essen, D. C. Neural responses to polar, hyperbolic, and Cartesian gratings in area V4 of the macaque monkey. *J. Neurophysiol.* **76**, 2718–2739 (1996).

13. Tan, G., Xu, K., Liu, J. & Liu, H. A Trend on Autism Spectrum Disorder Research: Eye Tracking-EEG Correlative Analytics. *IEEE Trans. Cogn. Dev. Syst.* **14**, 1232–1244 (2022).

14. Hedrich, T., Pellegrino, G., Kobayashi, E., Lina, J. M. & Grova, C. Comparison of the spatial resolution of source imaging techniques in high-density EEG and MEG. *NeuroImage* **157**, 531–544 (2017).

15. Lins, O. G., Picton, T. W., Berg, P. & Scherg, M. Ocular artifacts in recording EEGs and event-related potentials. II: Source dipoles and source components. *Brain Topogr.* **6**, 65–78 (1993).

16. Kovach, C. K. *et al.* Manifestation of ocular-muscle EMG contamination in human intracranial recordings. *NeuroImage* **54**, 213–233 (2011).

17. Crapse, T. B. & Sommer, M. A. Corollary discharge circuits in the primate brain. *Curr. Opin. Neurobiol.* **18**, 552–557 (2008).

18. Ali, M. A., Lischka, K., Preuss, S. J., Trivedi, C. A. & Bollmann, J. H. A synaptic corollary discharge signal suppresses midbrain visual processing during saccade-like locomotion. *Nat. Commun.* **14**, 7592 (2023).

19. Wurtz, R. H. Corollary Discharge Contributions to Perceptual Continuity Across Saccades. *Annu. Rev. Vis. Sci.* **4**, 215–237 (2018).

20. Wachowiak, M. All in a Sniff: Olfaction as a Model for Active Sensing. *Neuron* **71**, 962–973 (2011).

21. Hoffman, K. L. *et al.* Saccades during visual exploration align hippocampal 3–8 Hz rhythms in human and non-human primates. *Front. Syst. Neurosci.* **7**, (2013).

22. Leszczynski, M. *et al.* Saccadic modulation of neural excitability in auditory areas of the neocortex. *Curr. Biol.* **33**, 1185-1195.e6 (2023).

23. Renninger, L. W., Verghese, P. & Coughlan, J. Where to look next? Eye movements reduce local uncertainty. *J. Vis.* **7**, 6 (2007).

24. Gallego-Carracedo, C., Perich, M. G., Chowdhury, R. H., Miller, L. E. & Gallego, J. Á. Local field potentials reflect cortical population dynamics in a region-specific and frequency-dependent manner. *eLife* **11**, e73155 (2022).

25. Hughes, A. M., Whitten, T. A., Caplan, J. B. & Dickson, C. T. BOSC: a better oscillation detection method, extracts both sustained and transient rhythms from rat hippocampal recordings. *Hippocampus* **22**, 1417–1428 (2012).

26. Donoghue, T. *et al.* Parameterizing neural power spectra into periodic and aperiodic components. *Nat. Neurosci.* **23**, 1655–1665 (2020).

27. Schalk, G., McFarland, D. J., Hinterberger, T., Birbaumer, N. & Wolpaw, J. R. BCI2000: a general-purpose brain-computer interface (BCI) system. *IEEE Trans. Biomed. Eng.* **51**, 1034–1043 (2004).

28. Molnar, C. *Interpretable Machine Learning: A Guide For Making Black Box Models Explainable*. (Christoph Molnar).

29. Pannasch, S., Helmert, J. R., Roth, K., Herbold, A.-K. & Walter, H. Visual Fixation Durations and Saccade Amplitudes: Shifting Relationship in a Variety of Conditions. *J. Eye Mov. Res.* **2**, (2008).

30. Nourmohammadi, A. *et al.* Passive functional mapping of receptive language cortex during general anesthesia using electrocorticography. *Clin. Neurophysiol.* **147**, 31–44 (2023).

31. Parvizi, J. & Kastner, S. Promises and limitations of human intracranial electroencephalography. *Nat. Neurosci.* **21**, 474–483 (2018).

32. Pan, Y., Popov, T., Frisson, S. & Jensen, O. Saccades are locked to the phase of alpha oscillations during natural reading. *PLOS Biol.* **21**, e3001968 (2023).

33. Leszczynski, M. & Schroeder, C. E. The Role of Neuronal Oscillations in Visual Active Sensing. *Front. Integr. Neurosci.* **13**, 32 (2019).

34. Jutras, M. J. & Buffalo, E. A. Synchronous Neural Activity and Memory Formation. *Curr. Opin. Neurobiol.* **20**, 150–155 (2010).

35. Breiman, L. Random Forests. *Mach. Learn.* **45**, 5–32 (2001).

36. Terlau, J. *et al.* Conjunctive population coding integrates sensory evidence to guide adaptive behavior. *Proc. Natl. Acad. Sci.* **122**, e2520444122 (2025).

37. Kuhn, H. W. Classics in Game Theory. 1–328 (2020).

38. Verhagen, J. V., Wesson, D. W., Netoff, T. I., White, J. A. & Wachowiak, M. Sniffing controls an adaptive filter of sensory input to the olfactory bulb. *Nat. Neurosci.* **10**, 631–639 (2007).

39. Barczak, A. *et al.* Dynamic Modulation of Cortical Excitability during Visual Active Sensing. *Cell Rep.* **27**, 3447-3459.e3 (2019).

40. Lahner, B., Mohsenzadeh, Y., Mullin, C. & Oliva, A. Visual perception of highly memorable images is mediated by a distributed network of ventral visual regions that enable a late memorability response. *PLOS Biol.* **22**, e3002564 (2024).

41. Wang, Y., Cao, R. & Wang, S. Encoding of Visual Objects in the Human Medial Temporal Lobe. *J. Neurosci.* **44**, (2024).

42. Doucet, G., Gulli, R. A., Corrigan, B. W., Duong, L. R. & Martinez-Trujillo, J. C. Modulation of local field potentials and neuronal activity in primate hippocampus during saccades. *Hippocampus* **30**, 192–209 (2020).

43. Sander, V., Soper, B. & Everling, S. Nonhuman primate event-related potentials associated with pro- and anti-saccades. *NeuroImage* **49**, 1650–1658 (2010).

44. Staudigl, T., Minxha, J., Mamelak, A. N., Gothard, K. M. & Rutishauser, U. Saccade-related neural communication in the human medial temporal lobe is modulated by the social relevance of stimuli. *Sci. Adv.* **8**, eabl6037.

45. Staudigl, T., Hartl, E., Noachtar, S., Doeller, C. F. & Jensen, O. Saccades are phase-locked to alpha oscillations in the occipital and medial temporal lobe during successful memory encoding. *PLOS Biol.* **15**, e2003404 (2017).

46. Bremmer, F., Kubischik, M., Hoffmann, K.-P. & Krekelberg, B. Neural Dynamics of Saccadic Suppression. *J. Neurosci.* **29**, 12374–12383 (2009).

47. Golan, T. *et al.* Increasing suppression of saccade-related transients along the human visual hierarchy. *eLife* **6**, e27819 (2017).

48. Leszczynski, M. *et al.* Neural activity in the human anterior thalamus during natural vision. *Sci. Rep.* **11**, 17480 (2021).

49. Martin, C. B. & Barense, M. D. Perception and Memory in the Ventral Visual Stream and Medial Temporal Lobe. *Annu. Rev. Vis. Sci.* **9**, 409–434 (2023).

50. Rosen, M. C. & Freedman, D. J. How distributed is the brain-wide network that is recruited for cognition? *Nat. Rev. Neurosci.* **27**, 138–150 (2026).

51. Benigno, G. B., Budzinski, R. C., Davis, Z. W., Reynolds, J. H. & Muller, L. Waves traveling over a map of visual space can ignite short-term predictions of sensory input. *Nat. Commun.* **14**, 3409 (2023).

52. DiCarlo, J. J., Zoccolan, D. & Rust, N. C. How Does the Brain Solve Visual Object Recognition? *Neuron* **73**, 415–434 (2012).

53. Prabhakaran, V., Narayanan, K., Zhao, Z. & Gabrieli, J. D. E. Integration of diverse information in working memory within the frontal lobe. *Nat. Neurosci.* **3**, 85–90 (2000).

54. Yang, S. C.-H., Lengyel, M. & Wolpert, D. M. Active sensing in the categorization of visual patterns. *eLife* **5**, e12215.

55. Lee, D. & Malpeli, J. G. Effects of saccades on the activity of neurons in the cat lateral geniculate nucleus. *J. Neurophysiol.* **79**, 922–936 (1998).

56. He, B. J. Scale-free brain activity: past, present, and future. *Trends Cogn. Sci.* **18**, 480–487 (2014).

57. Purpura, K. P., Kalik, S. F. & Schiff, N. D. Analysis of Perisaccadic Field Potentials in the Occipitotemporal Pathway During Active Vision. *J. Neurophysiol.* **90**, 3455–3478 (2003).

58. Kang, I., Talluri, B. C., Yates, J. L., Niell, C. M. & Nienborg, H. Is the impact of spontaneous movements on early visual cortex species specific? *Trends Neurosci.* **48**, 7–21 (2025).

59. Buzsáki, G., Anastassiou, C. A. & Koch, C. The origin of extracellular fields and currents-EEG, ECoG, LFP and spikes. *Nat. Rev. Neurosci.* **13**, 407–420 (2012).

60. Zacksenhouse, M. & Ahissar, E. Temporal Decoding by Phase-Locked Loops: Unique Features of Circuit-Level Implementations and Their Significance for Vibrissal Information Processing. *Neural Comput.* **18**, 1611–1636 (2006).

61. Koay, S. A., Charles, A. S., Thiberge, S. Y., Brody, C. D. & Tank, D. W. Sequential and efficient neural-population coding of complex task information. *Neuron* **110**, 328-349.e11 (2022).

62. Williams, C. C. Not all visual memories are created equal. *Vis. Cogn.* **18**, 201–228 (2010).

63. Sapountzis, P., Paneri, S. & Gregoriou, G. G. Distinct roles of prefrontal and parietal areas in the encoding of attentional priority. *Proc. Natl. Acad. Sci. U. S. A.* **115**, E8755–E8764 (2018).

64. Vries, I. E. J. de, Slagter, H. A. & Olivers, C. N. L. Oscillatory Control over Representational States in Working Memory. *Trends Cogn. Sci.* **24**, 150–162 (2020).

65. Backus, A. R., Schoffelen, J.-M., Szebényi, S., Hanslmayr, S. & Doeller, C. F. Hippocampal-Prefrontal Theta Oscillations Support Memory Integration. *Curr. Biol.* **26**, 450–457 (2016).

66. Zheng, J. *et al.* Theta phase precession supports memory formation and retrieval of naturalistic experience in humans. *Nat. Hum. Behav.* **8**, 2423–2436 (2024).

67. Yan, Y., Zhaoping, L. & Li, W. Bottom-up saliency and top-down learning in the primary visual cortex of monkeys. *Proc. Natl. Acad. Sci.* **115**, 10499–10504 (2018).

68. Barron, H. C., Auksztulewicz, R. & Friston, K. Prediction and memory: A predictive coding account. *Prog. Neurobiol.* **192**, 101821 (2020).

69. Inman, C. S. *et al.* Direct electrical stimulation of the amygdala enhances declarative memory in humans. *Proc. Natl. Acad. Sci. U. S. A.* **115**, 98–103 (2018).

70. Schapiro, A. C. *et al.* The hippocampus is necessary for the consolidation of a task that does not require the hippocampus for initial learning. *Hippocampus* **29**, 1091–1100 (2019).

71. Zhou, B., Lapedriza, A., Khosla, A., Oliva, A. & Torralba, A. Places: A 10 Million Image Database for Scene Recognition. *IEEE Trans. Pattern Anal. Mach. Intell.* **40**, 1452–1464 (2018).

72. Stark, S. M., Stevenson, R., Wu, C., Rutledge, S. & Stark, C. E. L. Stability of age-related deficits in the mnemonic similarity task across task variations. *Behav. Neurosci.* **129**, 257–268 (2015).

73. Desikan, R. S. *et al.* An automated labeling system for subdividing the human cerebral cortex on MRI scans into gyral based regions of interest. *NeuroImage* **31**, 968–980 (2006).

74. Kural, M. A. *et al.* Criteria for defining interictal epileptiform discharges in EEG. *Neurology* **94**, e2139–e2147 (2020).

75. König, S. D. & Buffalo, E. A. A nonparametric method for detecting fixations and saccades using cluster analysis: Removing the need for arbitrary thresholds. *J. Neurosci. Methods* **227**, 121–131 (2014).

76. Chawla, N. V., Bowyer, K. W., Hall, L. O. & Kegelmeyer, W. P. SMOTE: Synthetic Minority Over-sampling Technique. *J. Artif. Intell. Res.* **16**, 321–357 (2002).

Supplementary materials

Supplementary Table 1 Data Summary

ID	Experiment duration (day)	Number of study session	Number of test session	Total number of valid visual encoding trials *	Total number of valid saccades
1	4	4	4	184	1010
2	4	8	8	187	1112
3	2	4	4	91	431
4	4	8	8	196	1447
5	6	12	12	263	1561
6	2	4	4	69	392
7	2	4	4	80	1063
8	2	4	4	30	292

*The criteria for a valid visual encoding trial include 1. Based on the eye-tracking data, subjects maintained their gaze on the monitor for more than half the duration of each trial; 2. No brain stimulation was delivered during this trial.

Supplementary Table 2 Patient Characteristics

ID	Epilepsy diagnosis	Sex	Age	Handedness	WAIS
1	Focal epilepsy with seizure onset in the left hippocampus	F	36–40	N/A	90
2	Multifocal mesial temporal lobe epilepsy	F	36–40	N/A	N/A
3	Multifocal epilepsy with seizure onset in the hippocampus	F	41–45	R	N/A
4	Focal left hippocampal epilepsy	M	36–40	R	98
5	Focal right hippocampal epilepsy	M	36–40	R	76
6	Focal epilepsy in left supplementary motor area	F	36–40	R	N/A
7	No spontaneous seizures recorded	F	31–35	R	107
8	Focal epilepsy with seizure onset in the right hippocampus and amygdala	F	22–25	R	88

N/A: not available. In the Sex column, ‘F’ stands for ‘female’ and ‘M’ stands for ‘male’. In the Handedness column, ‘L’ stands for ’left’ and ‘R’ stands for ‘right’. WAIS: Wechsler Adult Intelligence Scale.

Supplementary Table 3 Visual encoding behavioral results

		The number of				The number of				
ID	Task ID	Visual encoding trial	Tested visual encoding trial	Remembered tested visual encoding trials	Correct recall rate (%)	Test trials	Novel test trials	Correct recognition of novel test trials	Correct recognition rate of novel test trials	Overall correct recognition rate
	All trials									
1	Encoding1	180	160	110	69%	240	80	47	59%	65%
1	Encoding2	180	160	155	97%	240	80	5	6%	67%
2	Encoding1	180	160	83	52%	240	80	72	90%	65%
2	Encoding2	180	160	126	79%	240	80	54	68%	75%

3	Encoding1	180	160	132	83%	240	80	51	64%	76%
4	Encoding1	180	160	121	76%	240	80	68	85%	79%
4	Encoding2	180	160	99	62%	240	80	64	80%	68%
5	Encoding1	180	160	131	82%	240	80	59	74%	79%
5	Encoding2	180	159	140	88%	240	81	42	52%	76%
5	Encoding3	180	160	148	93%	240	80	38	48%	78%
6	Encoding1	160	80	38	48%	160	80	56	70%	59%
7	Encoding1	160	80	71	89%	160	80	65	81%	85%
8	Encoding1	160	80	47	59%	160	80	57	71%	65%
Valid trials only*										
1	Encoding1	91	73	50	68.5%	-	-	-	-	-
1	Encoding2	93	77	74	96.1%	-	-	-	-	-
2	Encoding1	95	77	36	46.8%	-	-	-	-	-
2	Encoding2	92	74	61	82.4%	-	-	-	-	-
3	Encoding1	91	77	64	83.1%	-	-	-	-	-
4	Encoding1	97	80	62	77.5%	-	-	-	-	-
4	Encoding2	99	79	50	63.3%	-	-	-	-	-
5	Encoding1	98	79	62	78.5%	-	-	-	-	-
5	Encoding2	78	67	58	86.6%	-	-	-	-	-
5	Encoding3	87	75	69	92.0%	-	-	-	-	-
6	Encoding1	69	35	14	40.0%	-	-	-	-	-
7	Encoding1	80	40	35	87.5%	-	-	-	-	-
8	Encoding1	30	18	12	66.7%	-	-	-	-	-

Correct recall rate represents the percentage of remembered visual encoding trials over the tested visual encoding trials. The overall correct recognition rate is calculated as the sum of true positives (old stimuli correctly recalled) and true negatives (new stimuli correctly rejected) divided by the

total number of test trials. *The criteria for a valid visual encoding trial include 1. Based on the eye-tracking data, subjects maintained their gaze on the monitor for more than half the duration of each trial; 2. No brain stimulation was delivered during this trial.

Supplementary Table 4 Electrode coverage

ID	Task ID	The total number of implanted electrode contacts	The number of bad contacts*	The number of valid contacts	Average number of valid contacts for each subject
1	Encoding1	225	4	221	220.5
	Encoding2	225	5	220	
2#	Encoding1	229	6	223	224.5
	Encoding2	229	3	226	
3#	Encoding1	170	4	166	166
4#	Encoding1	150	4	146	145.5
	Encoding2	150	5	145	
5#	Encoding1	214	3	211	210.3
	Encoding2	214	4	210	
	Encoding3	214	4	210	
6#	Encoding1	229	10	219	219
7#	Encoding1	190	2	188	188
8	Encoding1	222	3	219	219
Total					1592.8

*Electrodes exhibiting epileptiform activity or artifactual signals (e.g., due to poor contact) were excluded prior to re-referencing. # For a subset of subjects, 2 Ad-yech Behnke Fried Depth electrodes, each with 8-contact micro recording, were implanted. Data from micro wires were excluded if they displayed epileptiform activity or artifactual signals. The number of micro wires is not included in this table.

Appendix A Study protocol

The current study is part of the Amygdala Memory Enhancement trial (NCT05065450).

Electrode placement and patient monitoring

Electrodes are implanted stereotactically to help localize the seizure focus. As a standard means to increase accuracy, the surgery is guided by contrasted MR images, with post-operative reimaging for confirmation. The electrodes from various commercial vendors (Adtech, PMT, Dixi) have platinum contacts for recording intracranial electroencephalogram (iEEG) and for stimulation. An electrode may include macroelectrode contacts only or macro- and micro-electrode contacts. All electrodes are FDA-approved equipment for recording intracranial recording during presurgical evaluation.

Epilepsy monitoring unit (EMU) are wards that are designed for inpatient video EEG monitoring and are staffed by a multidisciplinary team of specialists, including attending physicians, fellows, psychiatrists, EEG technicians, nurses, and information-technology technicians. The EMU contains computers with monitors, one station per room, to visualize the real time recording of EEG and video data. The EMU continuously monitors the daily progress and health of each patient server for secure storage and access. The EMU rotates personnel to monitor and care for each patient daily (24 hours per day) during the patient's stay (on average 2 3 weeks) in the EMU. A patient under presurgical evaluation is discharged from the EMU at the discretion of the treating physicians.

All electrophysiological data will be collected through the EMU's clinical intracranial neural recording system and other devices that have been approved by the FDA to be sold for studies in human subjects or are commonly approved and used at other research institutions.

Reference

1. Sharot, T. & Yonelinas, A. P. Differential time-dependent effects of emotion on recollective experience and memory for contextual information. Cognition106, 538–547 (2008).

Figures for the manuscript titled “Mind’s eye: Saccade-related evoked potentials support visual encoding in humans”

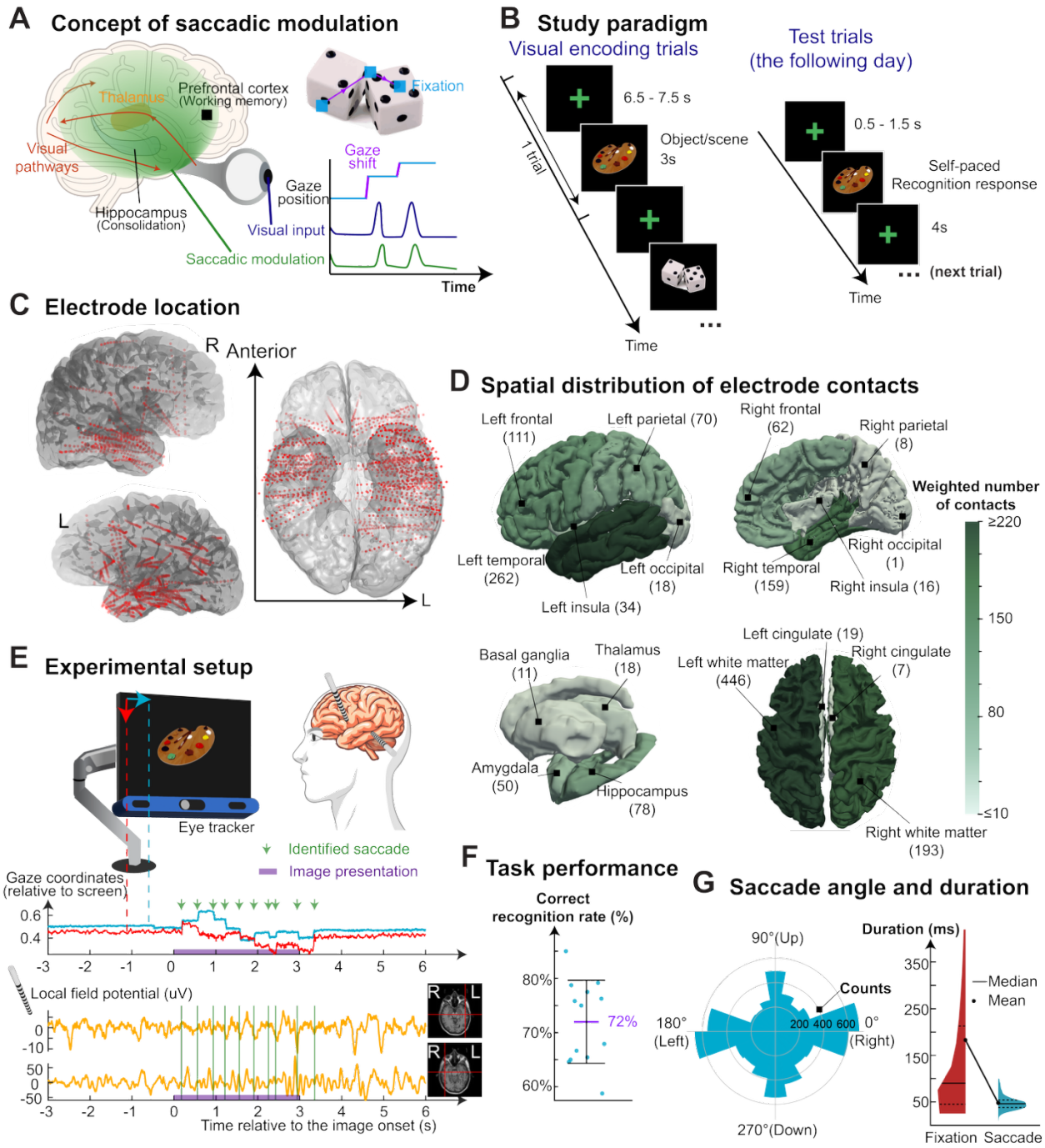

Figure 1. Experimental design for studying saccadic modulation in humans. (A) Concept of saccadic modulation. Neural processing of visual information peaks shortly after fixation onset, when visual acuity is at its maximum. Retinal inputs are transmitted

to the visual cortex via the lateral geniculate nucleus. Saccadic modulation refers to changes in neural activities related to eye movements. **(B)** Study paradigm. Subjects were asked to memorize a series of objects and scenes that were presented for 3 seconds each. Recognition memory was assessed the following day, where subjects used a keyboard to indicate whether they recognized the previously presented images among a series of old and new images. Examples of actual visual stimuli are shown in **Figure 1–Figure supplement 1G**. **(C)** Electrode location. We localized implanted stereoelectroencephalography (SEEG) electrodes in subject-specific anatomical space using post-implantation computed tomography (CT) imaging, co-registered to pre-implantation MRI. For visualization purposes, we transformed electrode coordinates into a common anatomical reference space obtained from a reference subject (Subject ID 1). **(D)** Regional distribution of electrode contacts. The common anatomical brain model is divided into four cortical areas (i.e., frontal, temporal, parietal, and occipital cortices), the insula and cingulate cortices, and four subcortical regions (i.e., amygdala, hippocampus, thalamus, and basal ganglia). Color represents the weighted number of electrode contacts per region. When electrode contacts (~2 mm^3 volume) overlapped voxels assigned to multiple brain regions, their contributions were proportionally allocated among these regions (see **Star Methods**). Left white matter has the greatest number of contacts (n = 446), followed by the left temporal lobe (n = 262). The sampling density, defined as the ratio of the number of electrode contacts per unit anatomical volume, was greatest in the amygdala (13 contacts/cm^3), followed by the hippocampus (7 contacts/cm^3), and the left temporal cortex (4 contacts/cm^3, **Figure 1 – Figure supplement 2A**). (**E)** Experimental setup. BCI2000 controlled stimulus presentation, recorded local field potentials from SEEG electrodes, and tracked eye movements. We identified saccades onset and offsets based on gaze coordinates using a clustering algorithm (see **Star Methods**). **(F)** Task performance. Each data point represents the recognition accuracy for one subject performing the visual encoding task described in panel **B**. All subjects confirmed that they performed the task as instructed during a post-experiment debriefing. The average overall correct recognition rate across tasks and subjects was 72%. (**G**) Distribution of saccade angle and direction.

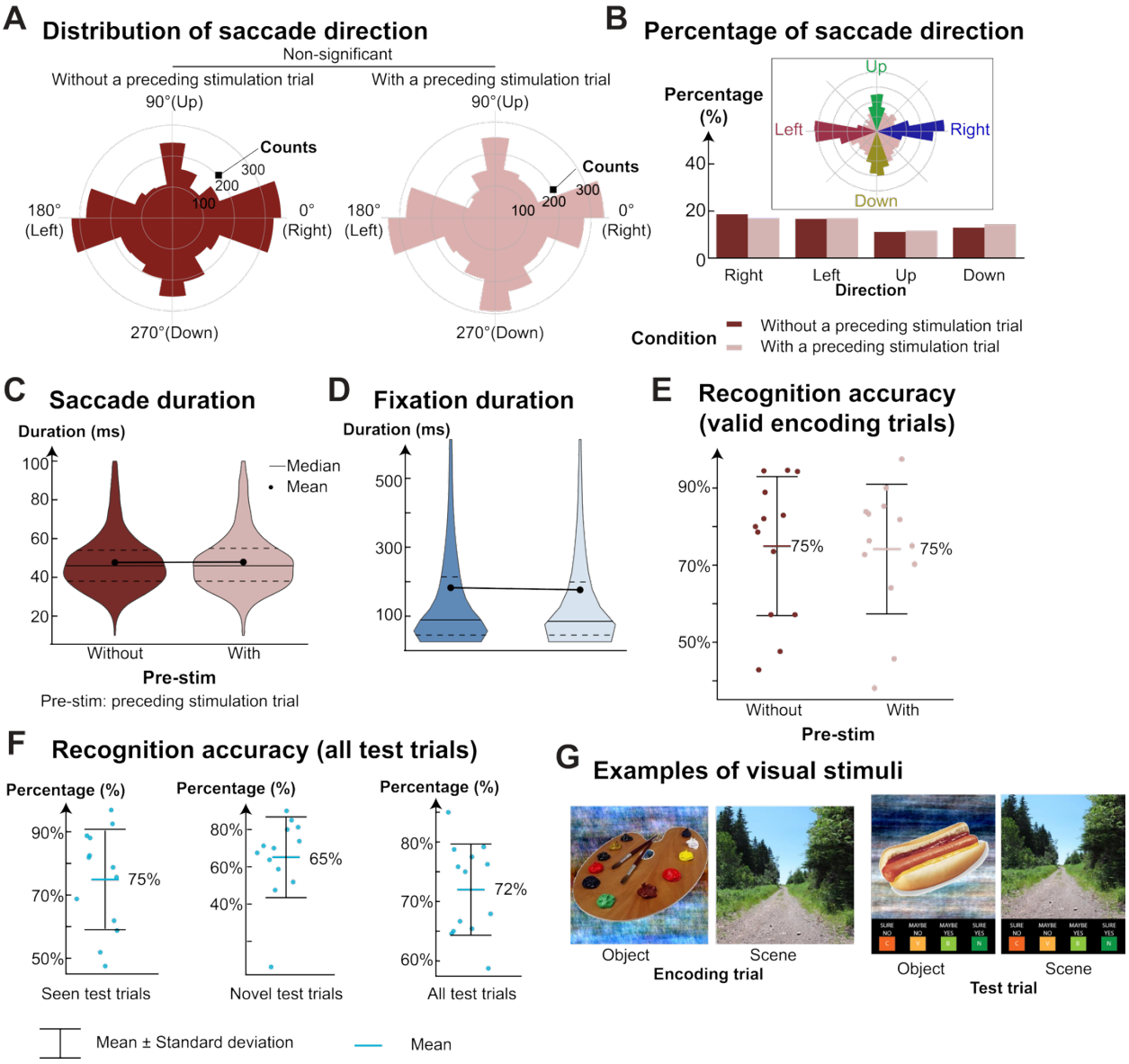

Figure 1 – Figure Supplement 1. Control analysis to rule out any latent effect of electrical stimulation on saccade behavior and recognition memory. This study is part of a clinical trial investigating the effects of electrical stimulation of the basolateral amygdala on visual memory encoding (NCT05065450). Cortical stimulation was administered during 50% of encoding trials. For this study, we excluded all stimulation trials. Comparison of saccade behavior and recognition memory performance for trials without and with a preceding stimulation trial did not show latent effects of electrical stimulation. **(A)** Distribution of saccade directions. We found no significant difference in saccade directions for trials without and with a preceding stimulation trial (Watson-Williams test, F-statistics (1, 7290) = 0.023, p = 0.879). **(B)** Percentage of saccades that are categorized as upward, downward, leftward, or rightward. The inset illustrates the definition of saccade direction: a saccade is classified as “rightward” if its angle lies within

±20° around the horizontal axis (0°). **(C–D)** Saccade and fixation duration for trials without and with a preceding stimulation trial. The effect size comparing durations between the two conditions was trivial (|Cohen's d| < 0.05). **(E)** Recognition accuracy for trials without and with a preceding stimulation trial (Cohen's d = -0.044). **(F)** Recognition accuracy for seen (e.g., old) test trials, novel test trials, and all test trials. **(G)** Examples of visual stimuli used in the encoding and test trials.

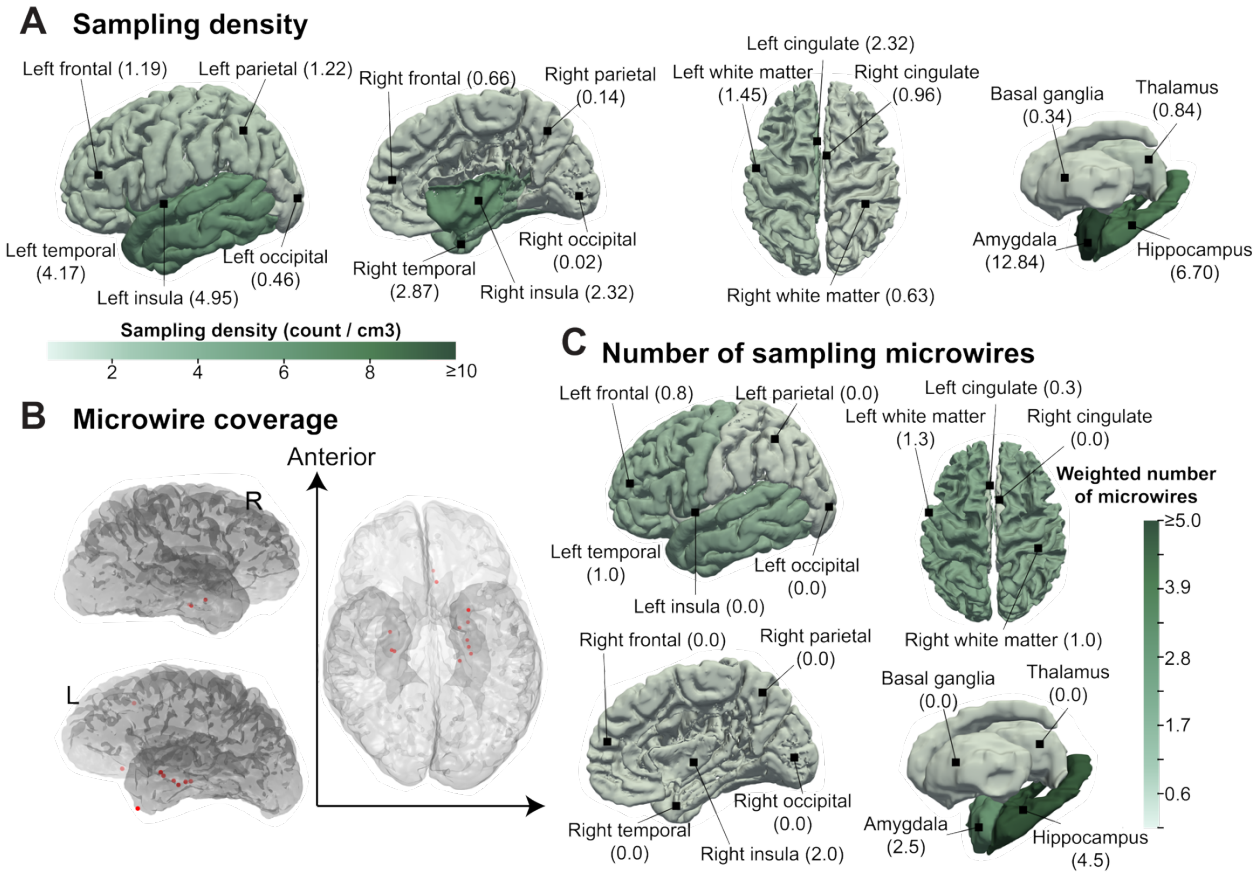

Figure 1 – Figure Supplement 2. Macro electrode sampling density and microwire locations. Six subjects were each implanted with two Ad-Tech Behnke-Fried depth electrodes, each containing eight macro contacts and eight microwires. We refer to the bundle of microwires emerging from the tip of each electrode as a micro-contact location. **(A)** Sampling density for macro-electrode contacts, calculated by dividing the weighted contact count within each brain region by the volume of that region. **(B)** Location of microwires on the brain model of a reference subject. **(C)** Number of microwires in major brain regions.

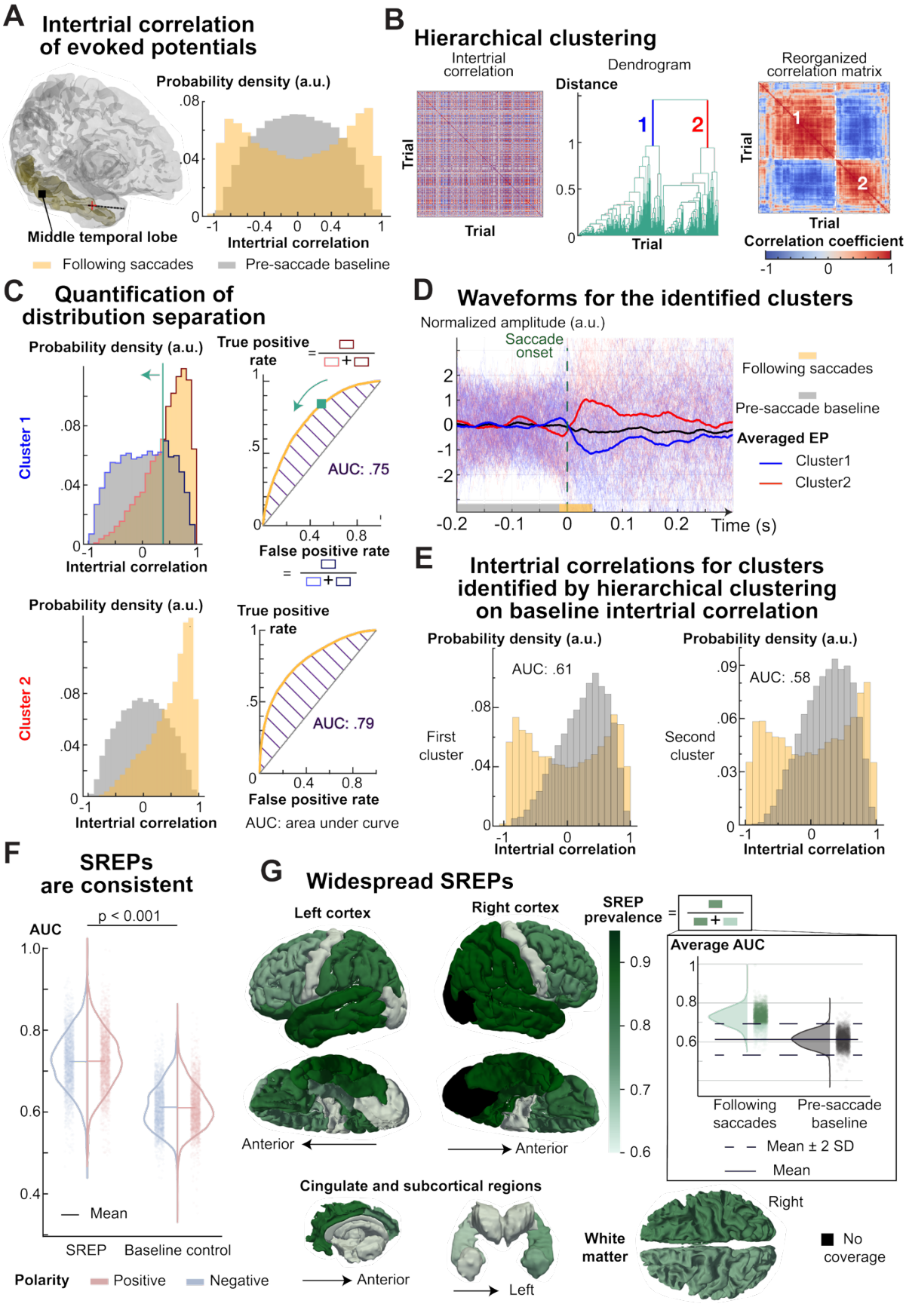
A
Intertrial correlation of evoked potentials
Probability density (a.u.)
Middle temporal lobe
Intertrial correlation
Following saccades
Pre-saccade baseline
B
Hierarchical clustering
Intertrial correlation
Dendrogram
Distance
Reorganized correlation matrix
Trial
Correlation coefficient
C
Quantification of distribution separation
Probability density (a.u.)
True positive rate
False positive rate
AUC: .75
Cluster 1
Cluster 2
AUC: .79
AUC: area under curve
D
Waveforms for the identified clusters
Normalized amplitude (a.u.)
Saccade onset
Following saccades
Pre-saccade baseline
Averaged EP
Cluster1
Cluster2
Time (s)
E
Intertrial correlations for clusters identified by hierarchical clustering on baseline intertrial correlation
AUC: .61
First cluster
AUC: .58
Second cluster
F
SREPs are consistent
AUC
p < 0.001
Mean
SREP
Baseline control
Polarity
Positive
Negative
G
Widespread SREPs
Left cortex
Right cortex
SREP prevalence
Average AUC
Following saccades
Pre-saccade baseline
Mean ± 2 SD
Mean
Anterior
Cingulate and subcortical regions
Left
White matter
Right
No coverage

Figure 2. Evoked potentials following saccades are consistent and widespread across the cerebrum. **(A)** Intertrial correlation of local field potentials (LFPs). To determine the presence of saccade-related evoked potentials (SREPs), we calculated the intertrial correlation of LFPs during the peri-saccadic and the baseline window (i.e., -10 ms to 40 ms, and -200 ms to -10 ms, relative to saccade onsets, respectively). Here, each trial is defined as an LFP segment centered on a saccade event. We calculated the intertrial correlation across all trial combinations using Pearson's correlation. The exemplar result for a representative electrode contact within the right middle temporal lobe shows an intertrial correlation distribution during the peri-saccadic period skewed toward the tails. In contrast, the corresponding baseline intertrial correlation appears normally distributed. **(B)** Hierarchical clustering. The bimodal nature of the peri-saccadic correlation distribution suggests the presence of two EP clusters, with trials within a cluster positively correlated and those between clusters negatively correlated. We used hierarchical clustering to identify these clusters. The dendrogram and the reordered intertrial correlation matrix confirm the presence of two distinct saccade-evoked potentials (shown in D). **(C)** Quantification of the separation between peri-saccadic and baseline correlation distributions. We used a sliding threshold to compute the receiver operator characteristic (ROC) curve. For a set of thresholds from -1 to 1, we calculated the true positive rate (fraction of peri-saccadic probability density above a threshold relative to the combined density) and false positive rate (fraction of peri-saccadic probability density below a threshold relative to the combined density) for each threshold. We used the area under the ROC curve (AUC) to measure separability. **(D)** Evoked potentials averaged across trials in clusters 1 and 2. To extract EP waveforms, we z-scored LFPs before hierarchical clustering. Each line represents the z-scored LFP of one trial. **(E)** Hierarchical clustering on baseline data. This procedure accounts for clustering-induced AUC inflation. **(F)** Peri-saccadic and baseline AUCs for intertrial correlations. AUC following saccades was significantly higher than baseline AUCs (Cohen's d = 1.857, two-tailed paired t-test, n = 2604, t statistic = 81.13, $p < 0.001$), indicating robust SREP. Each dot represents one electrode contact in one subject during one task. Colors denote the SREP polarity based on the sign of the first peak (details in **Figure 3**). **(G)** SREP prevalence across cerebrum. SREP prevalence is defined as the proportion of electrode contacts with AUC in the peri-saccadic condition above the mean + 2 standard deviation (SD) of baseline AUC. Color represents SREP prevalence. Electrode contacts are co-registered to a common reference brain model. The brain was segmented into White Matter (Left, Right), Hippocampus (Left, Right), Amygdala (Left, Right), Basal Ganglia, Thalamus, Orbitofrontal (Left, Right), Inferior Frontal (Left, Right), Middle Frontal (Left, Right), Superior Frontal (Left, Right), Anterior Cingulate, Posterior Cingulate, Motor (Left, Right), Anterior Temporal (Left, Right), Middle Temporal (Left, Right), Superior Temporal (Left, Right), Inferior Temporal (Left, Right), Medial Temporal (Left, Right), Fusiform (Left, Right), Parietal (Left, Right), Occipital (Left, Right), and Insula (Left, Right). We show robust

results of response ratio across cerebrum across various AUC thresholds used to define SREP prevalence in **Figure 2 – Figure supplement 1**, for example, mean + 3 SD of baseline AUC. We show the spatial distribution of intertrial consistency magnitude in **Figure 2 – Figure Supplement 2**. We show the electrode contact-level intertrial consistency magnitude in **Figure 2 – Figure Supplement 3**.

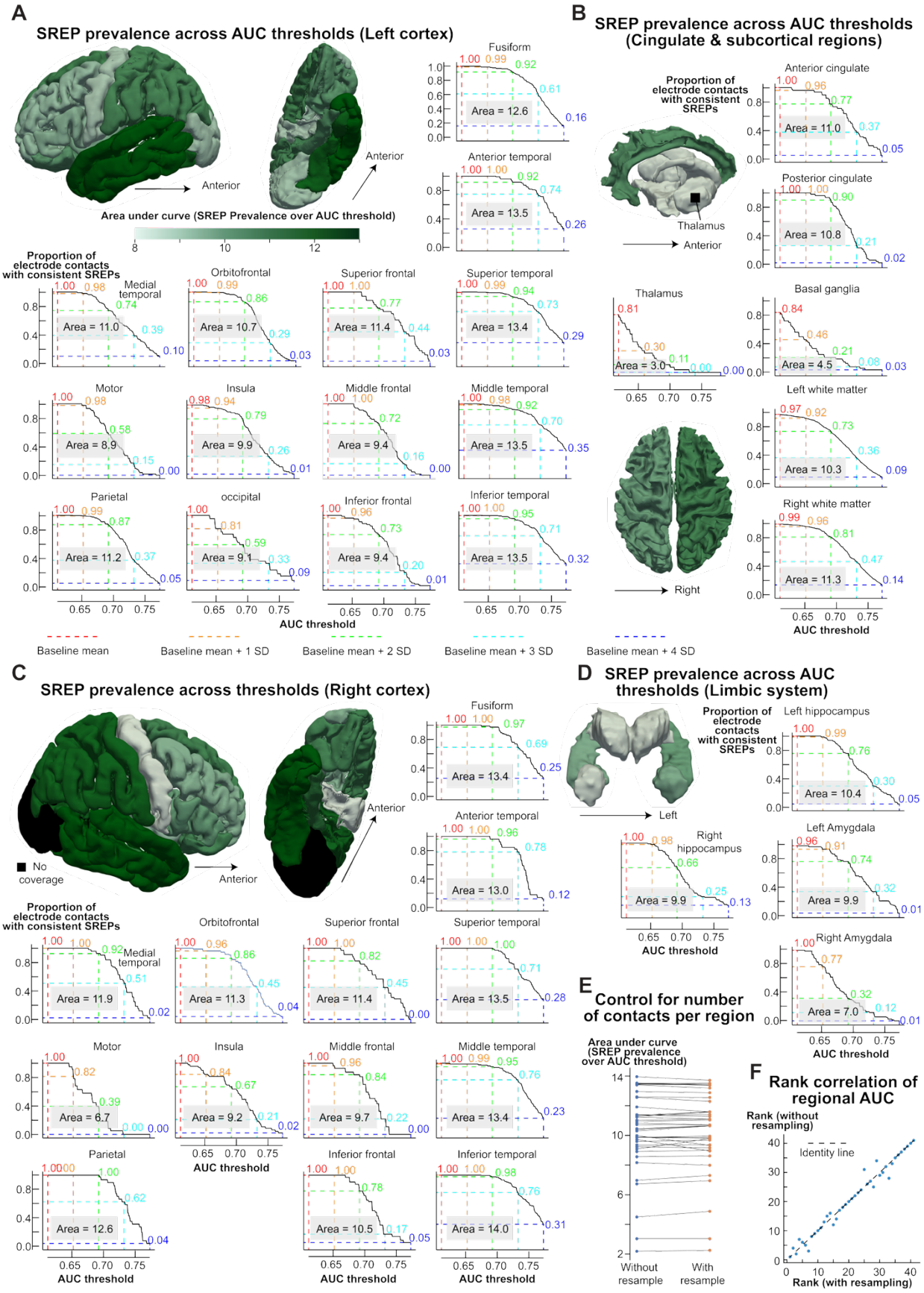
A
SREP prevalence across AUC thresholds (Left cortex)
Anterior
Anterior
Area under curve (SREP Prevalence over AUC threshold)
8
10
12
Proportion of electrode contacts with consistent SREPs
Fusiform
Area = 12.6
Anterior temporal
Area = 13.5
Medial temporal
Area = 11.0
Orbitofrontal
Area = 10.7
Superior frontal
Area = 11.4
Superior temporal
Area = 13.4
Motor
Area = 8.9
Insula
Area = 9.9
Middle frontal
Area = 9.4
Middle temporal
Area = 13.5
Parietal
Area = 11.2
occipital
Area = 9.1
Inferior frontal
Area = 9.4
Inferior temporal
Area = 13.5
AUC threshold
Baseline mean
Baseline mean + 1 SD
Baseline mean + 2 SD
Baseline mean + 3 SD
Baseline mean + 4 SD
B
SREP prevalence across AUC thresholds (Cingulate & subcortical regions)
Proportion of electrode contacts with consistent SREPs
Thalamus
Anterior
Anterior cingulate
Area = 11.0
Posterior cingulate
Area = 10.8
Thalamus
Area = 3.0
Basal ganglia
Area = 4.5
Left white matter
Area = 10.3
Right white matter
Area = 11.3
Right
AUC threshold
C
SREP prevalence across thresholds (Right cortex)
No coverage
Anterior
Anterior
Proportion of electrode contacts with consistent SREPs
Fusiform
Area = 13.4
Anterior temporal
Area = 13.0
Medial temporal
Area = 11.9
Orbitofrontal
Area = 11.3
Superior frontal
Area = 11.4
Superior temporal
Area = 13.5
Motor
Area = 6.7
Insula
Area = 9.2
Middle frontal
Area = 9.7
Middle temporal
Area = 13.4
Parietal
Area = 12.6
Inferior frontal
Area = 10.5
Inferior temporal
Area = 14.0
AUC threshold
D
SREP prevalence across AUC thresholds (Limbic system)
Left
Proportion of electrode contacts with consistent SREPs
Left hippocampus
Area = 10.4
Right hippocampus
Area = 9.9
Left Amygdala
Area = 9.9
Right Amygdala
Area = 7.0
AUC threshold
E
Control for number of contacts per region
Area under curve (SREP prevalence over AUC threshold)
Without resample
With resample
F
Rank correlation of regional AUC
Rank (without resampling)
Identity line
Rank (with resampling)

Figure 2 – Figure Supplement 1. **The percentage of electrodes showing consistent SREP across AUC thresholds**. **(A)** SREP consistency in the left cortex. Each panel shows the proportion of electrode contacts whose peri-saccadic AUC is over AUC thresholds. The color-coded dashed lines represent the reference thresholds: mean, mean + 1 standard deviation (SD), mean + 2 standard deviation (SD), mean + 3 standard deviation (SD), and mean + 4 standard deviation (SD) of baseline AUC. The color of the brain model reflects the area under the SREP-prevalence-over-AUC-threshold curve, representing the robustness of spatial distribution of SREP prevalence. **(B–D)** SREP consistency in the right cortex, subcortical regions, and cingulate cortex. **(E)** Areas under the curve of the SREP prevalence across the AUC thresholds. To control for the number of sampling electrodes in different regions, we resampled electrodes with replacement to equalize sample sizes across regions, then repeated the calculation of the area under the curve. Each dot represents the area under the curve for each region with or without resampling. **(F)** Correlation between AUCs derived from original and resampled data. The strong correlation revealed that the number of sampling electrodes has a trivial effect on the rank of SREP consistency (Spearman's $\rho = 0.987$, $p < 0.001$, $n = 37$, two-tailed t-test).

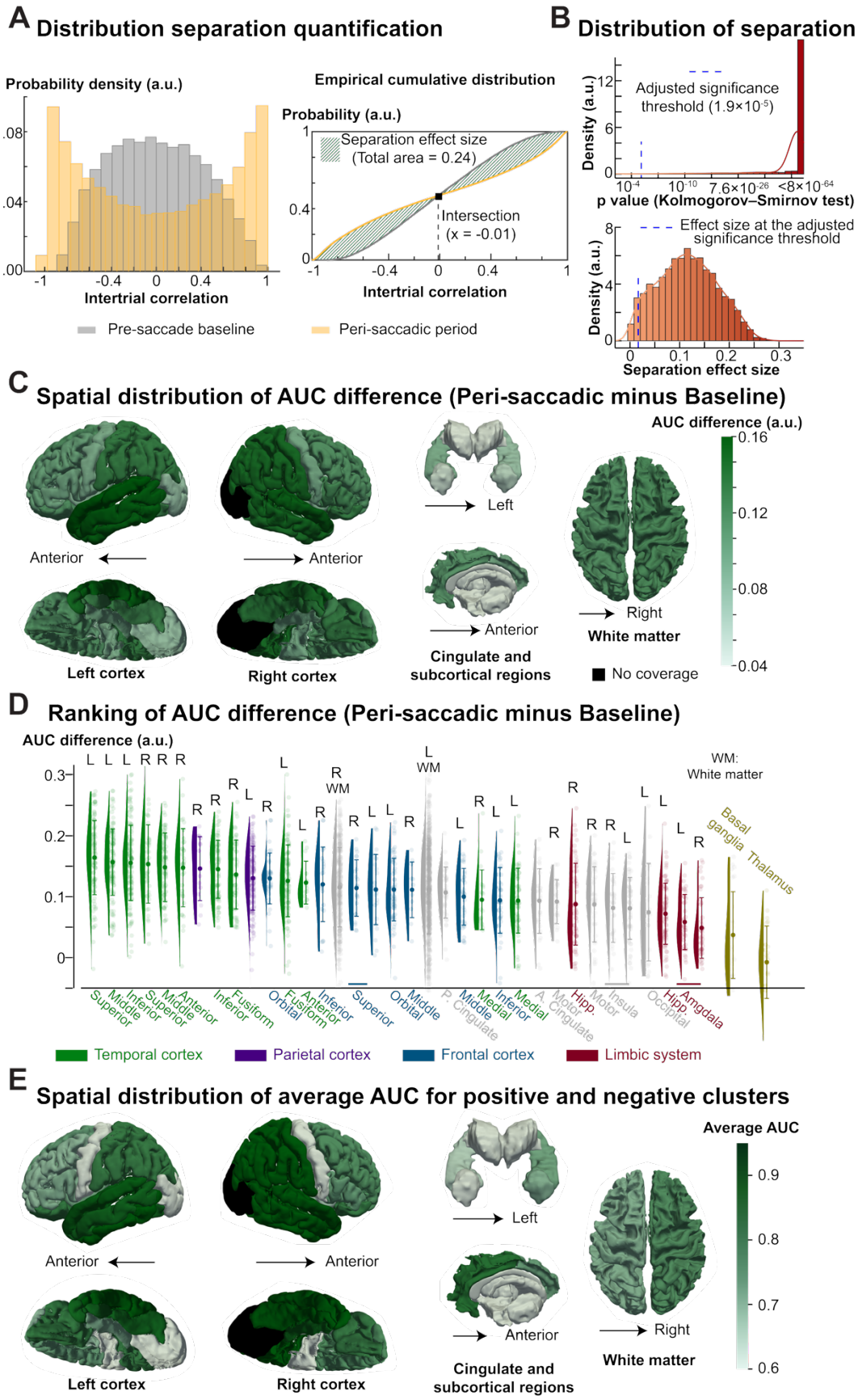
A Distribution separation quantification
Probability density (a.u.)
Intertrial correlation
Pre-saccade baseline
Empirical cumulative distribution
Probability (a.u.)
Separation effect size
(Total area = 0.24)
Intersection
(x = -0.01)
Intertrial correlation
Peri-saccadic period
B Distribution of separation
Adjusted significance threshold (1.9×10-5)
Density (a.u.)
p value (Kolmogorov–Smirnov test)
Effect size at the adjusted significance threshold
Separation effect size
C Spatial distribution of AUC difference (Peri-saccadic minus Baseline)
AUC difference (a.u.)
Anterior
Left
Right
Left cortex
Right cortex
Cingulate and subcortical regions
White matter
No coverage
D Ranking of AUC difference (Peri-saccadic minus Baseline)
AUC difference (a.u.)
WM: White matter
Temporal cortex
Parietal cortex
Frontal cortex
Limbic system
E Spatial distribution of average AUC for positive and negative clusters
Average AUC
Anterior
Left
Right
Left cortex
Right cortex
Cingulate and subcortical regions
White matter

Figure 2 – Figure Supplement 2. Quantifying the regional saccade-related EP consistency based on intertrial correlation distributions. **(A)** Quantification of the separation between intertrial correlation distributions during the baseline and peri-saccadic periods. To statistically assess the presence of robust and bimodal saccade-related EP, we quantified the separation (e.g., deviation from normal distribution toward bimodal distribution) between the intertrial correlation distributions during the peri-saccadic and baseline periods. Specifically, we computed the intersection point of their cumulative distributions and measured the absolute difference in area under the curve (AUC) between them. The striped region illustrates the absolute difference in AUC. **(B)** Distributions of p-value from Kolmogorov-Smirnov tests and the distribution of the separation effect size. The significance threshold was corrected for multiple comparisons. The blue dashed line marks the bimodal deviation corresponding to the significance threshold. The effect size corresponding to the adjusted significance threshold is 0.017. **(C)** The separation between the intertrial correlation distributions during the peri-saccadic and baseline periods across the cerebrum. The color reflects the difference in the area under the curve (computed separately for the two clusters and then averaged) of probability density over intertrial correlation (**Figure 2C**). **(D)** The ranking of the magnitude of SEP consistency (AUC difference). Colors indicate anatomical regions. L: Left; R: Right. **(E)** The magnitude of SREP consistency across anatomical regions. We quantified the magnitude of EP consistency as the average area under the probability density curve for intertrial correlation following saccades across polarity clusters.

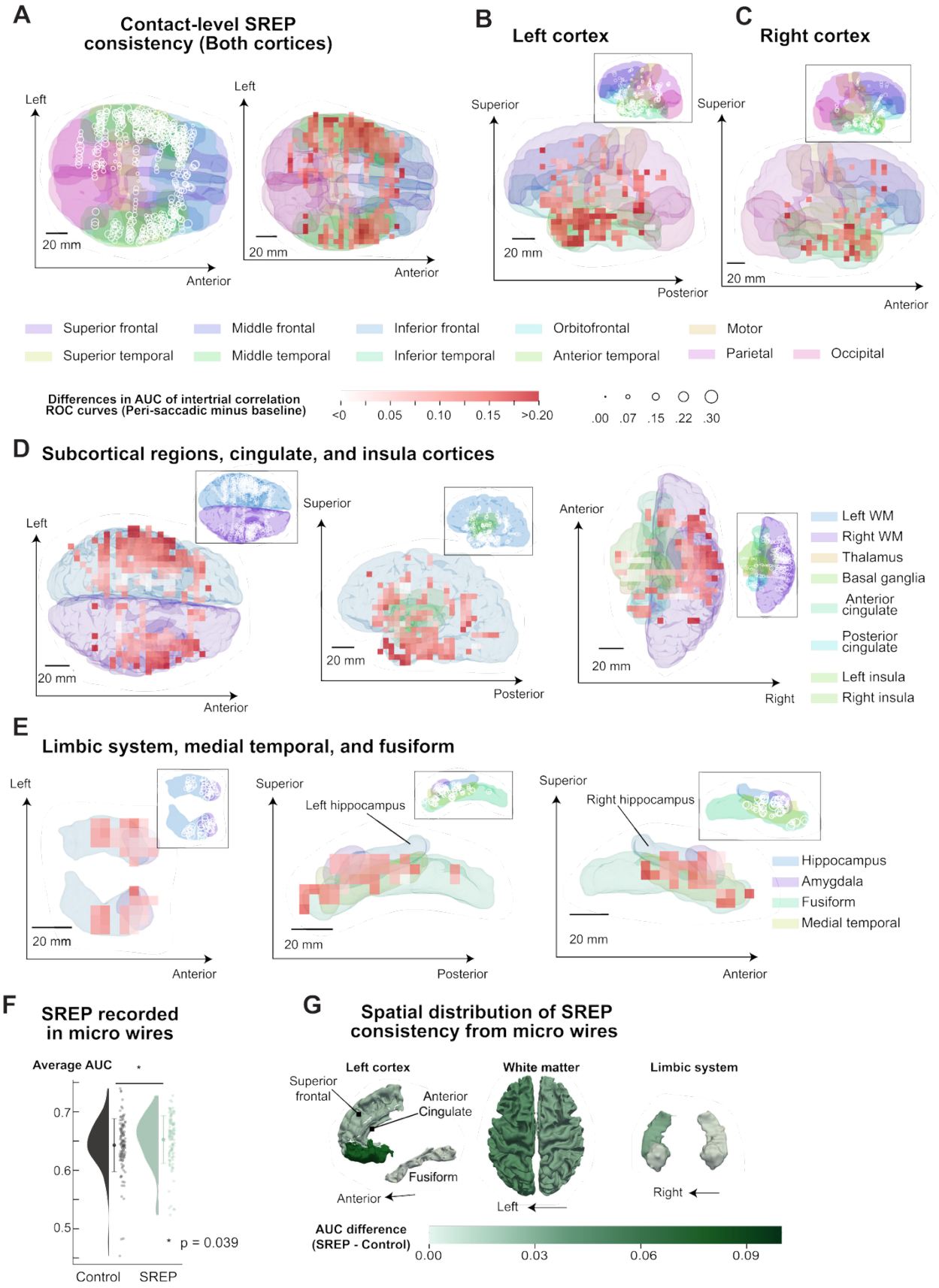
A
Contact-level SREP consistency (Both cortices)
Left
Left
20 mm
20 mm
Anterior
Anterior
B
Left cortex
Superior
20 mm
Posterior
C
Right cortex
Superior
20 mm
Anterior
Superior frontal
Middle frontal
Inferior frontal
Orbitofrontal
Motor
Superior temporal
Middle temporal
Inferior temporal
Anterior temporal
Parietal
Occipital
Differences in AUC of intertrial correlation ROC curves (Peri-saccadic minus baseline)
<0
0.05
0.10
0.15
>0.20
.00
.07
.15
.22
.30
D
Subcortical regions, cingulate, and insula cortices
Left
20 mm
Anterior
Superior
20 mm
Posterior
Anterior
20 mm
Right
Left WM
Right WM
Thalamus
Basal ganglia
Anterior cingulate
Posterior cingulate
Left insula
Right insula
E
Limbic system, medial temporal, and fusiform
Left
20 mm
Anterior
Superior
Left hippocampus
20 mm
Posterior
Superior
Right hippocampus
20 mm
Anterior
Hippocampus
Amygdala
Fusiform
Medial temporal
F
SREP recorded in micro wires
Average AUC
0.7
0.6
0.5
* p = 0.039
Control
SREP
G
Spatial distribution of SREP consistency from micro wires
Left cortex
Superior frontal
Anterior Cingulate
Fusiform
Anterior
White matter
Left
Limbic system
Right
AUC difference (SREP - Control)
0.00
0.03
0.06
0.09

Figure 2 – Figure Supplement 3. Electrode contact-level differences in the area under the curve (AUC) of intertrial correlation receiver operation characteristic (ROC) curves between baseline and peri-saccadic periods. For each electrode contact and each condition (baseline vs peri-saccade), AUCs were calculated separately for the two SREP clusters and then averaged. AUC difference between conditions, the degree of SREP consistency in anatomical regions sampled by each electrode. To visualize spatial patterns and enable comparison of effects across panels (devoid of a 3D perspective), we projected the 3D brain surface and electrode coordinates onto a 2D plane. The overlay heatmap represents the spatial pattern of SREP consistency. To generate the heatmap, we discretized this 2D space into a regular grid with a 5 mm resolution. We computed the local average AUC difference within a 10 mm radius for each grid element. Heatmap elements that have no nearby sampling electrodes are fully transparent. **(A–E)**. Spatial pattern of SREP consistency in cortices and subcortical regions. The heatmap color bar is uniform across panels A–E. **(F)** Consistency of peri-saccadic SREPs recorded from micro wires. We calculated the area under the receiver operator characteristic curve from intertrial correlation distributions. We averaged the area under the curve (AUC) for the two clusters. The average peri-saccadic AUCs were higher than the control AUCs (Cohen's $d = 0.227$, two-tailed paired t-test, $n = 115$, t statistic $= 2.088$, $p < 0.039$). **(G)** Spatial distribution of SREP consistency across the cerebrum. Brain regions located within 5 mm of the microwire electrodes are shown, which include Left Hippocampus, Left Amygdala, Left White Matter, Right Hippocampus, Right Amygdala, Right White Matter, Left Fusiform, Left Superior Frontal, and Anterior Cingulate.

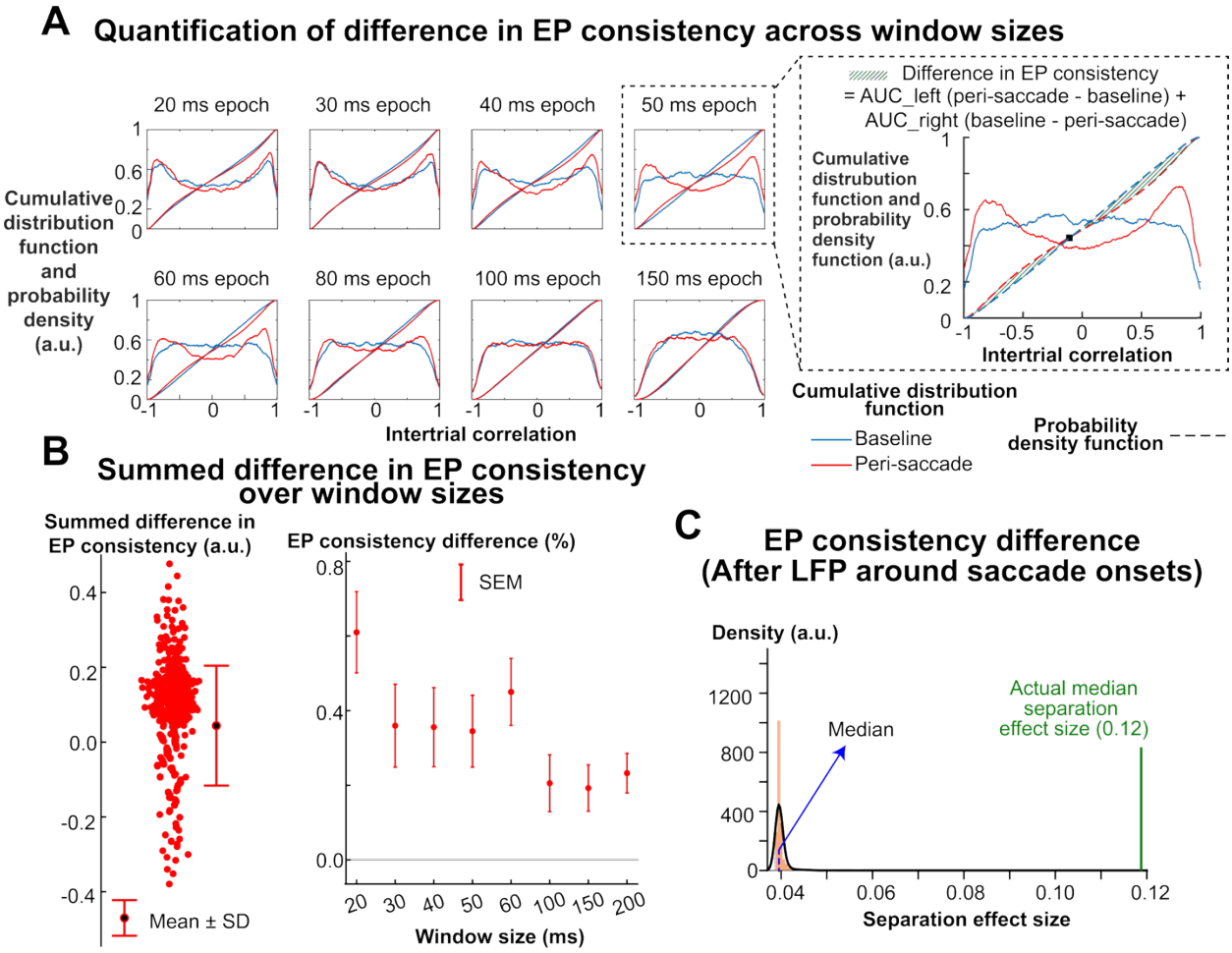

Figure 2 – Figure Supplement 4. **Evoked potential (EP) consistency across window size**. **(A)** Quantification of bimodality as a measure of EP consistency. To determine the time over which the EP waveform remains stable, we calculated the intertrial correlation distribution across a range of window sizes (20, 30, 40, 50, 60, 100, 150, 200 ms). We defined the baseline (i.e., pre-saccadic) epoch starting from 1s prior to saccade onset, with the same length as the peri-saccadic epoch. This panel shows cumulative distributions of intertrial correlation for an exemplary electrode (same electrode as shown in **Figure 2a**) across window sizes. As the window size increased, the degree of bimodality in the intertrial correlation distribution decreased. A more bimodal distribution of intertrial correlations, with values closer to 1 or -1, indicates greater EP consistency. To quantify EP consistency differences between baseline and peri-saccadic epochs, we computed the sum of two AUC differences: (1) For correlations smaller than the crossing point (black rectangle), we calculated $(peri - saccade\ AUC\ -\ pre - saccade\ AUC)$. 2. For correlations greater than the crossing point, we calculated $(pre - saccade\ AUC\ - peri - saccade\ AUC)$. **(B)** EP consistency differences summed across window sizes. Similar to our main analysis (**Figure 2G**), we defined electrode contacts showing consistent EPs following saccades as those whose mean AUC of intertrial correlation

following saccades exceeded the mean pre-saccade AUC by two standard deviations. For each such electrode contact, we computed EP consistency differences between baseline and peri-saccadic epochs, as illustrated in panel **A**, at each window size and summed these differences across window sizes. Across electrode contacts, the summed difference in EP consistency was significantly greater than 0 ($t = 5.349$, $p < 0.001$, Cohen's $d = 0.274$, $n = 382$, two-sided t-test). Across all window sizes, the peri-saccadic EPs consistently exhibited greater waveform consistency compared to the pre-saccadic baseline. **(C)** EP consistency difference following temporal shuffling of local field potentials. As a negative control, we disrupted the temporal structure by shuffling the local field potential data and repeated the analysis of the separation effect size, as defined in **Figure 2 – Figure Supplement 2a**. The median EP consistency difference between peri-saccadic and baseline EP was 0.04 in this negative control, significantly smaller than the observed separation effect size ($t = 65.086$, $p < 0.01$, Cohen's $d = 1.804$, two-sided t-test, $n = 2604$, compared to **Figure 2 – Figure Supplement 2B**), indicating our main findings remain robust.

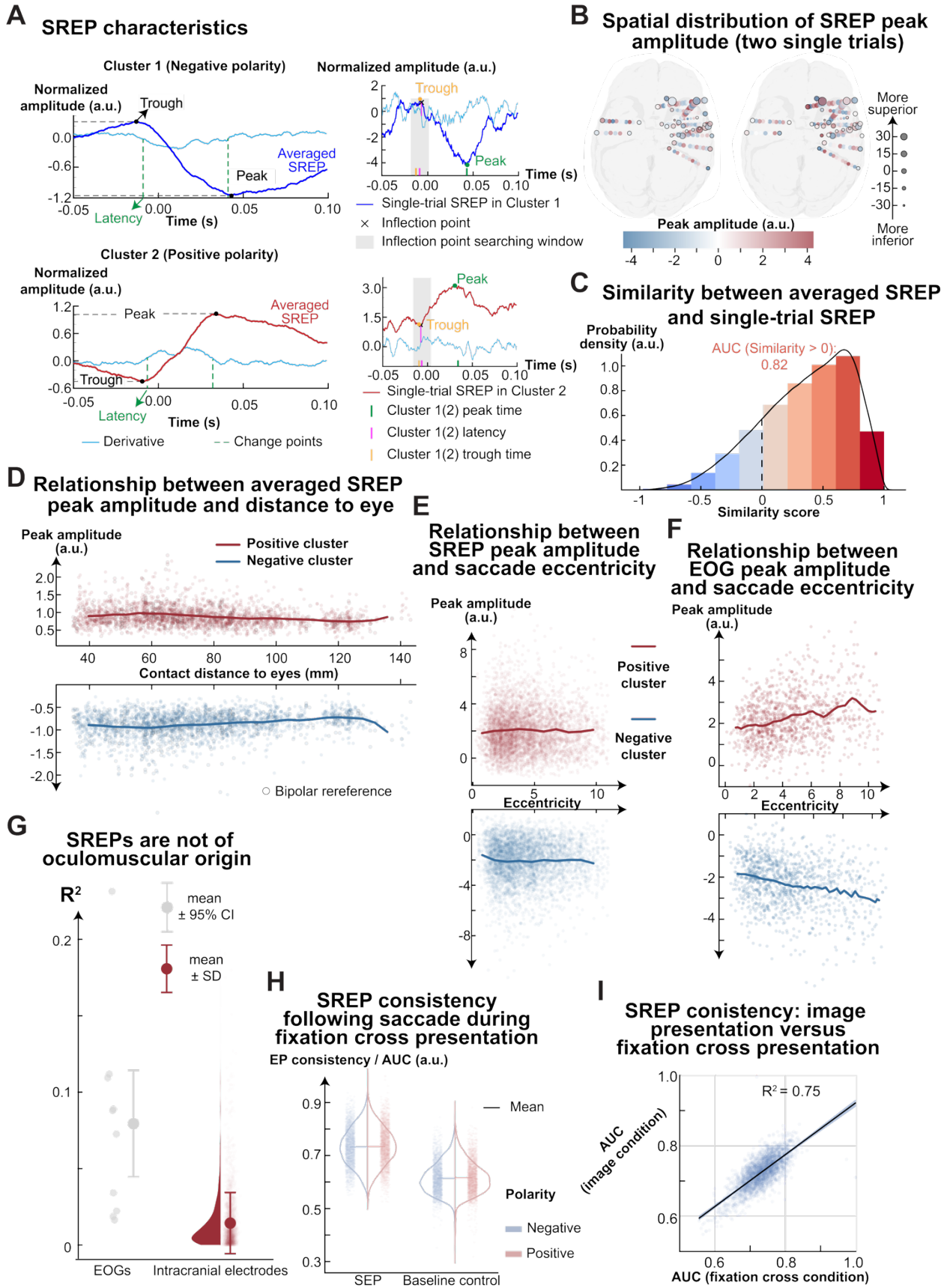
A
SREP characteristics
Cluster 1 (Negative polarity)
Normalized amplitude (a.u.)
Trough
Averaged SREP
Peak
Latency
Time (s)
Normalized amplitude (a.u.)
Trough
Peak
Time (s)
Single-trial SREP in Cluster 1
Inflection point
Inflection point searching window
Cluster 2 (Positive polarity)
Normalized amplitude (a.u.)
Peak
Averaged SREP
Trough
Latency
Time (s)
Derivative
Change points
Peak
Trough
Time (s)
Single-trial SREP in Cluster 2
Cluster 1(2) peak time
Cluster 1(2) latency
Cluster 1(2) trough time
B
Spatial distribution of SREP peak amplitude (two single trials)
More superior
More inferior
Peak amplitude (a.u.)
C
Similarity between averaged SREP and single-trial SREP
Probability density (a.u.)
AUC (Similarity > 0): 0.82
Similarity score
D
Relationship between averaged SREP peak amplitude and distance to eye
Peak amplitude (a.u.)
Positive cluster
Negative cluster
Contact distance to eyes (mm)
Bipolar rereference
E
Relationship between SREP peak amplitude and saccade eccentricity
Peak amplitude (a.u.)
Positive cluster
Negative cluster
Eccentricity
F
Relationship between EOG peak amplitude and saccade eccentricity
Peak amplitude (a.u.)
Eccentricity
G
SREPs are not of oculomuscular origin
R²
mean ± 95% CI
mean ± SD
EOGs
Intracranial electrodes
H
SREP consistency following saccade during fixation cross presentation
EP consistency / AUC (a.u.)
Mean
Polarity
Negative
Positive
SEP
Baseline control
I
SREP conistency: image presentation versus fixation cross presentation
R² = 0.75
AUC (image condition)
AUC (fixation cross condition)

Figure 3. **SREPs are not of oculomuscular origin**. **(A)** Characterization of averaged and single-trial SREPs. We characterized SREPs using latency, peak amplitude, trough amplitude, peak time, and trough time. After hierarchical clustering, we used MATLAB's *findchangepts* function to identify two inflection points in the derivative of SREPs averaged across trials within a cluster. We defined latency as the first point and peak time as the time point within a 10-ms window around the second inflection point at which the z-scored SREP amplitude was maximal for positive clusters (or minimal for negative clusters). Similarly, we defined trough time as the time point within a 10-ms window around latency at which the z-scored SREP amplitude is minimal for positive clusters (or maximal for negative clusters). We identified latency for single-trial SREP as the inflection point around the latency identified from the corresponding averaged SREP. We identified the peak and trough amplitudes for single-trial SREP by finding the maximum and minimum SREP amplitudes around the corresponding cluster-level peak and trough times. **(B)** Spatial distribution of SREP peak amplitudes following individual saccades. This panel shows SREP peak amplitudes across intracranial electrode contacts for two saccades in a subject (Subject ID 1). Circle size indicates electrode depth along the superior-to-inferior axis, with smaller circles representing deeper (i.e., more inferior) electrode contacts. We did not observe any spatial pattern in polarity or peak amplitude. **(C)** Similarity between single-trial SREPs and the corresponding cluster-level averaged SREPs, assessed using Spearman's correlation. Similarity distributions were skewed towards 1 (positive correlation), with an area under the curve of 0.812 for correlations greater than 0, compared to 0.181 for correlations less than 0, indicating that most single-trial SREPs resemble their cluster-level averaged SREP. **(D)** Relationship between averaged SREPs' peak amplitude and eyeball-to-electrode distance. The x-axis represents the distance from the recording electrode contact to the nearest eye. The line represents the average peak amplitude calculated within sliding windows of 10 mm, incremented by 5 mm steps. The distance explained 3.8% and 3.5% variance in peak amplitude of averaged SREPs for positive and negative clusters, respectively, across all electrode contacts. **(E)** Relationship between single-trial SREP amplitudes and saccade eccentricity. For both polarities, saccade eccentricity explained 0.0% variance in peak amplitude. Due to the large sample size, we show 2% of the data in the plot. **(F)** Relationship between single-trial oculomuscular signal peak amplitudes and saccade eccentricity. We derived oculomuscular signals (electrooculogram, EOG) extracted electrooculogram (EOG) signals from fronto-polar EEG scalp electrodes (Fp1 and Fp2) using bipolar re-referencing. Eccentricity explains 7.0% and 6.8% variance in oculomuscular signal peak amplitude for positive and negative clusters. We also explored potential relationship between SREP peak amplitude and other aspects of saccade kinetics, such as saccade duration. In our study, saccade duration positively correlated with saccade eccentricity but not with absolute peak amplitudes of the SREPs (**Figure 3 – Figure Supplement 1D**, Pearson correlation coefficient = 0.056, $p < 0.001$ between

saccade duration and saccade eccentricity, Pearson correlation coefficient = -0.002, p=0.080 between saccade duration and absolute peak amplitudes, permutation test). **(G)** Comparison of correlation coefficients between saccade eccentricity and single-trial SREP amplitudes for intracranial electrodes versus EOG. For each electrode contact, we calculated the correlation between eccentricity and single-trial SREP amplitudes for this contact. The mean correlation coefficient was 0.014 for intracranial electrodes and 0.079 for oculomuscular signals. Welch's t-test for comparison between unbalanced sample sizes showed that correlation coefficients for EOGs were significantly higher than intracranial local field potential signals (t = 3.154, p = 0.012, Cohen's d = 3.193, $n_{EOG} = 10$, $n_{EOG} = 2367$). For EOG correlation coefficients, the horizontal bars represent the bootstrapped 95% confidence interval (CI). **(H)** Consistency of SREP during fixation cross presentation, quantified using AUC as described in **Figure 2c**. During fixation cross presentation, SREP consistency was significantly higher than baseline (paired t-test, p<0.001, Cohen's d = 2.631, n = 2604). **(I)** Correlation between SREP consistency during image presentation and during fixation cross presentation. Electrode contacts with consistent SREPs during image presentation also exhibited consistent SREPs following saccades during fixation cross presentation.

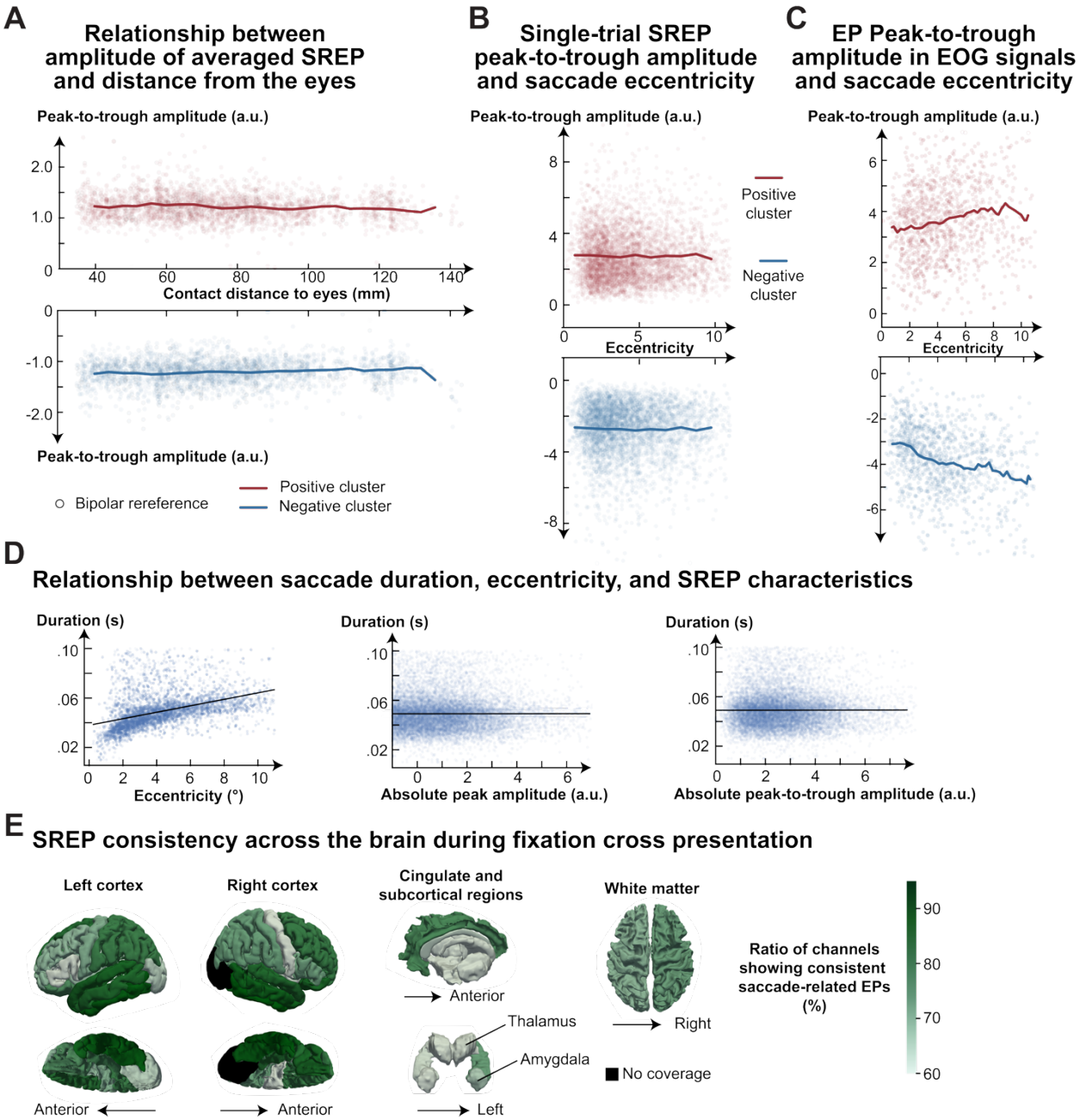

Figure 3 – Figure Supplement 1. SREPs are not oculomuscular signals. **(A)** Relationship between averaged SREPs' peak-to-trough amplitude and electrode-to-eye distance. The x-axis represents the distance from the recording electrode to the nearest eye. The line represents the average peak amplitude calculated within sliding windows of 10 mm, incremented by 5 mm steps. The distance explained 0.9% and 0.7% variance in peak to trough of averaged SREPs for positive and negative clusters, respectively, across all electrode contacts. **(B)** Relationship between single-trial SREP peak to trough and saccade eccentricity. For both polarities, saccade eccentricity explained 0.0% of the variance in peak-to-trough amplitude. **(C)** Relationship between single-trial

oculomuscular signal amplitudes and saccade eccentricity. We extracted electrooculogram (EOG) signals from fronto-polar EEG scalp electrodes (Fp1 and Fp2) using bipolar re-referencing. Eccentricity explains 2.7% and 8.2% variance in SREP peak-to-trough amplitude for positive and negative clusters. **(D)** Relationship between saccade duration and eccentricity, SREP peak amplitude, and SREP peak to trough. Saccade duration and saccade eccentricity were positively correlated ($Pearson's\ r = 0.056$), while saccade duration was correlated less with SREP peak amplitude ($Pearson's\ r = -0.002$), or SREP peak to trough ($Pearson's\ r = 0.004$). **(E)** Response ratios during fixation cross presentation across the cerebrum. The response ratio is defined as the proportion of electrode contacts with AUC in the peri-saccadic condition above the mean + 2 standard deviation (SD) of baseline AUC. The AUC calculation is illustrated in **Figure 2C–D**. The brain was segmented into White Matter (Left, Right), Hippocampus (Left, Right), Amygdala (Left, Right), Basal Ganglia, Thalamus, Orbitofrontal (Left, Right), Inferior Frontal (Left, Right), Middle Frontal (Left, Right), Superior Frontal (Left, Right), Anterior Cingulate, Posterior Cingulate, Motor (Left, Right), Anterior Temporal (Left, Right), Middle Temporal (Left, Right), Superior Temporal (Left, Right), Inferior Temporal (Left, Right), Medial Temporal (Left, Right), Fusiform (Left, Right), Parietal (Left, Right), Occipital (Left, Right), and Insula (Left, Right).

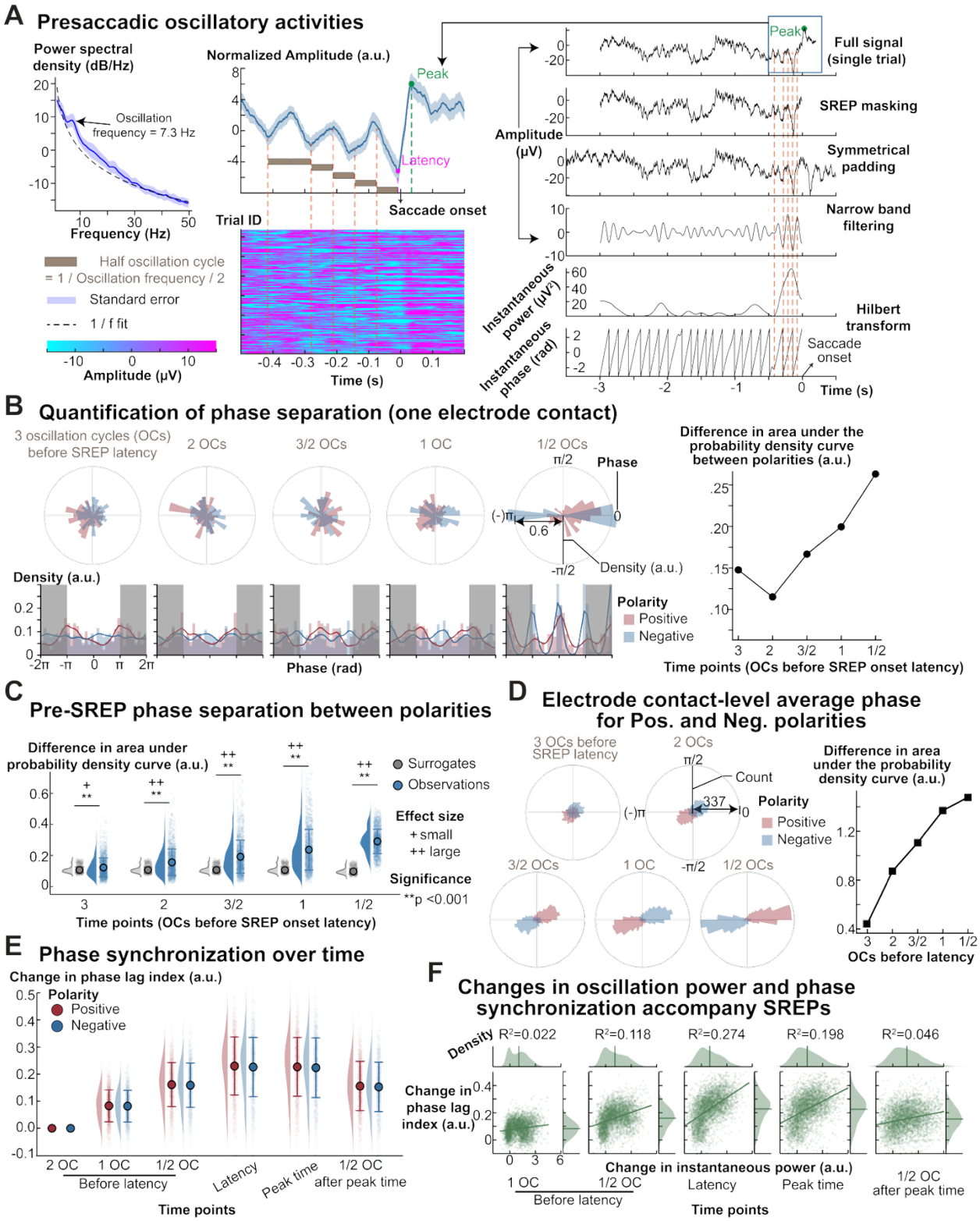

Figure 4. **Pre-saccadic oscillatory activity determines SREP polarities following saccades**. **(A)** Identification of oscillatory activities. To account for the aperiodic activity, we fitted a one-over-frequency ($1/f$) curve. We defined the oscillation frequency as the

frequency at which the residual of the power spectral density from the $1/f$ fit was largest. The middle panel shows the averaged SREP and single-trial SREP time-locked to saccade offset. Based on the identified SREP latency, we defined 5 time points of interest: 0.5, 1, 1.5, 2, and 3 oscillatory cycles (OCs) before latency. The heatmap shows the voltage signals from single trials. We estimated the instantaneous phase and power using the Hilbert transform, applied to padded, narrowband-passed signal segments preceding SREP latency (to avoid the potential influence of SREP in phase estimation). We only retained instantaneous power and phase corresponding to the masked, unpadded signal. **(B)** Pre-saccadic oscillation phase for the electrode contact shown in **A** and quantification of phase separation between SREPs of opposing polarities. The circular histograms show the distribution of phase for an electrode contact, colored by SREP polarity. To account for the circular nature of phase (i.e., -π is equal to π), we unwrapped phase values and extended the phase range from [$-\pi, \pi$] to [-2π, 2π]. We then estimated the probability density function and calculated the absolute difference in area under the probability density curve to quantify the phase separation between polarities. **(C)** Phase separation between polarities across electrode contacts. Each data point represents the difference in the area under the probability density function for one electrode contact. To assess whether the phases preceding SREP were different for positive and negative SREPs, we generated the surrogate (null) distribution by randomly permuting the polarity labels. The grey dots indicate the mean separation metric from the 50 permutations for each electrode contact. We used paired Wilcoxon signed rank test (two-sided, n = 1970 pairs per condition) to compare observed and null phase separation metrics across electrode contacts for each time point. All comparisons indicated statistically significant differences ($p < 0.001$). We quantified effect sizes using the rank biserial correlation, a non-parametric analog to Cohen's d that reflects the degree of separation between paired samples. Effect sizes increased progressively across conditions: from 0.204 in the earliest time point and 1.000 in the latest, suggesting strengthening of phase separation between polarities as time approached saccades. The rank-biserial correlation were 0.204, 0.581, 0.790, 0.901, 1.000 for the 5 time points. The data shown are from electrode contacts that exhibit both oscillatory activities and consistent SREP following saccades. We defined contacts exhibiting oscillatory activities as those in which the largest deviation between the power spectral density and the fitted 1/f aperiodic curve occurred at a frequency below 30 Hz. This criterion excludes broadband activity (the elbow in the PSD) or high-frequency artifacts, such as 60 Hz line noise, resulting in 1970 electrode contacts (see **Figure 4 – figure supplement 1d**). **(D)** Average phase across trials for positive and negative SREPs. The circular histogram shows the distribution of phase for the two polarities averaged across trials for each electrode contact. The right panel shows increased separation in the average phase between polarities as the time approaches SREP latency. **(E)** Phase synchronization induced by SREPs. To quantify phase coherence around saccades, we estimated instantaneous power and phase using unmasked signals, in contrast to panel

A. The effect size (Cohen's d) between phase lag index at 2 OC before latency and subsequent time points (from 1 OC before latency to 1 OC after peak time) were 1.214, 1.625, 1.739, 1.704, and 1.427. The corresponding rank-based effect sizes (rank-biserial correlation) were 0.924, 0.980, 0.988, 0.982, 0.959. Phase lag index significantly increased after 2 OC before latency ($p < 0.001$, Wilcoxon paired test, $n = 5300$). **(F)** Relationship between oscillation power and phase synchrony. Oscillation power, measured as instantaneous power began increasing from 2 OC before the SREP latency and remained elevated (see **Figure 4 – figure supplement 1f**). The positive correlation between instantaneous power and phase synchrony was strongest at the SREP latency and weaker at other time points. The density plot at the top and right represents the unimodal distribution of instantaneous power and instantaneous phase, where the means of these distributions are marked.

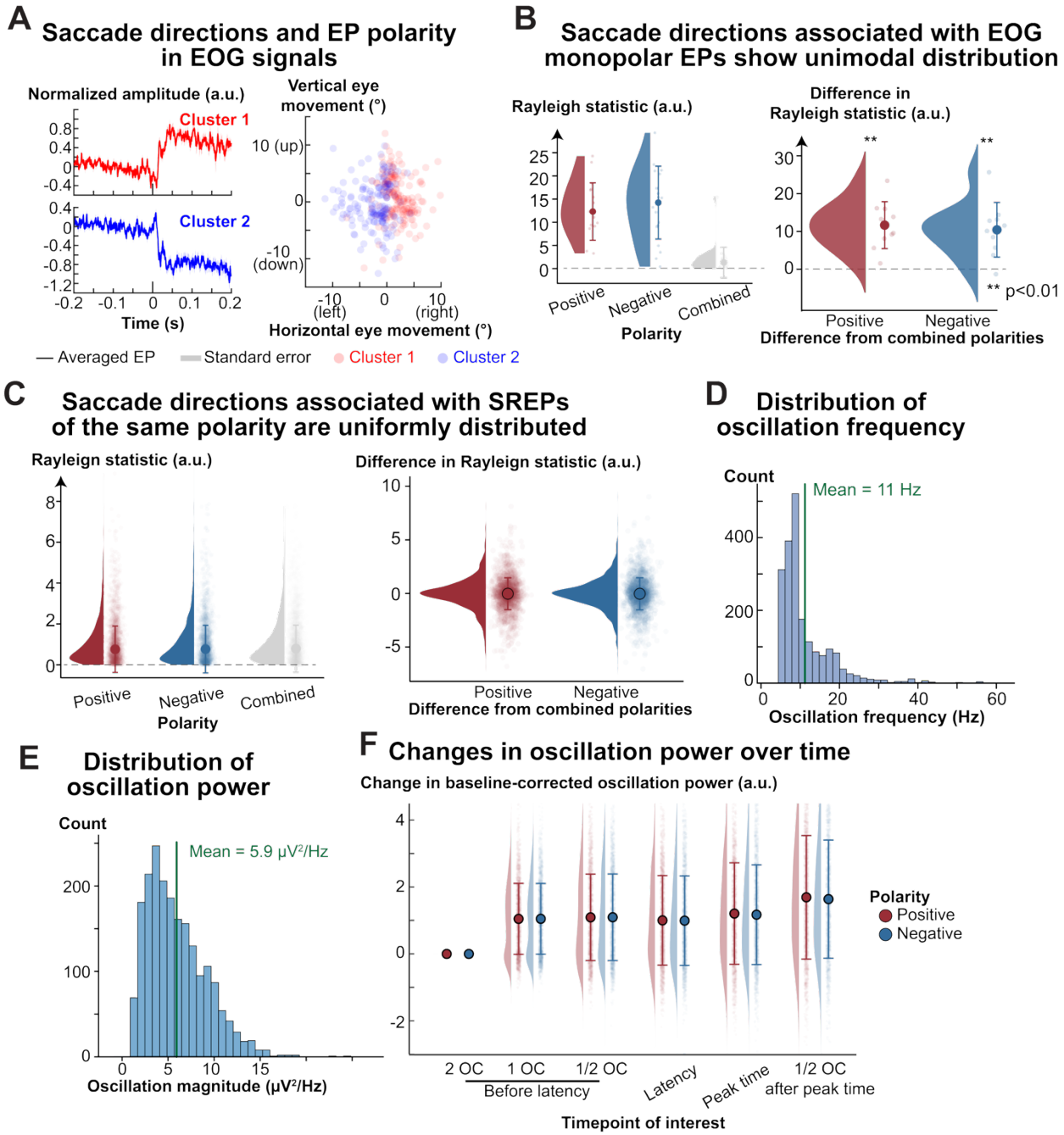

Figure 4 – Figure Supplement 1. Saccade direction is associated with polarity of EOG EPs but not the polarity of SREPs extracted from intracranial LFPs. (A) Relationship between saccade direction and EP polarity in EOG signals. We applied the same clustering and EP characterization procedures to EOG signals. The left panel shows the positive and negative EOG EPs averaged across trials from a representative subject. Time 0 is the saccade offset. The right panel shows the saccade direction associated with the positive and negative EPs. The shaded area in the left panel represents the standard error. **(B)** Saccade directions were unimodally distributed in

monopolar EOG EPs. Assuming EOG signals captured oculomuscular artifacts during saccades, we expected that the circular distribution of saccade direction associated with monopolar EP has a unimodal peak. We used Rayleigh statistics to quantify this unimodal bias. Rayleigh statistics for monopolar EPs were higher than the Rayleigh statistics for combined EPs. Each data point in the plot represents Rayleigh statistics calculated from EOG signals in one subject during one task. We ensured the same sample size when calculating the Rayleigh statistics. We defined the resampling size as the 20th percentile of the number of trials (n = 32) for each subject, each task, and each electrode contact. We sampled the same number of saccade directions associated with monopolar EPs and saccade directions associated with the combined EPs. The right panel shows the distribution of Rayleigh statistic differences (monopolar – combined). For both polarities, differences in Rayleigh statistics were significantly greater than zero (For positive polarity, $t = 5.950$, $p < 0.001$, Cohen's d = 1.881, paired t-test, n = 15; for negative polarity, $t = 4.553$, $p = 0.001$, Cohen's d = 1.440, n = 18). In addition, the circular distribution of saccade direction was significantly different between positive and negative polarity ($p < 0.001$ for all subjects, 95% CI for W statistics = [33.223, 46.050], Mardia-Watson-Wheeler test). **(C)** Saccade directions associated with positive and negative SREPs measured with stereoelectroencephalography. For both polarities, Rayleigh statistic differences (monopolar – combined) were centered at zero (For positive polarity, $t=-0.953$ $p = 0.341$, Cohen's d = -0.022, two-tailed t-test, n = 2068; for negative polarity, $t = -1.028$, $p = 0.304$, Cohen's d = -0.023, n = 2058). To estimate the difference between the saccade directions associated with positive and negative SREPs, we sampled the same number of saccade directions associated with monopolar EPs. Consistently, we defined the resampling size as the 20th percentile of the number of trials (n = 62) for each subject, each task, and each electrode contact. Across subjects, tasks, and electrode contacts, we found no difference in saccade direction between polarities (95% CI for W statistics = [1.926, 2.107], the corresponding 95% CI for p-value is [0.486, 0.512], Mardia-Watson-Wheeler test). **(D)** Distribution of oscillation frequencies in intracranial signals. The mean oscillatory frequency is 11 Hz. To minimize potential confounds from line noise, we identified oscillation frequency as the frequency between 1 and 58 Hz at which the difference between the power spectral density and its one-over-frequency fit was maximal. **(E)** Distribution of oscillation power in intracranial signals. Measured as the difference in power spectral density from a one-over-frequency fit at the oscillatory frequency. **(F)** Changes in oscillation power (i.e., instantaneous power at the oscillatory frequency) over time. To enable cross-subject and cross-contact comparisons, we normalize oscillation power to power at two oscillation cycles before the EP latency. The effect size (Cohen's d) between phase lag index at 2 OCs before latency and subsequent time points (from 1 OC before latency to 1 OC after peak time) were 0.894, 0.780, 0.694, 0.742, and 0.860 (n = 5300).

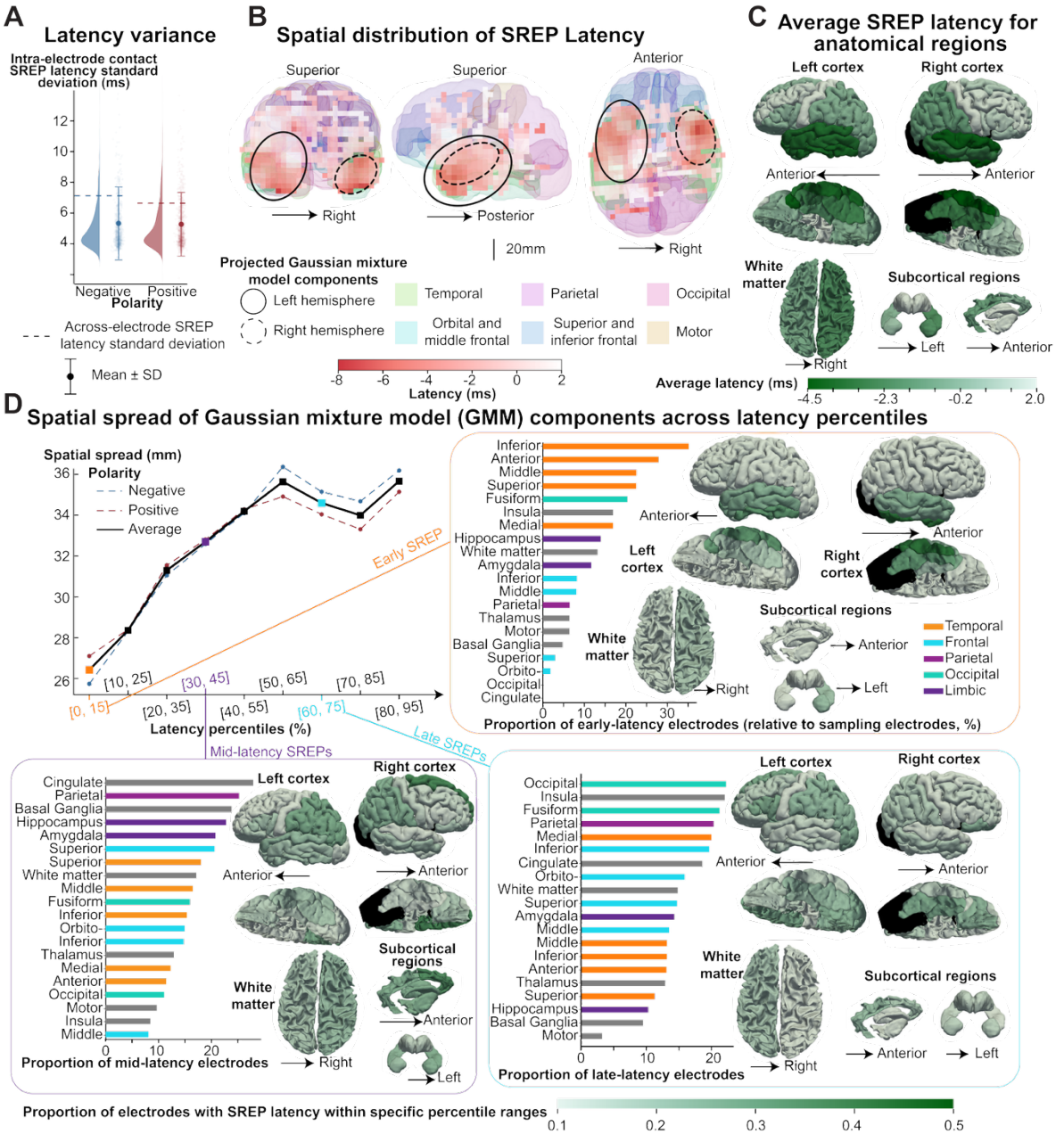
A
Latency variance
Intra-electrode contact SREP latency standard deviation (ms)
Negative
Positive
Polarity
Across-electrode SREP latency standard deviation
Mean ± SD
B
Spatial distribution of SREP Latency
Superior
Superior
Anterior
Right
Posterior
20mm
Right
Projected Gaussian mixture model components
Left hemisphere
Right hemisphere
Temporal
Parietal
Occipital
Orbital and middle frontal
Superior and inferior frontal
Motor
Latency (ms)
C
Average SREP latency for anatomical regions
Left cortex
Right cortex
Anterior
Anterior
White matter
Subcortical regions
Left
Anterior
Right
Average latency (ms)
D
Spatial spread of Gaussian mixture model (GMM) components across latency percentiles
Spatial spread (mm)
Polarity
Negative
Positive
Average
Early SREP
Late SREPs
Mid-latency SREPs
Latency percentiles (%)
Proportion of early-latency electrodes (relative to sampling electrodes, %)
Proportion of mid-latency electrodes
Proportion of late-latency electrodes
Temporal
Frontal
Parietal
Occipital
Limbic
Proportion of electrodes with SREP latency within specific percentile ranges
E
Temporal progression of SREP across anatomical regions
Proportion of electrodes (relative to sampling electrodes, %)
* corrected p<0.05
Frontal
Temporal
Others
Parietal
Limbic
Occipital
Orbital*
Inferior*
Basal Ganglia*
Middle*
Inferior*
Superior*
Latency percentiles (%)
F
Spatial distribution of SREP peak amplitude
Superior
Anterior
Right
Right
Superior
Posterior
Projected GMM components
Left hemisphere
Right hemisphere
Amplitude (a.u.)
G
GMM component spatial spread across amplitude percentiles
Spatial spread (mm)
Polarity
Negative
Positive
Average
Amplitude percentiles (%)

Figure 5. **Spatiotemporal dynamics of SREPs**. **(A)** Comparison between intra-contact SREP latency variance and inter-contact SREP latency variance. The averaged standard deviation of intra-electrode-contact SREP latencies was 5.3 ms for negative and positive SREP. The standard deviation of intra-contact SREP latencies was significantly lower compared to inter-contact SREP latency of 7.1 ms and 6.6 ms for negative and positive SREPs ($N = 786$, W statistics = 24141, $p < 0.001$, Rank-biserial correlation= -0.766 for negative polarity; $N = 797$, W statistics = 34836, $p < 0.001$, Rank-biserial correlation= -0.669 for positive polarity; Wilcoxon signed-rank test). To estimate intra-contact SREP latency variance, we included single trials whose SREP waveforms were similar to the averaged SREP waveform, defined as having a correlation coefficient above the median. We resampled the single-trial SREP latency for each contact to the 50th percentile of the trial count for all electrode contacts. To estimate inter-contact SREP latency variance, we resampled electrode contacts to have equal sample sizes, matching the median of per-contact trial counts. We repeated the process 100 times and plotted the mean inter-contact SREP latency variance using dashed lines. **(B)** Spatial distribution of SREP latencies across electrode contacts. Similar to **Figure 2 – Figure supplement 3**, we projected the 3D brain surface and electrode coordinates onto a 2D plane. We overlay a heatmap to represent the spatial pattern of SREP latencies. To generate the heatmap, we discretized this 2D space into a regular grid with a 5 mm resolution. We computed the local average SREP latency within a 10 mm radius for each grid element. Heatmap elements that have no nearby sampling electrodes are shown as fully transparent. To analyze the spatial dynamics of SREP over time, we stratified electrodes by SREP latency percentiles. For each percentile-defined subset, we applied a 3D Gaussian Mixture Model (GMM) to identify two spatial clusters of electrode contacts. We extracted the cluster centroids in the left and right hemispheres. We quantified the spatial spread based on standard deviations along the x, y, and z axes. The solid and dashed ellipses represent the two GMM components identified from electrode contacts exhibiting SREP latency in the 0 – 15th percentile range. **(C)** Average SREP latency across anatomical regions. We parcellate the brain into White Matter (Left, Right), Hippocampus (Left, Right), Amygdala (Left, Right), Basal Ganglia, Thalamus, Orbitofrontal (Left, Right), Inferior Frontal (Left, Right), Middle Frontal (Left, Right), Superior Frontal (Left, Right), Anterior Cingulate, Posterior Cingulate, Motor (Left, Right), Anterior Temporal (Left, Right), Middle Temporal (Left, Right), Superior Temporal (Left, Right), Inferior Temporal (Left, Right), Medial Temporal (Left, Right), Fusiform (Left, Right), Parietal (Left, Right), Occipital (Left, Right), and Insula (Left, Right). Colors denote the mean SREP latency, averaged across polarities and electrode contacts localized to each anatomical region. **(D)** Relationship between spatial spread and SREP latency percentile ranges. We quantified spatial spread as the square root of the sum of variances along the X, Y, and Z axes (i.e., the Euclidean norm of the standard deviations). For illustration, we selected early, mid, and late percentile ranges ([0–15], [30–45], and [60–75]) and plotted the proportion of

electrodes showing SREP with latency within each range. We calculated the proportion as the ratio between the number of electrodes in a region with latency within a percentile range and the total number of electrodes localized in that region. The accompanying 3D brain plots show the anatomical distribution of these proportions across regions. **(E)** Temporal progression of SREP across anatomical regions. Each data point represents the proportion of electrodes for an anatomical region that showed SREP at a specific latency percentile range. Thick lines represent regions where the proportion changed monotonically across latency percentiles based on Spearman's correlation. We found that orbital ($\rho = 0.82$, Bonferroni corrected asymptotic p = 0.136, number of comparisons = 20) and inferior ($\rho = 0.89$, $corrcted\ p = 0.025$) frontal regions had a lower proportion of early SREPs and a higher proportion of late SREPs. Middle ($\rho = -0.97$, corrected $p < 0.001$), inferior ($\rho = -0.74$, corrected $p = 0.455$), and superior ($\rho = -0.98$, corrected $p < 0.001$) temporal regions showed the opposite pattern. **(F)** Spatial distribution of SREP peak amplitude across electrodes. **(G)** Relationship between spatial spread and SREP peak amplitude percentile ranges.

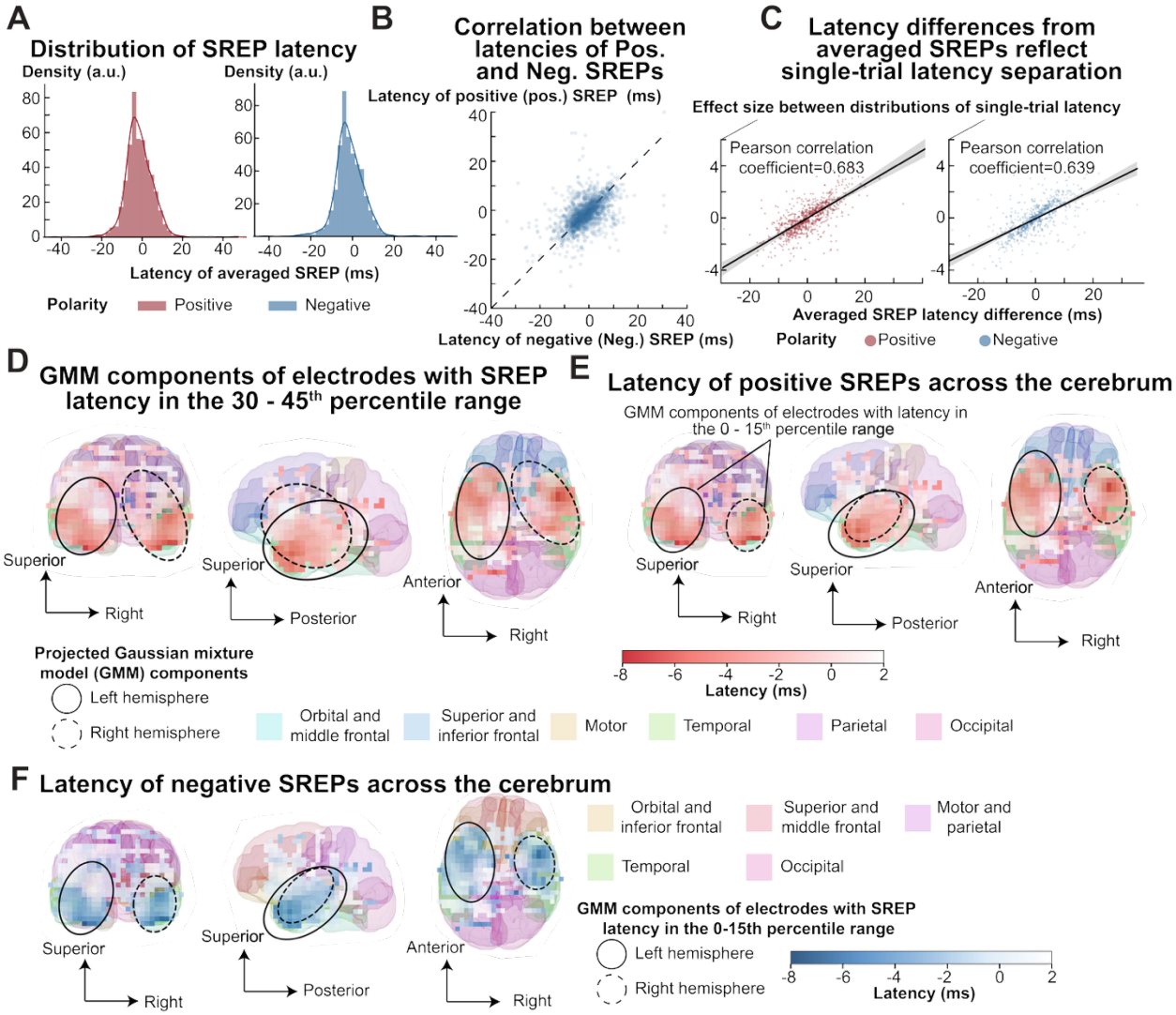

Figure 5 – Figure supplement 1. **SREP latency across the cerebrum**. **(A)** Averaged SREP latency. The mean latency was -1 ms for both positive and negative polarities. The standard deviation was 7.5 ms for positive SREPs and 7.7 ms for negative SREPs, respectively. **(B)** Correlation between latencies of averaged SREPs with positive and negative polarities. They were positively correlated (Pearson's correlation coefficient = 0.436, $p < 0.001$, exact test for Pearson's correlation, $n = 1558$). **(C)** Latency differences between trial-averaged SREPs across electrode contact pairs positively correlated with the effect size of latency differences estimated from single-trial SREPs ($p < 0.001$, exact test for Pearson's correlation, i.e., t-test). Given the large number of possible electrode contact pairs, we randomly sampled 2,000 contact pairs per polarity to reduce computational cost. We randomly sampled 2000 pairs of electrode contacts for each polarity. Illustration of two Gaussian Mixture Model (GMM) components estimated from electrodes with SREP latency in the 30 – 45th percentile range. Each ellipse represents a GMM component, derived from the centroid and standard deviations along the three

spatial axes of the 3D Gaussian distributions. The heatmap represents the average SREP latency averaged across polarities. The underlying projected 3D brain model provides an anatomical reference. As in **Figure 2 – Figure supplement 3**, the color of each heatmap element (5 mm by 5 mm) represents the average latency across electrode contacts localized within 10 mm of that element. **(E)** The spatial distribution of latency for positive SREPs. **(F)** The spatial distribution of latency for negative SREPs. Darker blue in the heatmap denotes earlier SREPs. The color of the underlying 3D brain is adapted from **E**, to avoid overlap with the blue-to-white latency heatmap. In **E** and **F,** the solid and dashed ellipses represent left and right GMM components estimated from the spatial location of electrodes with SREP latency in the 0 – 15th percentile range.

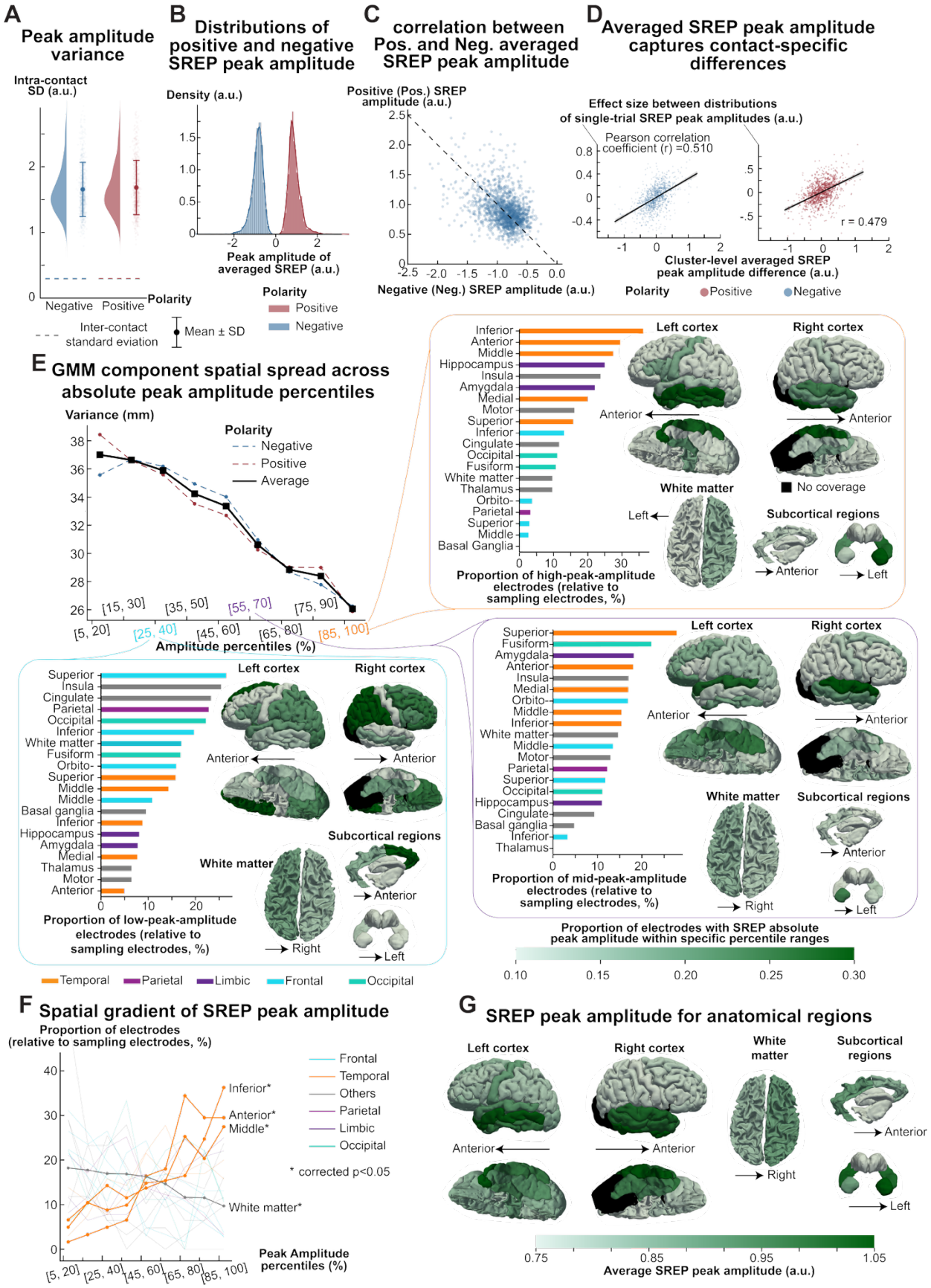
A
Peak amplitude variance
Intra-contact SD (a.u.)
Negative
Positive
Polarity
Inter-contact standard eviation
Mean ± SD
B
Distributions of positive and negative SREP peak amplitude
Density (a.u.)
Peak amplitude of averaged SREP (a.u.)
Polarity
Positive
Negative
C
correlation between Pos. and Neg. averaged SREP peak amplitude
Positive (Pos.) SREP amplitude (a.u.)
Negative (Neg.) SREP amplitude (a.u.)
D
Averaged SREP peak amplitude captures contact-specific differences
Effect size between distributions of single-trial SREP peak amplitudes (a.u.)
Pearson correlation coefficient (r) =0.510
r = 0.479
Cluster-level averaged SREP peak amplitude difference (a.u.)
Polarity
Positive
Negative
E
GMM component spatial spread across absolute peak amplitude percentiles
Variance (mm)
Polarity
Negative
Positive
Average
[5, 20]
[15, 30]
[25, 40]
[35, 50]
[45, 60]
[55, 70]
[65, 80]
[75, 90]
[85, 100]
Amplitude percentiles (%)
Inferior
Anterior
Middle
Hippocampus
Insula
Amygdala
Medial
Motor
Superior
Inferior
Cingulate
Occipital
Fusiform
White matter
Thalamus
Orbito-
Parietal
Superior
Middle
Basal Ganglia
Proportion of high-peak-amplitude electrodes (relative to sampling electrodes, %)
Left cortex
Right cortex
White matter
Subcortical regions
No coverage
Superior
Insula
Cingulate
Parietal
Occipital
Inferior
White matter
Fusiform
Orbito-
Superior
Middle
Middle
Basal ganglia
Inferior
Hippocampus
Amygdala
Medial
Thalamus
Motor
Anterior
Proportion of low-peak-amplitude electrodes (relative to sampling electrodes, %)
Proportion of mid-peak-amplitude electrodes (relative to sampling electrodes, %)
Proportion of electrodes with SREP absolute peak amplitude within specific percentile ranges
Temporal
Parietal
Limbic
Frontal
Occipital
F
Spatial gradient of SREP peak amplitude
Proportion of electrodes (relative to sampling electrodes, %)
Frontal
Temporal
Others
Parietal
Limbic
Occipital
Inferior*
Anterior*
Middle*
White matter*
* corrected p<0.05
Peak Amplitude percentiles (%)
G
SREP peak amplitude for anatomical regions
Left cortex
Right cortex
White matter
Subcortical regions
Average SREP peak amplitude (a.u.)

Figure 5 – Figure supplement 2. **Spatial distribution of SREP peak amplitude**. **(A)** Comparison between intra-contact single-trial SREP peak amplitude variance and inter-contact single-trial SREP peak amplitude variance. The average standard deviation of intra-contact SREP peak amplitudes was 1.656 and 1.685 for negative and positive SREPs, respectively. The standard deviation of intra-contact SREP peak amplitudes was significantly higher compared to inter-contact SREP peak amplitudes of 0.299 and 0.298 (N = 786, W statistics = 0, $p < 0.001$, Rank-biserial correlation = 1 for negative polarity; N = 797, W statistics = 0, $p < 0.001$, Rank-biserial correlation = 1 for positive polarity; Wilcoxon signed-rank test). **(B)** Peak amplitudes of cluster-level averaged SREPs. The mean peak amplitude was 0.897 and -0.883 for positive and negative polarities, respectively. The standard deviation was 0.296 for positive and negative SREPs. **(C)** Correlation between positive and negative averaged SREP peak amplitudes. They were negatively correlated (Pearson's correlation coefficient = -0.365, $p < 0.001$, exact test for Pearson's correlation). **(D)** Correlation between peak amplitude differences between cluster-level averaged SREPs across electrode contact pairs and the effect size of peak amplitude differences estimated from single-trial SREPs. They were positively correlated ($p < 0.001$, exact test for Pearson's correlation). **(E)** Relationship between spatial spread and absolute SREP peak amplitude percentile ranges (related to **Figure 5D**). For illustration, we selected high-, mid-, and low-amplitude percentile ranges ([0–15], [30–45], and [60–75]) and plotted the proportion of electrodes exhibiting SREPs with peak amplitude within each range. We calculated the proportion as the ratio between the number of electrodes in a region with SREP peak amplitude within a percentile range and the total number of electrodes localized in that region. The accompanying 3D brain plots show the anatomical distribution of these proportions across regions. **(F)** Proportion of electrodes with absolute SREP peak amplitude at a specific percentile range per region across absolute amplitude percentile bins. Thick lines represent regions where the proportion changed monotonically across amplitude percentile ranges based on Spearman's correlation. We found that anterior ($\rho = 0.95$, Bonferroni corrected asympototic $p = 0.002$, number of comparisons = 20), inferior ($\rho = 0.95$, $corrcted\ p = 0.001$),and middle ($\rho = 0.93$, $corrcted\ p = 0.005$) temporal regions had a lower proportion of electrodes showing SREPs with low absolute peak amplitude and a higher proportion of electrodes showing SREPs with high peak absolute amplitude. White matter ($\rho = -1$, $corrcted\ p < 0.001$) showed the opposite pattern. **(G)** Spatial distribution of absolute SREP peak amplitudes averaged across electrode contacts localized within an anatomical region.

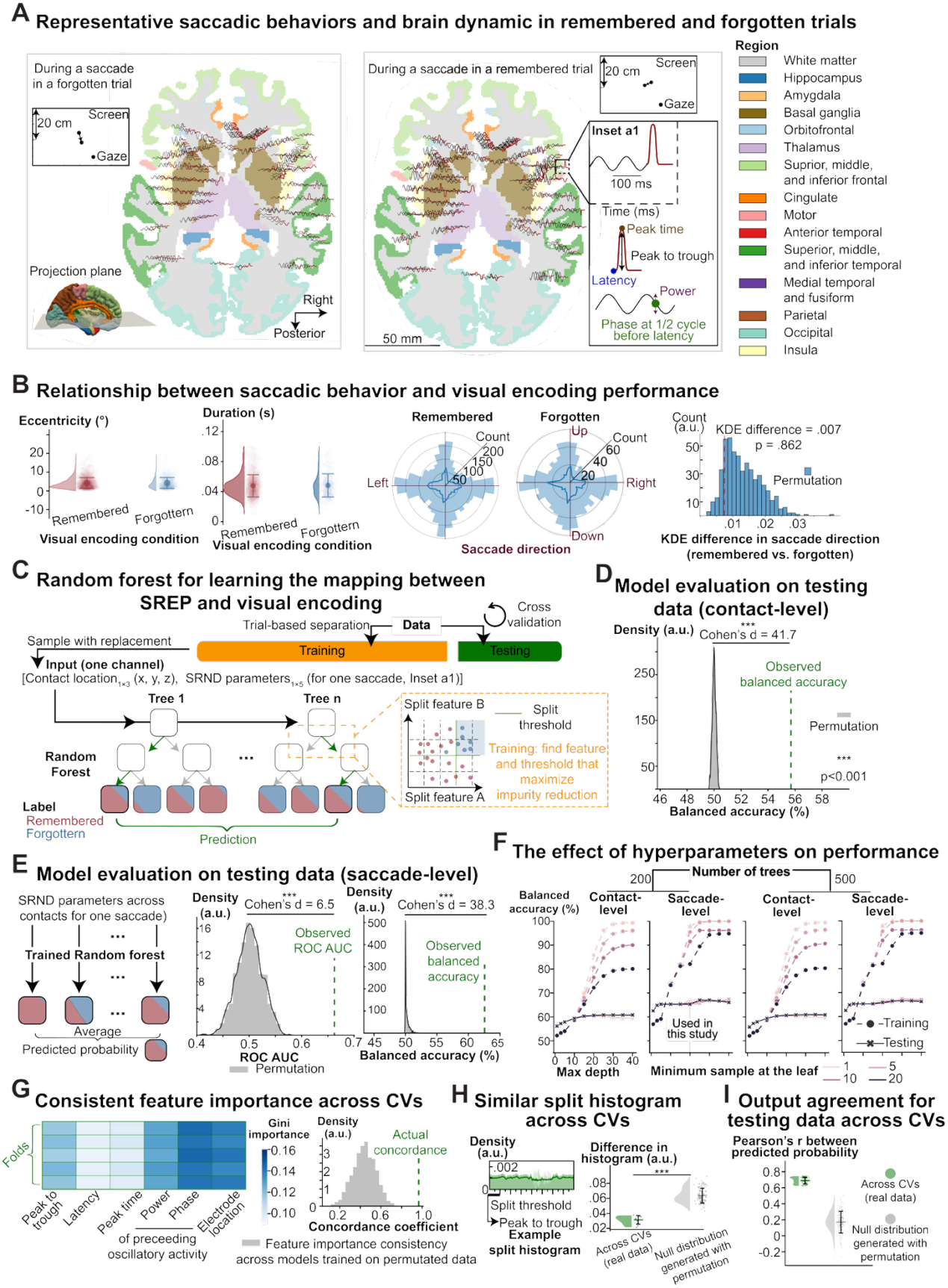
A Representative saccadic behaviors and brain dynamic in remembered and forgotten trials
During a saccade in a forgotten trial
20 cm
Screen
Gaze
Projection plane
Right
Posterior
During a saccade in a remembered trial
Inset a1
100 ms
Time (ms)
Peak time
Peak to trough
Latency
Power
Phase at 1/2 cycle before latency
50 mm
Region
White matter
Hippocampus
Amygdala
Basal ganglia
Orbitofrontal
Thalamus
Suprior, middle, and inferior frontal
Cingulate
Motor
Anterior temporal
Superior, middle, and inferior temporal
Medial temporal and fusiform
Parietal
Occipital
Insula
B Relationship between saccadic behavior and visual encoding performance
Eccentricity (°)
Remembered
Forgottern
Visual encoding condition
Duration (s)
Remembered
Forgottern
Visual encoding condition
Remembered
Forgotten
Count
Left
Right
Up
Down
Saccade direction
Count (a.u.)
KDE difference = .007
p = .862
Permutation
KDE difference in saccade direction (remembered vs. forgotten)
C Random forest for learning the mapping between SREP and visual encoding
Trial-based separation
Data
Cross validation
Sample with replacement
Training
Testing
Input (one channel)
[Contact location1×3 (x, y, z), SRND parameters1×5 (for one saccade, Inset a1)]
Tree 1
Tree n
Random Forest
Label
Remembered
Forgottern
Prediction
Split feature B
Split threshold
Training: find feature and threshold that maximize impurity reduction
Split feature A
D Model evaluation on testing data (contact-level)
Density (a.u.)
Cohen's d = 41.7
Observed balanced accuracy
Permutation
p<0.001
Balanced accuracy (%)
E Model evaluation on testing data (saccade-level)
SRND parameters across contacts for one saccade)
Trained Random forest
Average
Predicted probability
Density (a.u.)
Cohen's d = 6.5
Observed ROC AUC
ROC AUC
Permutation
Density (a.u.)
Cohen's d = 38.3
Observed balanced accuracy
Balanced accuracy (%)
F The effect of hyperparameters on performance
Number of trees
200
500
Balanced accuracy (%)
Contact-level
Saccade-level
Contact-level
Saccade-level
Used in this study
Training
Testing
Max depth
Minimum sample at the leaf
1
5
10
20
G Consistent feature importance across CVs
Folds
Peak to trough
Latency
Peak time
Power
Phase
Electrode location
of preceeding oscillatory activity
Gini importance
Density (a.u.)
Actual concordance
Concordance coefficient
Feature importance consistency across models trained on permutated data
H Similar split histogram across CVs
Density (a.u.)
Split threshold
Peak to trough
Example split histogram
Difference in histogram (a.u.)
Across CVs (real data)
Null distribution generated with permutation
I Output agreement for testing data across CVs
Pearson's r between predicted probability
Across CVs (real data)
Null distribution generated with permutation

Figure 6. **Machine learning reveals predictive mappings between SREPs and visual encoding**. **(A)** Illustration of brain dynamics during a remembered and a forgotten trial. Each trace plotted on top of a horizontal brain slice represents the SREP waveform and the preceding oscillatory activity recorded in an electrode contact. The color of the brain slice denotes anatomical regions. We reconstructed SREP waveforms as sigmoidal rise and fall based on latency, peak time, and peak-to-trough identified in the specific trials. The sigmoidal rise starts at the latency and peaks at the peak time. We reconstruct the preceding oscillatory activity using a 10 Hz sine wave parameterized by instantaneous power and phase at half a cycle before latency. We later trained linear and nonlinear models to predict visual encoding using these five SRND parameters at each electrode contact. The two insets at the top show fixation before and after a saccade, with arrows indicating saccade direction. **(B)** Relationship between saccadic behavior and visual encoding performance. From left to right, we show the distribution of saccade eccentricity, saccade duration, and saccade direction in remembered and forgotten trials. The rightmost panel shows the difference in circular distribution of saccade direction between remembered and forgotten trials. To quantify the difference in saccade direction, we estimated circular kernel density functions for remembered and forgotten trials and computed the absolute area under the difference between the two density curves. The red dotted line represents the actual difference in saccade direction between remembered and forgotten trials. The blue histogram represents the null distribution of saccade direction differences from permuted trial conditions (remembered vs. forgotten). **(C)** Model architecture for learning the mapping from SRND parameters to visual encoding. The input to the random forest is a vector including the spatial location of electrode contacts and SRND parameters (e.g., SREP latency, peak-to-trough, peak time, phase and power of preceding oscillatory activity). As the remembered and forgotten trials are imbalanced, we resampled both classes to achieve a balanced input. In addition, we added normally distributed spatial jitters to electrode contact location to enable learning mapping specific to spatial location while preventing associating the exact electrode contact location with the trial label. For prediction, each decision tree outputs a probability for the remembered and forgotten classes that reflects the proportion of training samples from each class reaching the corresponding leaf. The final predicted probability is the average of these vectors across all trees. **(D)** Balanced accuracy of the random forest in predicting visual encoding performance on testing data. We performed 200 permutations to generate a null distribution of balanced accuracy. The observed balanced accuracy was 55.7%, exceeding all values in the null distribution. **(E)** Saccade-level model performance. Using these saccade-level predicted probabilities, we computed the area under the receiver operating characteristic curve (ROC AUC). An illustration of calculating ROC AUC is shown in **Figure 2C**. The observed ROC AUC on test data (0.662) exceeded all values from a null distribution generated by training and evaluating models on data with permuted labels. The rightmost panel shows the observed saccade-level balanced

accuracy (62.6%), compared to the null distribution. To calculate the saccade-level balanced accuracy, we determined the optimal threshold, sweeping from 0 to 1, that maximized balanced accuracy. We applied this process to both observed data and data with permutated labels. **(F)** Effect of hyperparameters on model performance during training and testing. We evaluated how different hyperparameter settings affected the performance of random forests. The hyperparameter includes the number of trees, the maximum tree depth, and the minimum sample size at the leaf. In general, deeper trees with a small sample size can learn more complex patterns but risk overfitting. In each panel, color represents the minimum sample at the leaf, the x-axis represents the maximum depth, and the y-axis represents balanced accuracy. From left to right, the four panels show: (1) electrode contact-level performance using 200 trees, (2) saccade-level performance using 200 trees, (3) contact-level performance using 500 trees, and (4) saccade-level performance using 500 trees. In this study, we used a default hyperparameter setting of 200 decision trees, a maximum depth of 20, and a minimum leaf size of 1. This set of hyperparameters achieved moderate balanced accuracy during training and moderate generalization on test data, without evidence of overfitting. Therefore, we used the default parameters for consistency and computational efficiency, although performance on test data slightly improved with 500 decision trees. **(G)** Similar mapping from SRND parameters to visual encoding outcome across cross-validations (CVs). The left panel shows the feature importance based on the Gini impurity reduction across the 5-fold validations. We used Kendall's coefficient of concordance to quantify the concordance of feature importance across CVs and across permutated data. The right panel shows that the concordance coefficient across CVs (Kendall's W = 0.966) for the actual data exceeds all values in the null distribution (mean Kendall's W = 0.439, SD = 0.110). **(H)** Consistent decision boundaries across cross-validation folds. For each model trained on the actual data, we computed the histogram of split thresholds for every feature. To assess consistency, we compared split histograms between pairs of folds and quantified their similarity using the area under the absolute difference curve. The right panel shows that the split histogram for models trained on actual data across CVs were more similar than the null distribution generated based on permuted data (U = 0.000, $p < 0.001$, Mann-Whitney U test, Cohen's d = -3.398, $n_{actual} = 10, n_{null} = 100$). **(I)** Consistent predictions of random forest models across CV folds. To assess the output agreement, we randomly sampled an observation from the test set (in one of the folds) and passed it to two models trained from different CV folds. We repeated this procedure 200 times, both for models trained on actual data and on models trained on permuted data. We used Pearson's correlation coefficient between the predicted probabilities from a pair of models to quantify the output agreement between the two models. Each data point in the plot represents one such correlation. Models trained on actual data had higher output agreement across CVs than those trained from permuted data (U = 40000, $p < 0.001$, Mann-Whitney U test, Cohen's d = 5.208, $n_{actual} = 200, n_{null} = 200$).

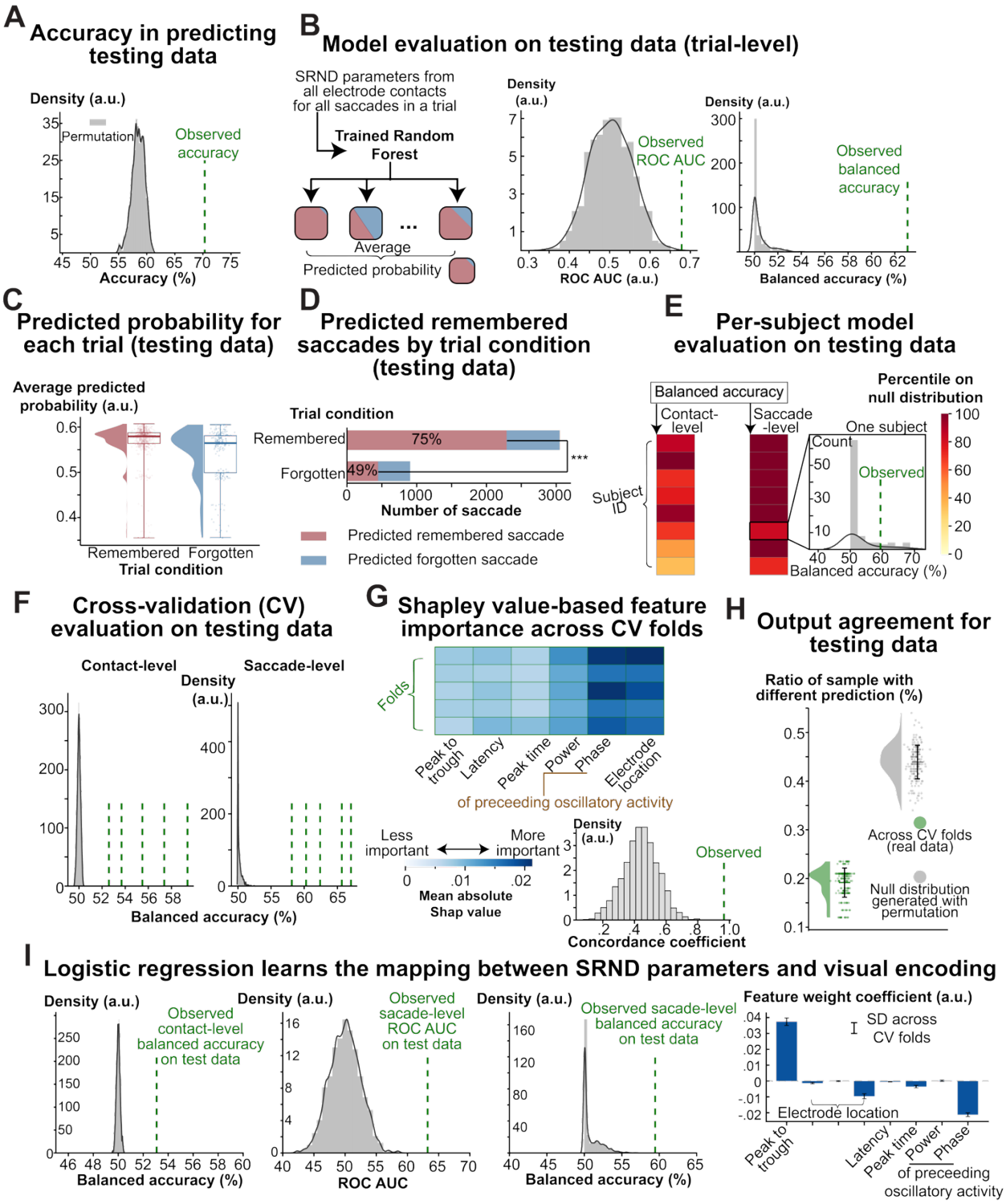

Figure 6 – Figure supplement 1. Validation of the model's ability to learn the mapping between SRND parameters and visual encoding. (A) Accuracy of the random forest in predicting visual encoding performance on testing data. We performed 200 permutations to generate a null distribution of accuracy. The observed accuracy was

70.3%, exceeding all values in the null distribution. **(B)** Trial-level model performance on test data. We used SRND parameters in all electrode contacts across all saccades during a trial as input to the model and used the average predicted probability as the trial-level predicted probability. Using these trial-level predicted probabilities, we computed the area under the receiver operating characteristic curve (ROC AUC). An illustration of calculating ROC AUC is shown in **Figure 2C**. The observed ROC AUC on test data (0.678) exceeded all values from a null distribution generated by training and evaluating models on data with permuted labels. The rightmost panel shows the observed trial-level balanced accuracy (63.1%), compared to the null distribution. To calculate the trial-level balanced accuracy, we determined the optimal threshold for average predicted probability, sweeping from 0 to 1, that maximized balanced accuracy. We applied this process to both observed data and data with permutated labels. **(C)** Average predicted probability in remembered and forgotten trials. Each data point in the plot represents the average predicted probability for a trial, and color denotes the trial condition. For test data, the average predicted probability was higher in remembered trials, compared to forgotten trials (U statistic = 84652, $p < 0.001$, rank-biserial correlation = 0.333, $n_{remembered}$ = 635, $n_{forgotten}$ = 200, Mann–Whitney U test). **(D)** Proportion of predicted remembered saccades and forgotten saccades in remembered and forgotten trials. The predicted label for a saccade was based on the average predicted probability across all recorded SREPs. The trained random forest classified 75% of saccades in remembered trials as remembered saccades and 49% of saccades in forgotten trials as forgotten saccades. A chi-squared test of independence revealed a significant association between trial condition and predicted saccade labels ($\chi^2(1)$=217.89, $p < 0.001$). **(E)** Generalizability of the model across individual subjects. We evaluated the model's performance separately for each subject's test data using saccade- and electrode contact-level balanced accuracy, averaged across cross-validation (CV) folds. For each subject, we generated a null distribution of balanced accuracy using models trained on permuted labels. The color represents the percentile rank relative to the null distribution for each subject. The observed saccade-level balanced accuracy exceeded the null distribution for 6 out of 8 subjects. We note that the other two subjects had the lowest correct recall rate (48% and 59%, subject ID 6 and 8, **Supplementary Table 3**). Correct recall rate is the proportion of previously presented images that were correctly recognized during the memory test, The inset shows the null distribution and observed balanced accuracy for a subject (Subject ID 6). **(F)** Electrode contact- and saccade-level balanced accuracy of all random forest models trained in 5-fold CV. These performance metrics exceeded all values in the null distribution. The green dashed lines show the observed balanced accuracy for each CV fold. **(G)** Concordance of Shapley value–based feature importance across CVs. We used Shapley values to interpret the contribution of each feature to the model's predictions. Shapley values, derived from cooperative game theory, quantify each feature's marginal contribution to the model's output by averaging over all possible

combinations of feature subsets. The color in the main plot represents the mean absolute Shapley value for each feature, each fold. The lower histogram shows that the Kendall's coefficient of concordance based on the mean absolute Shapley value for trained models across CVs exceeds all concordance coefficients in the null distributions. We generated the null distribution by calculating the concordance coefficient from 5 randomly sampled models trained on permuted data. **(H)** Output agreement across CVs on test data. In addition to **Figure 6I**, we assessed output agreement between models trained on different CV splits based on the ratio of samples with different predictions. For a pair of models trained on actual data in different CV folds, we passed the same test data to both models and computed the proportion of samples with different predictions. The green half violin shows the distribution of this disagreement ratio across models trained on actual data in different CV folds, and the grey half violin represents the null distribution generated from two randomly sampled models trained on permuted data. Summary bars on the right indicate the mean and standard deviation of disagreement ratios for models trained on observed or permuted labels. **(I)** Evaluation of logistic regression for mapping SRND parameters to visual encoding. As the anatomical regions and their function are not linearly distributed in the brain, we used non-linear models (random forest) to learn the mapping from SRND parameters recorded at specific brain regions to visual encoding. To assess whether there is a linear relationship, we trained logistic regression models using the same data and labels as those in **Figure 6C**. We evaluate model performance on held-out test data using electrode contact-level balanced accuracy, saccade-level ROC AUC, and saccade-level balanced accuracy, similar to **Figure 6D–E**. We found that logistic regression performed well above chance, although not as well as the random forest model. The rightmost plot shows the weight coefficient for each feature, suggesting that a higher peak-to-trough value was associated with remembered trials. Caution is warranted when interpreting the negative coefficient for the phase of preceding oscillatory activity, as phase is a circular variable and linear models may not fully capture its periodic nature.

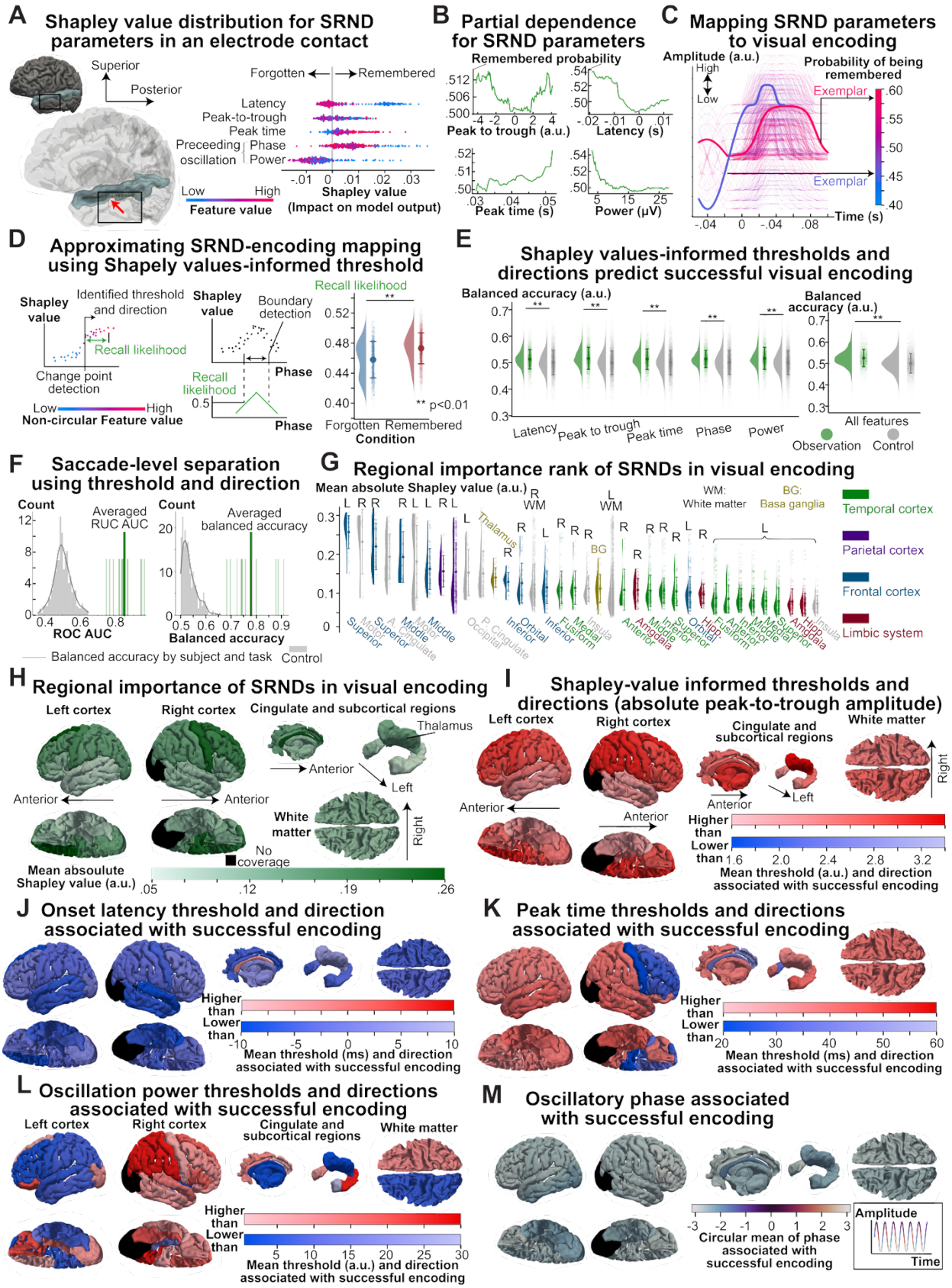
A
Shapley value distribution for SRND parameters in an electrode contact
Superior
Posterior
Forgotten
Remembered
Latency
Peak-to-trough
Peak time
Preceeding oscillation
Phase
Power
Low
High
Feature value
Shapley value (Impact on model output)
B
Partial dependence for SRND parameters
Remembered probability
Peak to trough (a.u.)
Latency (s)
Peak time (s)
Power (μV)
C
Mapping SRND parameters to visual encoding
Amplitude (a.u.)
High
Low
Probability of being remembered
Exemplar
Exemplar
Time (s)
D
Approximating SRND-encoding mapping using Shapely values-informed threshold
Shapley value
Identified threshold and direction
Recall likelihood
Change point detection
Low
High
Non-circular Feature value
Shapley value
Boundary detection
Phase
Recall likelihood
Phase
Recall likelihood
** p<0.01
Forgotten
Remembered
Condition
E
Shapley values-informed thresholds and directions predict successful visual encoding
Balanced accuracy (a.u.)
Latency
Peak to trough
Peak time
Phase
Power
Balanced accuracy (a.u.)
All features
Observation
Control
F
Saccade-level separation using threshold and direction
Count
Averaged RUC AUC
ROC AUC
Count
Averaged balanced accuracy
Balanced accuracy
Balanced accuracy by subject and task
Control
G
Regional importance rank of SRNDs in visual encoding
Mean absolute Shapley value (a.u.)
WM: White matter
BG: Basa ganglia
Temporal cortex
Parietal cortex
Frontal cortex
Limbic system
H
Regional importance of SRNDs in visual encoding
Left cortex
Right cortex
Cingulate and subcortical regions
Thalamus
Anterior
Left
Anterior
Anterior
White matter
Right
No coverage
Mean absoulute Shapley value (a.u.)
I
Shapley-value informed thresholds and directions (absolute peak-to-trough amplitude)
Left cortex
Right cortex
Cingulate and subcortical regions
White matter
Anterior
Anterior
Anterior
Left
Right
Higher than
Lower than
Mean threshold (a.u.) and direction associated with successful encoding
J
Onset latency threshold and direction associated with successful encoding
Higher than
Lower than
Mean threshold (ms) and direction associated with successful encoding
K
Peak time thresholds and directions associated with successful encoding
Higher than
Lower than
Mean threshold (ms) and direction associated with successful encoding
L
Oscillation power thresholds and directions associated with successful encoding
Left cortex
Right cortex
Cingulate and subcortical regions
White matter
Higher than
Lower than
Mean threshold (a.u.) and direction associated with successful encoding
M
Oscillatory phase associated with successful encoding
Circular mean of phase associated with successful encoding
Amplitude
Time

Figure 7. Explanatory analysis of the mapping between saccade-related neural dynamic (SRND) model parameters and visual encoding. **(A)** Interpretation of the learned relationship between SRND parameters and visual encoding using Shapley values. This panel shows the Shapley values for SRND parameters recorded at an electrode contact in the superior temporal gyrus. Each point represents the Shapley value of a feature value, quantifying how much this feature value contributed to the model's (e.g., random forest model) prediction. The color represents the relative feature value, mapped separately for each feature from low to high. A positive Shapley value indicates that the feature value increased the predicted probability of successful visual encoding by the Shapley value. **(B)** Partial dependence plots for SRND parameters recorded in the same electrode contact are shown in panel **A**. Each curve represents the marginal effect of a feature on the predicted probability of successful visual encoding by averaging out the effects of all other features in the model. This panel illustrates how each feature influences a model's prediction, allowing for a better understanding of Shapley values presented in **A**. For example, in panel **A**, an earlier SREP (lower latency) is associated with a higher Shapley value, which is confirmed by the partial dependence plot in panel **B.** Given that Shapley values are based on observed data and additive, we use them to interpret learned mapping in the random forest model. **(C)** Reconstructed SRND model and associated probability of successful encoding for the electrode contact shown in panel **A**. We systematically varied SRND parameters, including instantaneous phase and power at 0.5 oscillation cycles (OCs) before SREP latency, SREP latency, peak-to-trough amplitude, and peak time. We input the feature combinations and the electrode contact's spatial coordinates into the trained random forest model to obtain the predicted probability of successful visual encoding. Each curve represents the reconstructed SREP waveform combined with preceding oscillatory activities. We reconstructed the preceding oscillatory activities using a 10Hz sinusoidal wave, with instantaneous phase and power measured at half a cycle before the SREP latency. We reconstructed the SREP using two sigmoid functions: one for the rising phase, beginning from the SREP latency and oscillation amplitude at the SREP latency, to the peak time and the peak-to-trough amplitude at the peak time; and one for the falling phase from the peak time onward. Reconstructed SREP and preceding oscillation are color-coded by their predicted encoding probability. **(D)** Interpretation of the learned mapping in the random forest model using Shapley value-informed threshold and directions. For non-circular features, such as absolute peak-to-trough amplitude, we ordered observations by feature values. The left plot shows the Shapley values over the ordered feature values. We detected a feature value that minimized the total sum of squared differences between Shapley values and their respective means within segments separated by this value. For the circular feature, the instantaneous phase of the preceding oscillatory activities, we searched for a window (e.g., two boundaries on the unit circle) that minimized the sum of squared Shapley value differences from the mean within and outside the window. For each feature, we defined

the direction associated with successful encoding by comparing the average Shapley value between the two sides of the threshold. For the circular feature, we compared Shapley values inside and outside the identified window. To confirm that the Shapley value-informed thresholds and directions explain visual encoding, we calculated recall likelihood, a probability-like measure of successful encoding based on the thresholds and directions. For each observation, we computed recall likelihood as the distance between the feature value and the threshold, scaled by the standard deviation of the feature values. Depending on the Shapley value-informed direction, we added or subtracted the scaled distance from the prior probability (i.e., 0.5) and then clipped the result to the range [0, 1]. For circular features, the same logic was applied using the shortest angular distance between a given feature value and the boundaries of the encoding-favorable window. The right plot shows the distribution of recall likelihood averaged across electrode contacts in remembered and forgotten trials ($N_{remember} = 3052$, $N_{forgotten} = 906$, U = 1.872×10^6, p < 0.001, Mann-Whitney U test, rank-biserial correlation coefficient = 0.354). **(E)** Balanced accuracy of distinguishing between remembered and forgotten trials using recall likelihoods computed from Shapley value-informed thresholds and directions. For each saccade, we computed the recall likelihood of each SRND parameter at each electrode contact and compared it with a baseline probability of 0.5. The left plot shows the distribution of balanced accuracy using actual and control Shapley value-informed thresholds and directions. We generated the control thresholds and directions by randomly sampling thresholds from the observed feature values. For all SRND parameters, the balanced accuracy was higher using recall likelihood based on actual Shapley value-informed threshold and direction ($N_{observation} = 2707$, $N_{control} = 5414$, p < 0.001, t test, Cohen's d ranged from 0.296 to 0.390). The right plot shows the balanced accuracy of separating successful visual encoding from unsuccessful visual encoding using recall likelihood for all features ($N_{observation} = 2707$, $N_{control} = 5414$, U = 9.767×10^6, p < 0.001, Mann-Whitney U test, Cohen's d = 0.571). These results suggest that Shapley value-informed thresholds and directions reflect cognitive state related to successful visual encoding. We considered an observation of SREP at an electrode contact to be associated with successful visual encoding if more than half of the feature values exceeded the 0.5 baseline probability. **(F)** Saccade-level separation between remembered and forgotten trials using Shapley value-informed recall likelihood. For each saccade, we calculated the proportion of SRND parameters associated with successful visual encoding across electrode contacts. We generated the receiver operating characteristic (ROC) curve by varying the proportion threshold. The left plot shows the distribution of area under the ROC curve (AUC), and the right plot shows the distribution of balanced accuracy at the optimal proportion threshold. These two plots show saccade-level separation between remembered and forgotten trials based on Shapley value-informed thresholds and directions, versus the separation based on thresholds randomly sampled from the feature values. Individual green lines represent the observed AUC or

balanced accuracy for each subject and each task. For each plot, the thicker green line represents the averaged observed AUC (84.9%) or balanced accuracy (77.9%). The rank-biserial correlation was 1.000, and Cohen's d was 6.789 for the averaged AUC compared to the control distribution. Rank-biserial correlation was 1.000, and Cohen's d was 8.761 for balanced accuracy compared to the control distribution. **(G)** Contribution of SRND parameters to visual encoding across anatomical regions. To quantify the regional contribution of SRND parameters to visual encoding, we computed the mean absolute Shapley value for each anatomical region by averaging across electrode contacts within this region and across all SRND parameters. A higher mean absolute Shapley value indicates that the SRND parameters at this region have a greater influence on visual encoding performance. **(I–M)**, Spatial distribution of SRND parameters associated with successful visual encoding across anatomical regions. The five panels visualize the Shapley value-informed direction and threshold for SRND parameters associated with successful visual encoding at each anatomical region. We used two color schemes. The red color map (light red to red) indicates regions where higher feature values were associated with successful encoding. The blue colormap (light blue to blue) indicates regions where lower feature values were associated with successful encoding. The colors in the two color maps reflect the threshold value, with red and blue corresponding to the most extreme thresholds. For example, a red region indicates that high feature values above a relatively high threshold are associated with successful visual encoding. For the circular SREP characteristic, the instantaneous phase at 0.5 OCs before SREP latency, the color denotes the angular mean of the window of phase associated with successful visual encoding. We color-coded a sinusoidal signal by phase to facilitate interpretation. The orientation of the 3D brain models matches the orientation annotated in panel **I**.

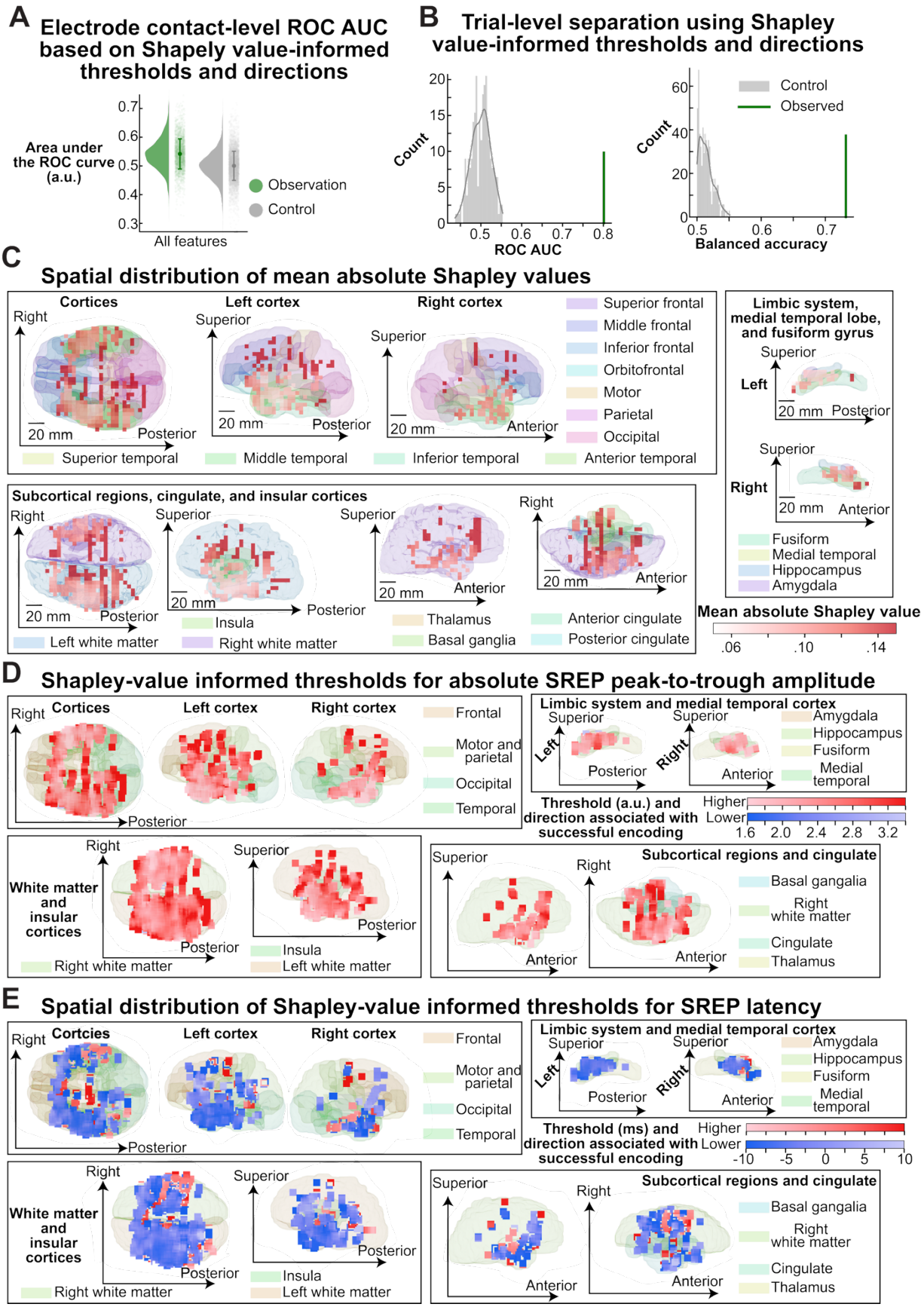
A
Electrode contact-level ROC AUC based on Shapely value-informed thresholds and directions
Area under the ROC curve (a.u.)
0.7
0.6
0.5
0.4
0.3
All features
Observation
Control
B
Trial-level separation using Shapley value-informed thresholds and directions
Count
ROC AUC
Balanced accuracy
Control
Observed
C
Spatial distribution of mean absolute Shapley values
Cortices
Left cortex
Right cortex
Right
Superior
Posterior
Anterior
20 mm
Superior frontal
Middle frontal
Inferior frontal
Orbitofrontal
Motor
Parietal
Occipital
Superior temporal
Middle temporal
Inferior temporal
Anterior temporal
Limbic system, medial temporal lobe, and fusiform gyrus
Left
Right
Fusiform
Medial temporal
Hippocampus
Amygdala
Subcortical regions, cingulate, and insular cortices
Insula
Left white matter
Right white matter
Thalamus
Basal ganglia
Anterior cingulate
Posterior cingulate
Mean absolute Shapley value
.06
.10
.14
D
Shapley-value informed thresholds for absolute SREP peak-to-trough amplitude
Cortices
Left cortex
Right cortex
Frontal
Motor and parietal
Occipital
Temporal
Limbic system and medial temporal cortex
Amygdala
Hippocampus
Fusiform
Medial temporal
Threshold (a.u.) and direction associated with successful encoding
Higher
Lower
1.6
2.0
2.4
2.8
3.2
White matter and insular cortices
Right white matter
Insula
Left white matter
Subcortical regions and cingulate
Basal gangalia
Right white matter
Cingulate
Thalamus
E
Spatial distribution of Shapley-value informed thresholds for SREP latency
Cortcies
Left cortex
Right cortex
Frontal
Motor and parietal
Occipital
Temporal
Limbic system and medial temporal cortex
Amygdala
Hippocampus
Fusiform
Medial temporal
Threshold (ms) and direction associated with successful encoding
Higher
Lower
-10
-5
0
5
10
White matter and insular cortices
Right white matter
Insula
Left white matter
Subcortical regions and cingulate
Basal gangalia
Right white matter
Cingulate
Thalamus

Figure 7 – Figure supplement 1. **Validation and illustration of Shapley value-informed thresholds and directions for successful visual encoding**. **(A)** Area under the receiver operating characteristic (ROC) curve for classifying whether a SREP recorded at an electrode contact during a saccade occurred in a remembered or forgotten trial, using recall likelihoods (detailed in **Figure 7D**) computed from Shapley value-informed thresholds and directions. We computed the ROC by systematically varying the decision threshold applied to the recall likelihood; that is, at each threshold, we computed the true positive rate and the false positive rate. We generated the control thresholds and directions by randomly sampling thresholds from the observed feature values. The area under the curve (AUC) was higher using recall likelihood based on actual Shapley value-informed threshold and direction ($N_{observation}$ = 2707, $N_{control}$ = 5414, p < 0.001, Mann-Whitney U test, U = 1.067×10^7, Cohen's d = 0.817). **(B)** Area under the ROC curve and balanced accuracy of separating remembered from forgotten trials using recall likelihoods (detailed in **Figure 7D**) aggregated across all saccades and electrode contacts for each trial. The grey distribution represents the ROC curve or balanced accuracy based on surrogate recall likelihood computed from control Shapley value-informed thresholds and directions. We generated the control thresholds and directions by randomly sampling thresholds from the observed feature values. The green vertical line represents the actual ROC curve or balanced accuracy based on actual recall likelihood. **(C)** Degree of contribution of SRND parameters to successful visual encoding across anatomical regions. We quantified where SRND parameters contributed more to successful visual encoding using mean absolute Shapley values for each electrode contact. Similar to **Figure 2 – Figure supplement 3**, we projected the 3D brain surface and electrode coordinates onto a 2D plane. We used a heatmap to represent the spatial pattern of mean absolute Sharpey values. To generate the heatmap, we discretized this 2D space into a 5 mm × 5 mm grid. For each electrode, we assigned its mean absolute Shapley value to the nearest grid element to preserve anatomical specificity. To account for the recording sensitivity of stereo-encephalogram signals, estimated to be approximately 10 mm, we computed the local average within a 10 mm radius for each grid element. Heatmap elements that have no nearby electrodes are fully transparent. Three panels show spatial distributions of mean absolute Shapley values across (i) cortices, (ii) subcortical structures, cingulate and insular cortices, and (iii) limbic regions. The heatmap color encodes the mean absolute Shapley values. The background anatomical surfaces provide spatial reference and are color-coded based on anatomical regions; their colors do not represent Shapley values. **(D)** Thresholds and directions of SREP magnitude (i.e., peak-to-trough amplitude) associated with successful visual encoding across anatomical regions. To visualize how SREP magnitude relates to successful encoding, we projected the brain model and electrodes onto a 2D plane and discretized this 2D space into a 2 mm × 2 mm grid. Since directions may differ for adjacent grid elements, spatial averaging is not appropriate. To account for the recording sensitivity of stereo-encephalogram

signals, we considered electrodes within a 10 mm radius for each grid element. We determined the dominant direction, defined as whether higher or lower absolute peak-to-trough amplitude values were more frequently associated with successful encoding. For each grid element, we computed the average of Shapley value-informed thresholds for electrode contacts within a 10 mm radius whose Shapley value-informed direction matched the majority direction. We used two color schemes to represent the thresholds of SREP magnitude associated with successful visual encoding. The red color map (light red to red) indicates regions where higher feature values were associated with successful encoding. The blue colormap (light blue to blue) indicates regions where lower feature values were associated with successful encoding. Within each color map, the color intensity reflects the threshold, with darker red and blue corresponding to more extreme thresholds. **(E)** Thresholds and directions of SREP onset latency associated with successful visual encoding across anatomical regions.

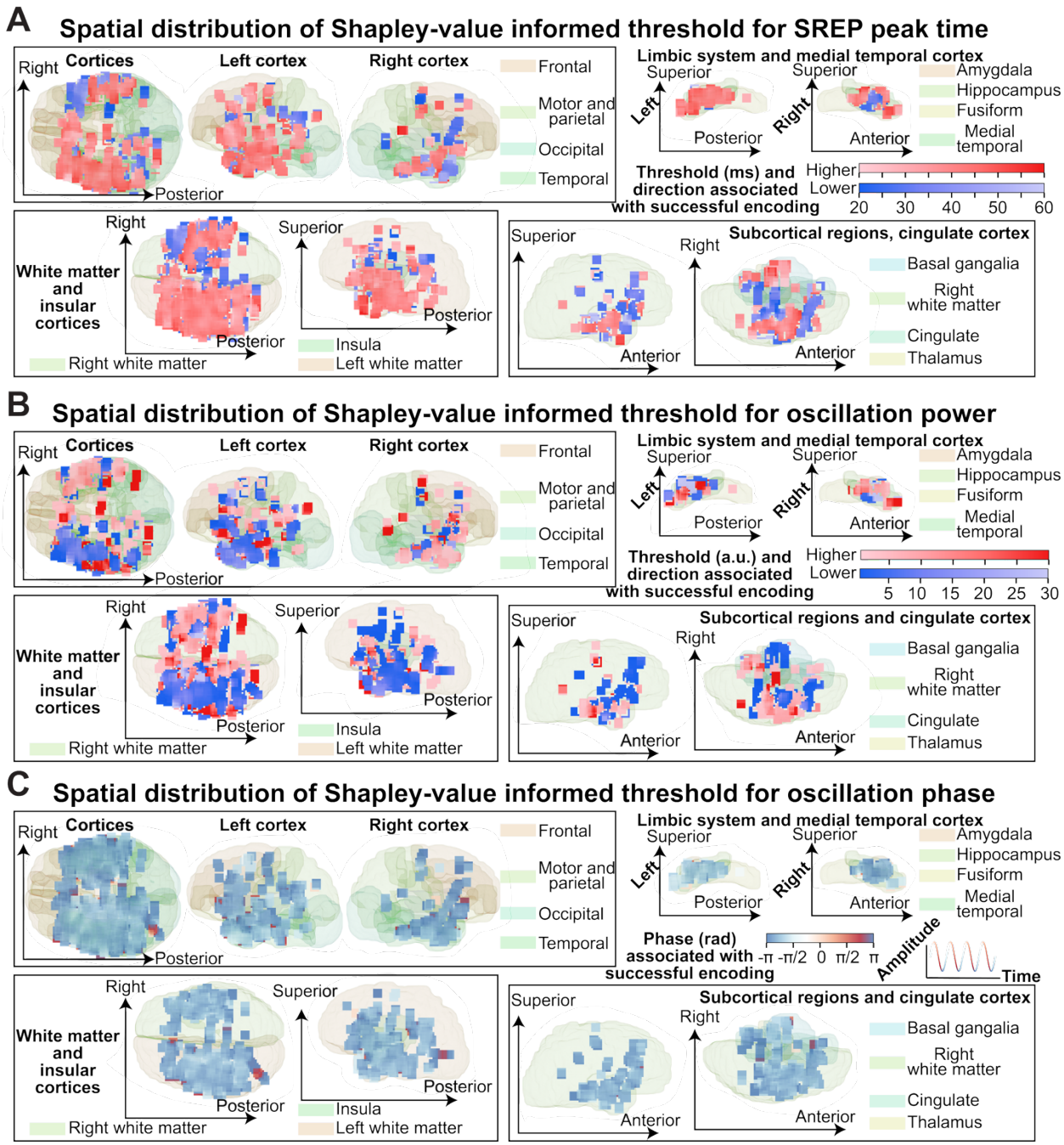

Figure 7 – Figure supplement 2. SRND parameters associated with successful visual encoding across anatomical regions. (A–B) . Thresholds and directions of SREP peak time and instantaneous power of the preceding oscillation associated with successful visual encoding. We computed the heatmaps using the same method as in **Figure 7 and Figure Supplement 1D**. **(C)** Instantaneous phase of the preceding oscillation associated with successful visual encoding. The heatmap color represents the angular mean of the instantaneous phase across electrodes within a 10 mm radius that were associated with successful encoding.

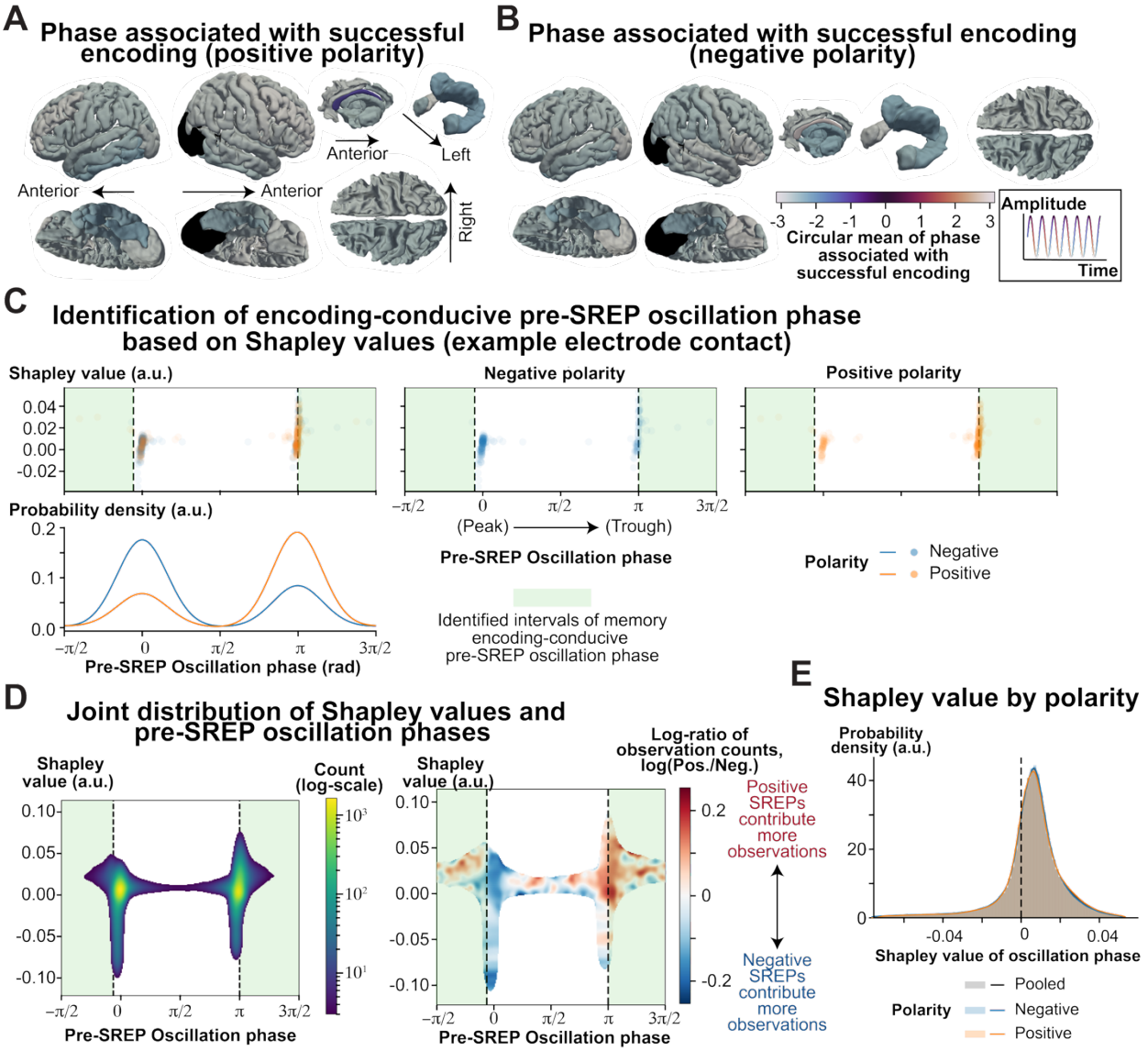

Figure 7 – Figure supplement 3. **Pre-SREP oscillatory phase associated with successful visual encoding across anatomical regions. (A–B)**. Spatial distribution of oscillation phase half oscillation cycle before SREP onset latency associated with successful visual encoding for positive (**A**) and negative polarity (**B**) SREPs. We computed oscillation cycle based on dominant oscillation frequency at each location. (**C**) Identification of encoding-conducive ranges of pre-SREP oscillation phases using Shapley values. This panel shows an example from one electrode contact in the left middle temporal lobe. The right plot in the top row shows the Shapley values associated with pre-SREP oscillatory phase, with color indicating SREP polarity. Middle and right plots in the top row show the same relationship restricted to negative and positive polarity SREPs, respectively. Although phase distributions differed between polarities, the phase

interval associated with higher Shapley values (i.e., greater predicted probability of successful encoding) was consistent across polarities. We identified encoding-conducive phase intervals by partitioning the oscillation phases into two segments that minimized within-segment variance of Shapley values and comparing mean Shapley values between segments (see **STAR Methods** - Shapley value-informed thresholds and directions). For visualization, we displayed phase on the interval from $-\frac{\pi}{2}$ to $\frac{3\pi}{2}$ radians to center the phase clusters observed near 0 and π radians. (**D**) Joint distribution of pre-SREP oscillatory phase and corresponding Shapley values across all electrode contacts. The left heatmap shows the joint distribution across SREP polarities, represented as a two-dimensional histogram (240 × 240 tiles) spanning oscillation phases from $-\frac{\pi}{2}$ to $\frac{3\pi}{2}$. Color represents the log-transformed count of SREP instances within each tile. Green shady regions denote the interval of memory encoding-conducive oscillation phase (i.e. oscillation phase associated with a higher predicted probability of successful memory encoding). For illustration, we applied Gaussian kernel (σ = 3 bins) to reduce fragmentation arising from the high-resolution grid. Low-count tiles (≤1 count) were masked. The right heatmap shows the contribution of positive- and negative-polarity SREPs to the observation count at each tile across the same oscillation phase-Shapley value space. Color represents the log-ratio of observation counts between positive- and negative-polarity SREPs within each tile, $\log_{10}$(Positive / Negative). A red tile indicates that positive-polarity SREPs prevail, blue indicates bins where negative-polarity SREPs predominate. Consistent with the left plot, low-count tiles (≤1 count) were masked. (**E**) Shapley value of pre-SREP oscillation phase, stratified by SREP polarity. Curves show the probability density of Shapley values for pooled SREPs as well as for negative and positive polarity SREPs separately. Probability densities are normalized such that their integrals equal one. To reduce the influence of extreme outliers on kernel density estimation, we trimmed Shapley value to the 0.5–99.5 percentiles. The dashed vertical line denotes zero Shapley value.

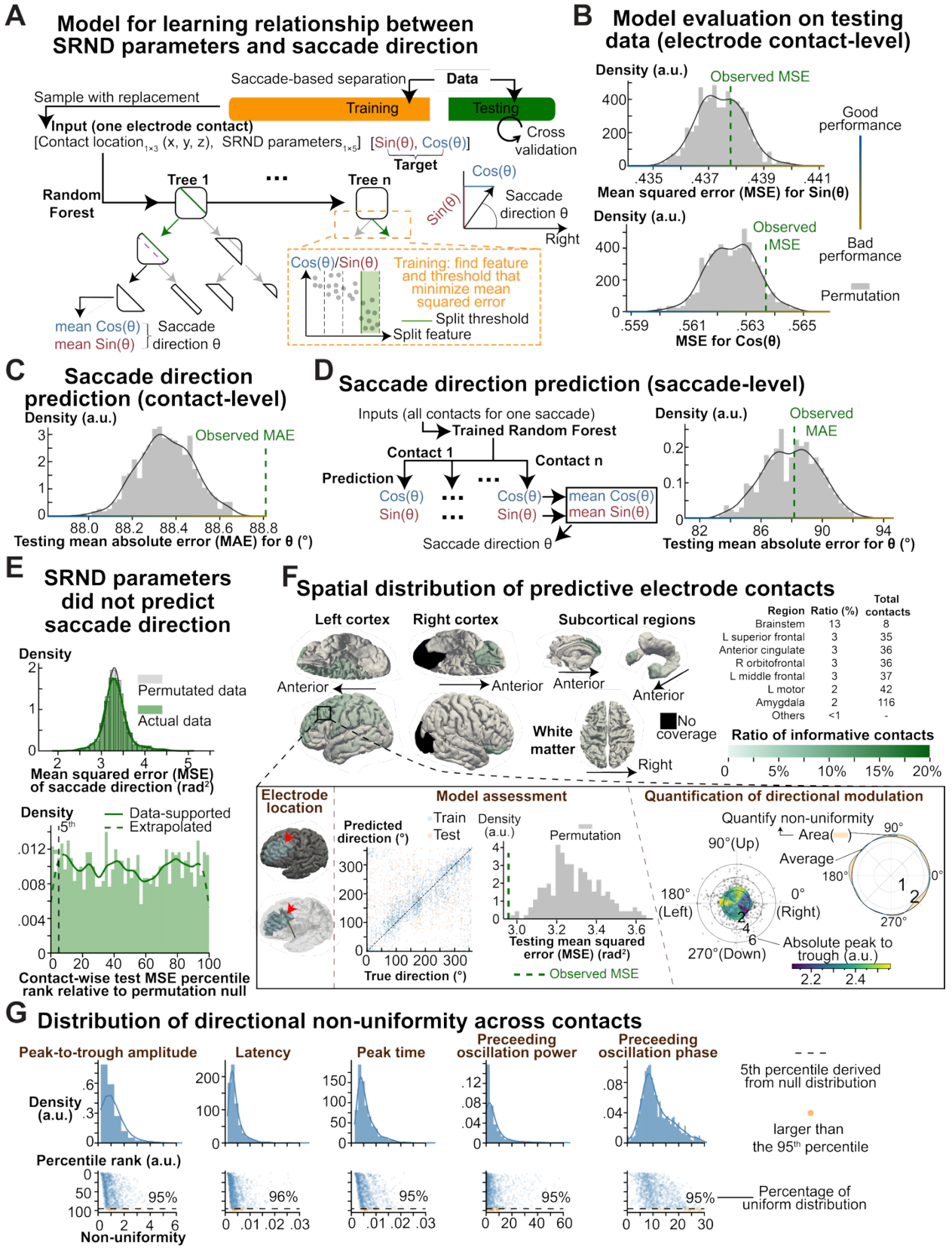

Region	Ratio (%)	Total contacts
Brainstem	13	8
L superior frontal	3	35
Anterior cingulate	3	36
R orbitofrontal	3	36
L middle frontal	3	37
L motor	2	42
Amygdala	2	116
Others	<1	-

Figure 8. **Most saccade-related evoked potentials (SREPs) did not encode saccade directions**. **(A)** Random forest regressor for learning the mapping between saccade-related neural dynamic (SRND) model parameters and saccade direction. We trained a random forest using 5-fold cross-validation. We split the training and testing data at the saccade level. The input to the random forest is a vector that includes the spatial location of electrodes and EP characteristics (e.g., latency, peak-to-trough amplitude, peak time, phase, and power of preceding oscillatory activity). To account for the circular nature of saccade direction, we defined the target as the vector $[Sin(\theta), Cos(\theta)]$, where θ denotes the saccade direction in angular space. This trigonometric transformation allows the use of Euclidean distance as a loss function and enables regression on a continuous 2D representation. During training, the random forest learned a set of features and split thresholds that minimize mean square error within each split node. To encourage spatial generalization while preserving spatial specificity, we added Gaussian-distributed spatial jitter to electrode coordinates, preventing the model from memorizing exact electrode contact locations. After training, each leaf node in a tree outputted $[Sin(\theta), Cos(\theta)]$, averaged across the training samples that reached that node. For SREPs recorded in an electrode contact during a saccade, the predicted saccade direction is the average of the output across all trees. We obtained the predicted saccade direction using the $atan2$, two-argument arctangent function. **(B)** Model evaluation on testing data. To assess whether SRND parameters contain information about saccade direction, we evaluated the model's prediction error on held-out testing data using mean squared error (MSE) between predicted and true [sin(θ), cos(θ)] values. Lower MSE indicates a relationship between SRND parameters and saccade direction, while higher MSE indicates little such a relationship. The vertical green dashed line represents the observed MSE. The gray histogram shows the null distribution of MSE values obtained by training the model on data with permuted target directions. **(C)** Electrode contact-level prediction of saccade direction. We quantified prediction performance at the level of individual electrodes using the mean absolute error (MAE) between predicted and true saccade directions. **(D)** Saccade-level prediction of saccade direction. For each saccade, we averaged the predicted [sin(θ), cos(θ)] vectors across electrodes to obtain the saccade-level prediction of saccade direction. The plot on the right compares the observed MAE against a null distribution generated by permuting saccade directions during training. **(E)** SRND parameters in most electrode contacts did not contain information about saccade direction. The top plot shows the distribution of MSE between predicted and true saccade directions across electrode contacts, compared to a null distribution. For each electrode contact, we computed the observed MSE and generated a null distribution by permuting saccade directions during cross-validation training 200 times. The bottom plot shows the distribution of MSE percentile rank relative to each electrode contact's null distribution. The vertical black dashed line marks the 5th percentile, and the green dashed line represents kernel density estimation outside the data support. **(F)** Ratio of saccade

direction-informative electrode contacts across anatomical regions. We identified electrode contacts where SRND parameters were informative of saccade direction using permutation testing, by comparing the percentile rank of each contact's saccade-level test MSE within its permutation-derived null distribution against a Bonferroni-corrected significance threshold ($\alpha = 0.05$, correcred for the number of electrode contact). The color of each anatomical region represents the proportion of saccade direction-informative electrode contacts among all contacts within that region. The inset illustrates an example informative electrode located in the left middle frontal lobe. In the two 3D brain models on the left, the left middle frontal lobe is highlighted in blue, and red arrows indicate the electrode location. The first middle plot in the inset illustrates the relationship between the predicted and true saccade directions for the training and testing data. The second middle plot shows the observed MSE for the testing data and the null distribution. The rightmost plots show the explanatory analysis of directional modulation for each EP characteristic. For example, we estimated the circular kernel density of the absolute peak-to-trough value as a function of saccade direction. We quantified directional modulation as non-uniformity, operationally measured as the integral of the absolute difference between the kernel density curve and the mean absolute peak-to-trough value across the angular domain. **(G)** Distribution of directional non-uniformity across electrode contacts. The top row shows the distribution of non-uniformity for SRND parameters. The bottom row shows the corresponding percentile rank of non-uniformity relative to each contact's null distribution. Each data point represents an electrode contact. The horizontal dashed line marks the 5th percentile of the null distribution. The annotated percentage indicates the proportion of electrode contacts whose non-uniformity is less than the 95th percentile of their relative null distribution.

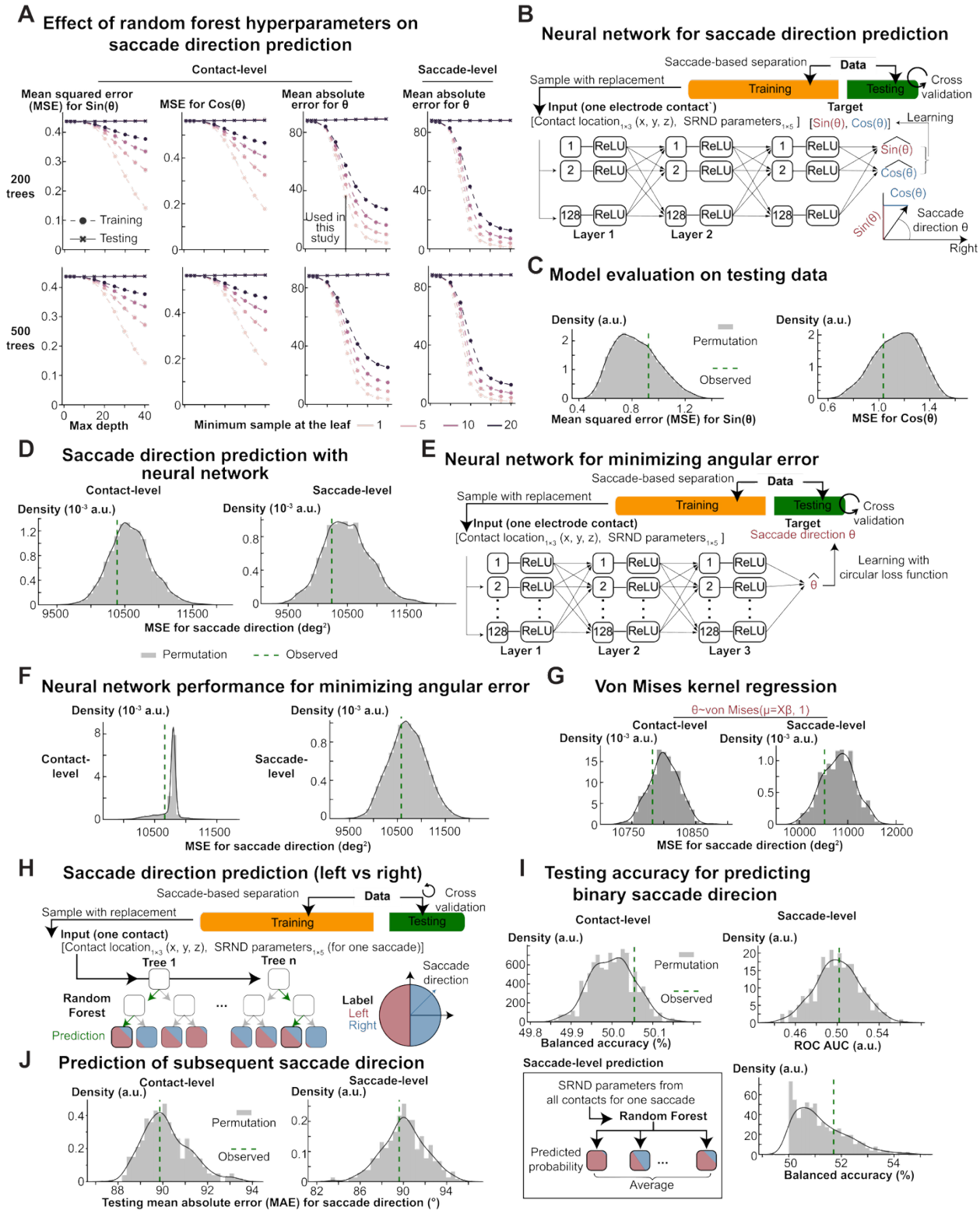

Figure 8 – Figure supplement 1. Most SREPs did not encode saccade directions, nor subsequent saccade directions. (A) Effect of hyperparameters on model performance during training and testing. We evaluated how different hyperparameter

settings affected the performance of random forests for predicting saccade direction. The hyperparameter includes the number of trees, the maximum tree depth, and the minimum sample size at the leaf. In general, deeper trees with a small sample size can learn more complex patterns but risk overfitting. In each plot, color represents the minimum sample at the leaf, and the x-axis represents the maximum depth. From left to right, the y-axis represents electrode contact-level mean squared error (MSE) for $Sin(\theta)$, $Cos(\theta)$, saccade direction θ, and saccade-level MSE for saccade direction θ The top row presents the model performance using 200 decision trees, and the bottom row shows the model performance with 500 decision trees. In this study, we used a default hyperparameter setting of 200 decision trees, a maximum depth of 20, and a minimum leaf size of 1. **(B)** Neural network architecture for predicting saccade direction. To rule out the possibility that the random forest model might not capture the relationship between saccade direction and SRND parameters, we implemented a neural network with three fully connected hidden layers. The input included electrode contact locations and EP characteristics. The output layer had two units representing sine and cosine of the saccade direction $Sin(\theta)$, $Cos(\theta)$. Each unit in the hidden layers was followed by a Rectified Linear Unit (ReLU) activation function to model non-linearity. **(C)** Evaluation of the neural network for predicting saccade direction. The two plots show the observed contact-level mean squared error (MSE) for $Sin(\theta)$ and $Cos(\theta)$, compared to null distributions of MSE obtained from neural networks trained with permuted data. **(D)** Electrode contact- and saccade-level MSE for saccade direction θ. To calculate saccade-level MSE, we averaged the outputs [$Sin(\theta)$, $Cos(\theta)$] across electrode contacts, and computed the predicted saccade direction using $atan2$, the two-argument arctangent function. The vertical green dashed marks the observed MSE for saccade direction, and the grey histogram represents the null distribution of MSE obtained from neural networks trained with permuted data. **(E)** Neural network architecture for minimizing angular loss. As a complementary model to predicting the trigonometric function of the saccade angle (shown in **B**), we implemented a neural network to minimize angular loss. There is one unit at the output layer representing the saccade direction. **(F)** Evaluation of a neural network for minimizing angular loss. The vertical green dashed lines show the observed contact- and saccade-level MSEs between the predicted and actual saccade directions. The grey histogram represents the null distribution of MSEs from neural networks trained on permuted data. **(G)**. Saccade direction prediction using circular kernel (i.e., von Mises kernel) regression. To assess if SRND parameters linearly contribute to saccade direction, we fitted a GLM with a von Mise link function. The plots show the observed contact- and saccade-level MSEs between predicted and actual saccade directions and their null distributions. **(H)** Random forest model for classifying binary saccade direction using SRND parameters. We binarized saccade direction as left vs. right, comparable to the prediction of successful visual encoding (**Figure 6C**). We trained the random forest classifier with inputs of SRND parameters. **(I)** Binary classification of saccade direction

using a random forest classifier. The top-left plot shows the observed electrode contact-level balanced accuracy for testing data and the null distribution of testing balanced accuracy. We generated the null distribution of testing balanced accuracy by training the random forest classifier with permuted binary labels of saccade direction. Similar to visual encoding prediction, we used the averaged predicted probability for rightward saccades across electrode contacts during a saccade as the saccade-level predicted probability. The right plots show the distribution of saccade-level area under the receiver operating characteristic (ROC) curve and the optimal balanced accuracy. We obtained the threshold for optimal balanced accuracy. We generated the null distribution of saccade-level area under the ROC curve and balanced accuracy using the same procedure but with permuted data. **(J)** Prediction of subsequent saccade direction using a random forest regressor. We identified subsequent saccades as the next saccade within 500ms. The random forest regressor structure is shown in **Figure 8A**. The two plots show the observed contact- and saccade-level testing mean absolute error for saccade direction. The grey histogram represents the null distribution of the observed contact- and saccade-level testing mean absolute errors, generated from models trained on permuted data.